COMPRESSION RESPONSE AND ENERGY ABSORPTION OF FILLED CIRCULAR CELL HONEYCOMBS

by

Royan John D'Mello

A dissertation submitted in partial fulfillment
of the requirements for the degree of
Doctor of Philosophy
(Aerospace Engineering)
in The University of Michigan
2014

Doctoral Committee:

Professor Anthony M. Waas, Chair
Assistant Professor Nakhiah C. Goulbourne
Assistant Professor Jason P. McCormick
Assistant Professor Pavana Prabhakar, University of Texas - El Paso
Associate Professor Veera Sundararaghavan
Chian-Fong Yen, Army Research Laboratory

To,

My parents,

Rudolph Casmir D'Mello & *Dorothy Lennie Miranda*

My sisters,

Prima Daisy D'Mello & *Raina Jane D'Mello*

My grandmother,

Severine Lobo

ACKNOWLEDGEMENTS

I am indebted to my advisor Prof. Anthony M. Waas for his excellent mentorship, patience and for being a role model during the course of my doctoral study. I am grateful to Prof. Nakhiah Goulbourne, Prof. Veera Sundararaghavan, Prof. Jason P. McCormick, Prof. Pavana Prabhakar and Dr. Chian-Fong Yen for serving on my dissertation committee and for providing valuable suggestions. I have learnt a lot from colleagues at the Composite Structures Laboratory, especially from technical discussions with Pascal Meyer over coffee breaks, Dianyun Zhang, Dr. Wooseok Ji, Dr. Susanta Ghosh, Dr. Trisha Sain and Dr. Wu Xu. Thanks to Amit Salvi, Dr. Mark R. Pankow and Brian P. Justusson for advice on high rate experiments. I have received generous help from Dianyun Zhang on the smeared crack model and Dr. Trisha Sain on modeling visco-hyperelasticity in polyurethane. Preliminary aspects of this investigation was done in partnership with Lucas R. Hansen and Ms. Sophia Guntupalli. Terry Larrow has built several components for my experimental setups. The honeycombs used in this investigation were purchased from Plascore Inc., Zealand, MI. I am grateful for the financial sponsorship of the Army Research Office and the Army Research Lab, Aberdeen Proving Ground, MD under grant W911NF-09-1-0380. I am forever indebted to my beloved family for their numerous sacrifices and for showing me what unconditional love really means.

TABLE OF CONTENTS

LIST OF FIGURES

Figure

ABSTRACT

COMPRESSION RESPONSE AND ENERGY ABSORPTION OF FILLED CIRCULAR CELL HONEYCOMBS

by

Royan John D'Mello

Chair: Anthony M. Waas

Manufactured circular cell honeycombs are two-dimensional cellular solids commonly used in aerostructures as sandwich panel cores. Honeycombs are also used as energy absorbers, for instance as crash barriers in the automotive industry. There has been some progress in understanding the crush mechanisms of honeycombs in the static regime. However, continuum level models in the failure regime are elusive because of complex localization phenomenon exhibited by these structures. Analysis is instead done using numerical methods such as the finite element method. This study examines the compression response and energy absorption of circular cell polycarbonate honeycombs at high loading rates and when they are filled with soft elastomers. Synergistic behavior is reported in the compression response of honeycombs when they are filled, which simultaneously enhances the peak strength and energy absorption capability. It is also seen that the filler material stabilizes the failure path.

High rate crushing along the axial direction is examined. Since low impedance of such structures preclude the use of the conventional split-Hopkinson pressure bar (SHPB), two new experimental methods are conceived by modifying the SHPB. De-

formation sequence is obtained using high speed imaging. Rate dependence in the crush response is observed. Analysis is done using the finite element method in conjunction with the commercial software ABAQUS/Explicit.

Quasi-static out-of-plane crushing of honeycomb filled with soft elastomer is studied. Here, 3-cell, 7-cell and 19-cell specimens are filled with polyurethane elastomer and then subjected to static compression loading along the axial direction. Diffused folding is the primary failure mechanism compared to localized progressive folding in the unfilled specimen. The in-plane static response of filled honeycomb is also examined with polydimethylsiloxane (PDMS) as filler. Analysis is done using Digital Image Correlation (DIC) and the finite element method. A Smeared Crack Approach is incorporated in the numerical model to account for Mode I cracking in the cell walls. A unique energy dissipation mechanism is reported. High rate axial crushing of filled honeycombs is studied using another modified split-Hopkinson pressure bar. Here, 19-cell specimens filled with polyurethane elastomer are used. The corresponding numerical study is performed using visco-hyperelastic behavior of polyurethane elastomer to capture the rate dependent behavior of the filled honeycomb.

This dissertation provides unique insight into controlling the deformation response of honeycombs so as to maximize the energy absorption under axial crushing.

CHAPTER I

Introduction

Thesis Statement

Honeycomb filled with an elastomer when subjected to compressive loading can have superior load carrying ability, a more stable failure path and better energy absorption capability compared to its unfilled counterpart. This is possible because the interacting filler material can be designed to control the deformation mode of the honeycomb walls.

1.1 Motivation

Manufactured honeycombs belong to a class of structural objects called *cellular solids*. A cellular solid is made up of ordered or random microstructure such that the relative density of the bulk is much lower than unity (Gibson & Ashby (1999)). The repeating unit is called the *cell*. Cellular solids can be classified into two categories, namely *foams* and *honeycombs*. Foams are macroscopically[1] isotropic and are made up of three dimensional repetition of polyhedral cells whose edges contain the material. On the contrary, honeycombs are anisotropic solids and are composed of two dimensional repetition of cells of any fixed geometry that are extruded along the

[1]The word "macroscopic" is used to refer to a volume that contains hundreds of cells.

third dimension. For this reason, honeycombs are categorized as 2D cellular solids. A few examples of naturally occurring cellular solid foams are wood cork and bones (Fratzl & Weinkamer (2007)) and examples of naturally occurring honeycombs are balsa wood and honeybee combs (Zhang et al. (2010)). Figure 1.1 shows few examples of cellular solids found in nature. Cellular solids today can not only be manufactured but are inspired by various designs found in nature. Ashby (1983) says, "When modern man builds large load-bearing structures, he uses dense solids: steel, concrete, glass. When nature does the same, she generally uses cellular materials: wood, bone, coral. There must be good reasons for this." Many of the designs found in nature are promising for practical structural applications, amongst others and are a subject of active research.

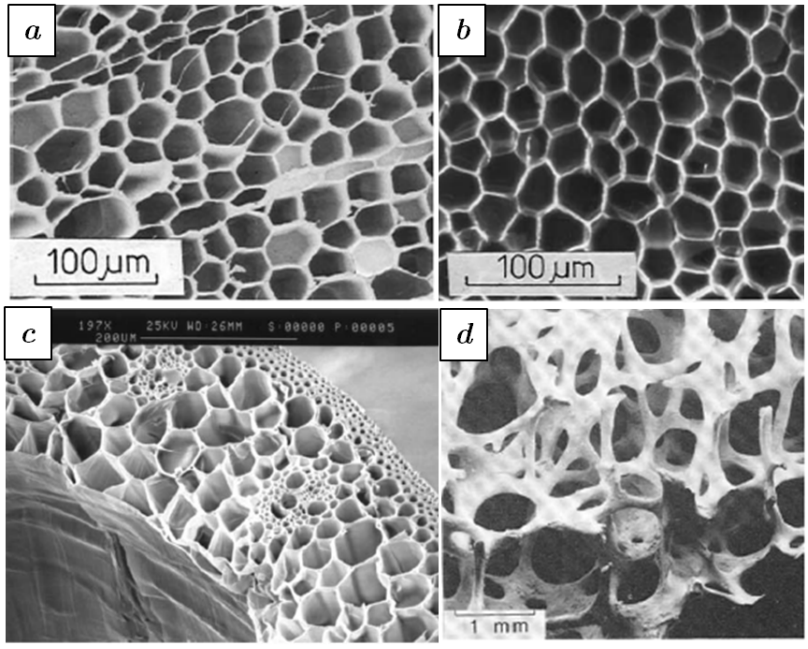

Figure 1.1: Natural cellular solids: Microstructures of (a) balsa wood, (b) cork, (c) grassy stem and (d) trabecular bone (Gibson & Ashby (1999)).

Manufactured foams and honeycombs are usually made out of metals, polymers and paper. Figure 1.2 shows a few examples of man made cellular solids. Foams and honeycombs are used as core material in *sandwich panels*. A sandwich panel is

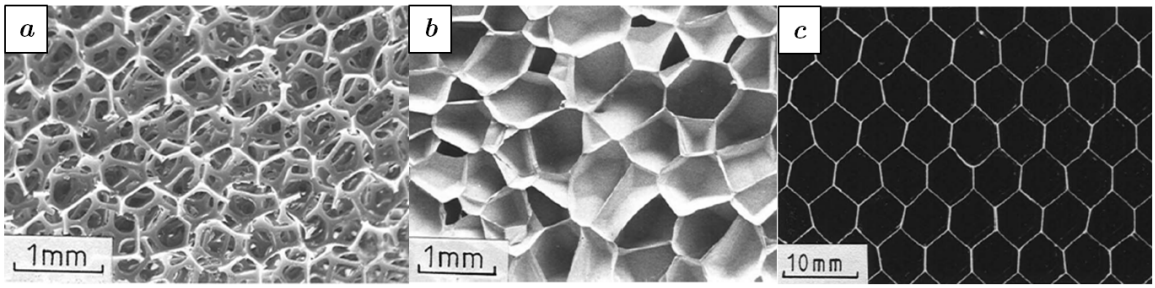

Figure 1.2: Manufactured cellular solids: Microstructures of (a) open-cell polyurethane foam, (b) closed-cell polyethylene foam and (c) hexagonal cell aluminum honeycomb (Gibson & Ashby (1999)).

a structure built up of thin yet stiff skins separated by a light core material such as a honeycomb. The human skull can be thought of as a natural sandwich structure, with a cellular spongy core separated by two layers of dense solid bone. In the case of bending, sandwich panels are analogous to an I-beam, which is commonly used in structural engineering. A typical sandwich structure with hexagonal honeycomb core is shown in Figure 1.3. Here, the sandwich core is analogous to the I-beam's web in resisting transverse shear and the thin face sheet's function corresponds to that of the I-beam's flange in resisting bending and normal stresses.

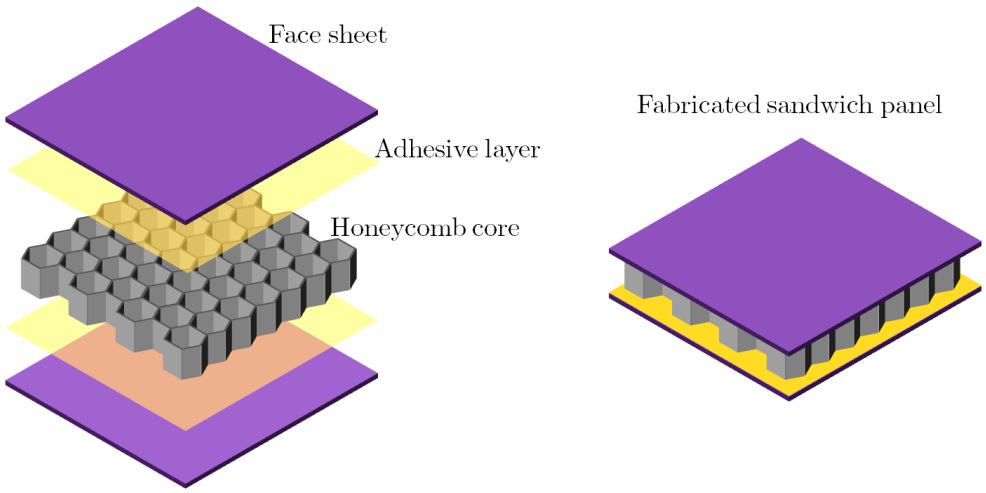

Figure 1.3: Sandwich structure with honeycomb core. Constitutents (left) with fabricated structure (right).

Sandwich structures are important in the aerospace industry due to high demand

on stiffness-to-weight ratio. Here, the honeycomb has three functions. First, the honeycomb resists out-of-plane pressure loads because of high structural stiffness along the honeycomb's out-of-plane direction. Second, it provides high transverse shear resistance. Third, it provides adequate bending stiffness by appropriate choice of out-of-plane honeycomb length in the sandwich panel. In the aerospace industry, these panels are used in helicopter rotor blades and also in aircraft floor panels (Lagace & Vizzini (1988), Petras & Sutcliffe (1999), Zhou et al. (2006)), among others. In the civil engineering industry, they are commonly used in prefabricated housing wall panels and in infrastructure rehabilitation projects such as in bridge decks. Vinson (2001) provides a concise description of the mechanics and applications of sandwich structures in his review paper. Depending on the loading condition, geometry and constituent properties of the core and the facesheets, one of many failure mechanisms may be observed globally or locally as shown in Figure 1.4. Detailed descriptions of failure modes in sandwich structures may be found in the text by Carlsson & Kardomateas (2011).

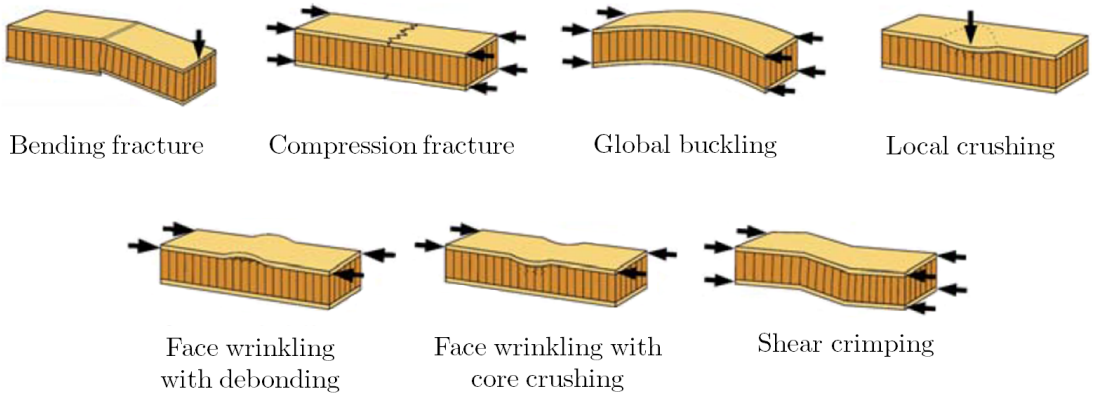

Figure 1.4: Failure modes in sandwich structures under various loading conditions (Heimbs et al. (2006)).

This dissertation focusses on another important aspect of honeycombs - *energy absorption*. Recall that a solid when loaded in the small deformation (elastic) regime

cannot dissipate energy. That is, when external forces are applied, the structure stores the external work done by those forces as internal strain energy. This internal energy is fully recovered upon the removal of these forces. Thus, such an energy conversion process is *reversible*. This aspect of elastic structures along with the solid's stiffness and strength are important parameters in the design of conventional load bearing structures that require long service life. On the contrary, an energy absorbing structure dissipates the work done by external loads using some inherent failure mechanism. Under impact loading, the structure must dissipate some or all of the kinetic energy of the impacting mass. There are several ways in which a material or a structure can dissipate energy under mechanical loads. *Plasticity* in ductile solids such as metals, *viscoelasticity* in dampers when used as shock absorbers in vehicles and *fracture* in brittle solids such as glass when impacted by a bullet, matrix cracking and fiber kinking in composite laminates under compression are a few examples. Here, the energy conversion process is *irreversible*.

The best energy absorbing structure for a given application is the one that absorbs the highest amount of energy, both per unit weight and per unit volume. The use of bulk materials as energy absorbers poses issues from a design point of view. First, bulk materials in general are stiff. Very high loads have to be attained before the structure can initiate internal dissipation mechanisms such as plasticity or fracturing. Second, materials in bulk form are heavy. Cellular solids are much more efficient than bulk solids in absorbing energy because they have more compliant response in their elastic regime and much lower loads are needed to trigger dissipation mechanisms. More importantly, the dissipation mechanism in cellular solids is progressive and this phenomenon takes place at a fairly constant load level (stiffness is zero meaning external work is dissipated and not stored in the structure as strain energy). It is shown later that circular cell honeycomb, the subject of this dissertation dissipates energy by progressive row-wise shear-type of collapse when loaded in the in-plane

direction and by progressive concertina-diamond folding when loaded in the axial direction.

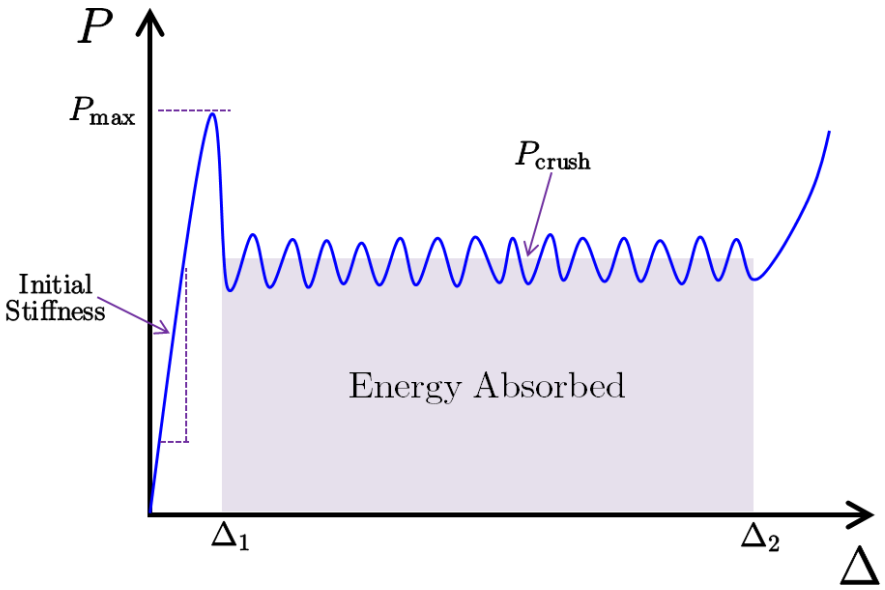

Figure 1.5: General crush response of a cellular solid.

A representative crush response of an energy absorption device such as cellular solids is given in Figure 1.5. Five important parameters for energy absorption design are

1. Initial stiffness.
2. Peak load (P_{max}).
3. Crush load (P_{crush}), also known as plateau load.
4. Stroke, a fraction of the crush distance where energy absorption takes place and is defined as $\Delta_2 - \Delta_1$. Here, Δ_1 is the crush distance where plateau region begins whereas Δ_2 corresponds to the end of the plateau region where densification begins.
5. Energy absorbed ($E_{absorbed}$) whose magnitude is represented as the shaded region.

A particular application would dictate the values of each of these parameters. It is desired that P_{max} should be low and closer to P_{crush}. This is important for energy absorption, especially during vehicle collision because higher peak load means that the vehicle is decelerating rapidly. It is well known that rapid decelerations during vehicle collision increases the risk of serious injury or even leads to death. The fairly constant load P_{crush} determines what level of force is transmitted to the impacted body. The energy absorbed is given by

$$E_{absorbed} = \int_{\Delta_1}^{\Delta_2} P d\Delta \tag{1.1}$$

Consequently, $E_{absorbed} = P_{crush}(\Delta_2 - \Delta_1)$.

Light-weight honeycomb structures for energy absorption applications are commercially manufactured from metals like aluminum and stainless steel or from synthetic polymers such as polycarbonate, polypropylene and aramid. They absorb large amounts of energy when subjected to static or impact loading and are hence used as energy absorption devices in the automotive and aerospace engineering industries as crash barriers and in packaging (Goldsmith & Sackman (1992), McFarland Jr (1964), Gibson & Ashby (1999)). Since energy conversion in such structures is irreversible, these structures serve for one time use. An early and notable use of man-made honeycombs as shock absorbers was by way of aluminum cartridges in the landing module of Apollo 11 (Rogers (1972)). A variety of cell shapes, sizes and cell wall thicknesses are now available for commercial use. The mechanics of such regular shaped honeycombs and also those with random microstructures are given in the text by Ostoja-Starzewski (2008).

Hexagonal honeycombs are most common because of ease in manufacturing compared to circular cell honeycombs. Gibson et al. (1982) and Masters & Evans (1996) provide an analysis of inplane mechanical properties of hexagonal cell honeycombs.

Klintworth & Stronge (1988) have developed elasto-plastic constitutive relations to describe the large inplane deformation of hexagonal honeycombs. Chen (2011) has studied the flexural rigidity and torsional rigidity of hexagonal cell honeycomb by formulating it as an anisotropic plate. Foo et al. (2007) investigated the tensile and compression response of lightweight Nomex paper honeycomb. Lin et al. (2012) show that circular cell honeycombs are more efficient than hexagonal honeycombs with similar relative-density due to higher stiffness and crushing strength along the inplane directions.

To understand the crashworthiness of circular cell honeycombs, previous studies (Papka & Kyriakides (1998), Chung & Waas (1999)) have focussed on the static crushing of circular cell polycarbonate honeycombs via experiments and finite element computations. With increasing understanding of the mechanics, primarily in the static regime, there is interest to provide a continuum level description for such structures, even though localization instabilities may render such a task prohibitive. Equivalent continuum representations of cellular periodic structures must also include higher order effects such as microrotations (Ostoja-Starzewski (2008)). For instance, Chung & Waas (2009) have modeled the circular cell honeycomb as an equivalent elastic micropolar solid in the linear response regime.

The foundational work in the understanding of the mechanics of circular cell honeycomb crushing was laid by the thesis works of S. D. Papka (1998) at the University of Texas at Austin and shortly after by J. Chung (2000) here at the University of Michigan - Ann Arbor. Papka's work focussed on understanding the inplane uniaxial and equibiaxial compression response of circular cell polycarbonate honeycombs, while Chung's work focussed on crushing (uniaxial and general biaxial) under elevated loading rates. The approach in this dissertation is somewhat holistic, in that, both the inplane and the out-of-plane compression responses are considered. The static responses along these two aforementioned loading directions are taken as a starting

point, along with few extensions. The point of departure and main contributions of this dissertation is the study of high rate crushing of honeycomb along the out-of-plane direction, and the mechanics of crushing of "composite" honeycombs that are referred to as filled honeycombs.

1.2 Organization of the Dissertation

This dissertation can be broadly divided into two parts: *Unfilled honeycomb compression* response (Chapters II-III) and *filled honeycomb* response (Chapters IV-VI). In Chapter II, the mechanics of quasi-static compression response of unfilled circular cell honeycomb is presented. Here, both the inplane and out-of-plane loading conditions are considered. In Chapter III, the high rate axial compressive crush response of honeycombs via two experimental methods namely the wave loading device (WLD) and the Direct Impact Method (DIM) are presented. Chapter IV is concerned with the quasi-static compression response of filled honeycomb. Chapter V deals with the quasi-static axial crushing of filled honeycombs. In Chapter VI, the axial dynamic crush response of filled honeycomb is presented. The dissertation concludes in Chapter VII with a summary and recommendations for future work.

CHAPTER II

Static Crush Response of Unfilled Honeycombs

2.1 Introduction

In the previous chapter, cellular solids and the notion of energy absorption in these structures were introduced. It was pointed out that their low relative density and the mechanism of progressive localization when subjected to compression were key to their usefulness as energy absorbing structures. Before discussing the compression response of filled honeycomb structures, it is instructive to first understand the mechanisms of compression response of finite-size unfilled honeycomb structures. Mechanics of the quasi-static compression response along the *inplane* and the *out-of-plane* direction are discussed in this chapter.

The honeycomb material used in this work was manufactured by Plascore, Inc., Zealand, MI. In the circular cell polycarbonate honeycomb, the representative repeating unit cell (RUC) is a circular cell of wall thickness t, radius R and length L along the cell generators. Circular cells are bonded to one another in hexagonal packing along $x - y$ directions to produce a honeycomb panel of desired dimension. A honeycomb panel of size $M \times N$ would indicate that it would be composed of M cells along the x-direction and N cells along the y-direction. A representative sketch of a 11×11 size circular cell honeycomb is shown in Figure 2.1. The direction parallel to the cell generators is called the *out-of-plane* direction. The out-of-plane direction

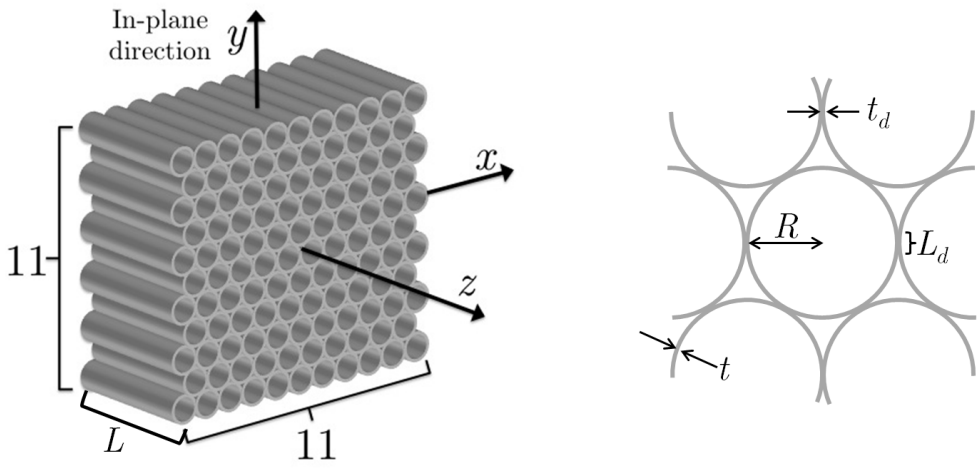

Figure 2.1: Sketch of a 11×11 size circular cell honeycomb (left). Details of the microsection with relevant dimensions, R: cell radius, t: wall thickness, L: cell length, t_d: double-wall thickness, L_d: bond length (right).

can interchangeably be called the *axial* direction. Structurally, the cell is similar to a cylindrical shell because $R/t >> 1$ and $L > R$. Therefore, it is expected that the compression response along the honeycomb's out-of-plane direction would be closely related to that of traditional shell axial compression (Brush & Almroth (1975)). The dimensions of the honeycomb cell are measured using an optical study. The nominal dimensions measured are: cell radius (R) 2 mm, wall thickness (t) 0.080 mm, double-wall thickness (t_d) 0.135 mm, wall-to-wall bond length (L_d) 0.25 mm and out-of-plane length (L) 25.4 mm. Here, the double-wall thickness t_d is the effective thickness of the wall at the contact site of two cells, the contact site having bond length L_d along the cell circumference (Figure 2.1). The density (ρ) of polycarbonate is 1,200 kg/m^3. The volume fraction V_f of this structure with perfect circular cells is

$$V_f = \frac{\pi}{\sqrt{3}} \left(\frac{t}{R} \right) \tag{2.1}$$

The density of the honeycomb ρ_{HC} is calculated as $\rho_{HC} = \rho V_f$. Then, the relative density (ρ_{HC}/ρ) equals 7.3%.

Understanding of honeycomb structural response is more complicated compared to the RUC because of the presence of interaction between an RUC and its neighbors when loaded. The in-plane direction is much more compliant compared to the out-of-plane direction. Moreover, for a given honeycomb specimen, the crush load (also known as plateau or propagation load) during collapse is much higher if the honeycomb is loaded in the out-of-plane direction. The macroscopic prebuckling stiffness (defined for the structure's prebuckling path) in the out-of-plane direction is dominated by membrane action whereas in the in-plane direction, the overall macroscopic stiffness has contributions from bending action as well. Consequently, the macroscopic characterization of a honeycomb structure does not conform to an isotropic model. For a honeycomb with perfectly circular cells, the macroscopic mechanical properties, such as elastic modulus and Poisson's ratio (defined for volumes of material that contain tens of cells) are identical along both inplane directions. This means that the structure is transversely isotropic. These properties are sensitive to deviations of the individual cell geometry from the intended perfect circular geometry (Chung & Waas (2002), Lin & Huang (2013)). Thus, for a honeycomb with elliptical cells, the macroscopic in-plane properties are orthotropic.

The inplane macroscopic stress-strain relation with respect to $x-y$ cartesian coordinates may be written as

$$\begin{pmatrix} \sigma_x \\ \sigma_y \\ \sigma_{xy} \end{pmatrix} = \begin{bmatrix} \frac{E_x^*}{1-\nu_{xy}^*\nu_{yx}^*} & \frac{\nu_{xy}^* E_y^*}{1-\nu_{xy}^*\nu_{yx}^*} & 0 \\ \frac{\nu_{yx}^* E_x^*}{1-\nu_{xy}^*\nu_{yx}^*} & \frac{E_y^*}{1-\nu_{xy}^*\nu_{yx}^*} & 0 \\ 0 & 0 & G_{xy}^* \end{bmatrix} \begin{pmatrix} \epsilon_x \\ \epsilon_y \\ \gamma_{xy} \end{pmatrix} \tag{2.2}$$

If all the cells are perfectly circular, then the inplane properties are isotropic. The macroscopic elastic modulus is

$$E_x^* = E_y^* = \left(\frac{8.329E}{1-\nu^2}\right)\left(\frac{t}{R}\right)^3 \tag{2.3}$$

and shear modulus is

$$G^*_{xy} = \left(\frac{2.306E}{1-\nu^2}\right)\left(\frac{t}{R}\right)^3 \tag{2.4}$$

where E and ν are honeycomb wall material Young's modulus and Poisson's ratio respectively. Then, the inplane Poisson's ratio ν^*_{xy} can be obtained using the well known relation for an isotropic solid as,

$$G^*_{xy} = \frac{E^*_x}{2(1+\nu^*_{xy})} \tag{2.5}$$

which gives $\nu^*_{xy} = 0.806$. Note that this value is independent of the honeycomb material property and depends solely on the geometry of the microstructure.

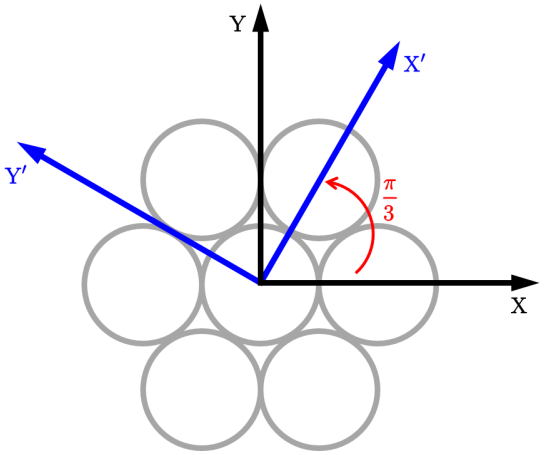

Figure 2.2: Microsection of the circular cell honeycomb showing $\pi/3$ symmetry in cartesian coordinates.

The honeycomb has $\pi/3$ symmetry in the $x-y$ plane on account of hexagonal packing as can be seen in Figure 2.2. Therefore, the macroscopic properties will be identical along some $X-Y$ coordinate frame and another coordinate frame $X'-Y'$ oriented at integer multiples of $\pi/3$ with respect to the $X-Y$ frame. Several analytical and experimental methods to determine anisotropic honeycomb material properties have been reviewed by Schwingshackl et al. (2006).

2.2 Part I: Inplane Crush Response

2.2.1 Stages of Crushing

Consider a finite size circular cell honeycomb that is quasi-statically loaded in the inplane direction as shown in Figure 2.1. Each of the cells deform under a cylindrical bending state. That is, there is no variation in deformation along the out-of-plane direction. Three distinct regions of deformation are seen in the following order: *Linear region* $\longrightarrow$ *Plateau region* $\longrightarrow$ *Densification region*. Figure 2.3 shows the sequence of deformation of an RUC in the linear and plateau regions. A general discussion of these deformation regimes is first presented. Next, important features of crushing are illustrated with examples.

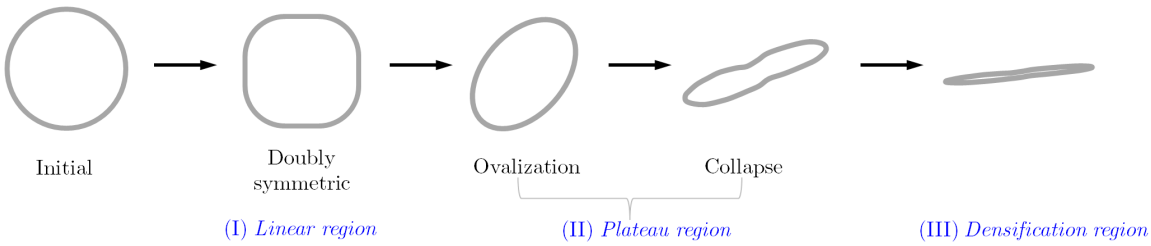

Figure 2.3: Deformation sequence of a typical RUC in a honeycomb specimen subjected to inplane crushing.

I. Linear Region: During the initial stages of loading, the circular cells gradually deform to a doubly-symmetric shape. Here, the doubly symmetric configuration is taken with respect to vertical and horizontal axes passing though the center of a given cell. This deformation mode is uniform across all the cells in the specimen. The load response is fairly linear. This region falls in the structure's prebuckling path. Here, the work done by external load is stored as membrane and bending strain energies in the cell walls.

II. Plateau Region: This region is first characterized by deviation from linearity in the load response. An instability causes the symmetry of deformation in the cells to

break. Cells in one or several rows start to switch into the unsymmetrical deformation mode, where a cell resembles a rotated ellipse. Such a process is called *ovalization*. In a particular row, the direction and magnitude of rotations in the cells are similar. However, to maintain compatible deformation between rows, the rotations must switch in sign between any two rows that are deviating from the doubly-symmetric mode. In such layers, cells form a zig-zag pattern along the vertical direction. In one of these layers, localization occurs where the cells begin to collapse faster than those in the neighboring rows. This local softening caused by instability is reflected globally as a momentary drop in load. The collapse mode in the cell is classified as a *shear collapse*. The location of the first collapse zone is controlled by geometrical imperfections. Simultaneously, the cells in the neighboring rows relax momentarily until complete collapse has occurred. When the cells completely collapse, the structure hardens locally due to contacting cell walls in the collapsed layer. Thus, the load begins to rise momentarily and the cells in the neighboring row begin to collapse. This deformation process occurs until this localization has propagated into the entire structure and this process is accompanied by undulations in the load response. A trough in the undulation signifies the complete collapse of a particular layer and the subsequent crest indicates the unstable cell collapse of the next row. The number of undulations depends on the number of layers in a honeycomb. The mean value of the undulating load is referred to as the *plateau load*. This regime corresponds to the structure's post-buckling path. This is the region of interest in energy absorption applications because the average stiffness in the plateau region is zero and occurs at a lengthy region which is a function of number of rows in the structure. This means that the external work done is dissipated in the row-wise collapse localization.

An explicit expression relating the plateau load to the geometric and material properties of the circular cell honeycomb has not yet been found. This is because of the complex nature of kinematics around the localization zone which are also

highly sensitive to material and geometrical nonlinearities. Thus, analysis of such a structure is done numerically using procedures such as the finite element method. Notwithstanding this, a simple model which considers a single RUC is used to obtain fairly accurate value of the plateau load. This is covered in Section 2.2.5 of this chapter.

III. Densification Region: This region is third in the sequence of deformation events. Here, the collapsed cells exhibit a stiff response and the load rapidly rises with increase in crushing. This region is of little importance in energy absorption as the structure has lost its ability to absorb energy at this point.

2.2.2 Illustration of Crush Regimes

The crush sequence of a 21×21 size honeycomb is shown in Figure 2.4 highlighting key features discussed above. The corresponding load vs. crush distance response is shown in Figure 2.5. Insets (a) through (f) in Figure 2.4 and corresponding points on the plot in Figure 2.5 are described below:

(a) Initial undeformed configuration of the honeycomb.

(b) Circular cells have assumed a doubly-symmetric deformation mode. The honeycomb is in the linear region at this point.

(c) The honeycomb enters the plateau region with limit point instability setting in. The doubly-symmetric mode has switched to a unsymmetrical mode (ovalization) in few layers in the structure. Notice the zig-zag pattern in the cells in these layers.

(d) One layer has completely collapsed. Also, notice that cells have partially relaxed in the rows adjacent to the collapsed row.

(e) Row-wise collapse has propagated into the neighboring rows in the structure.

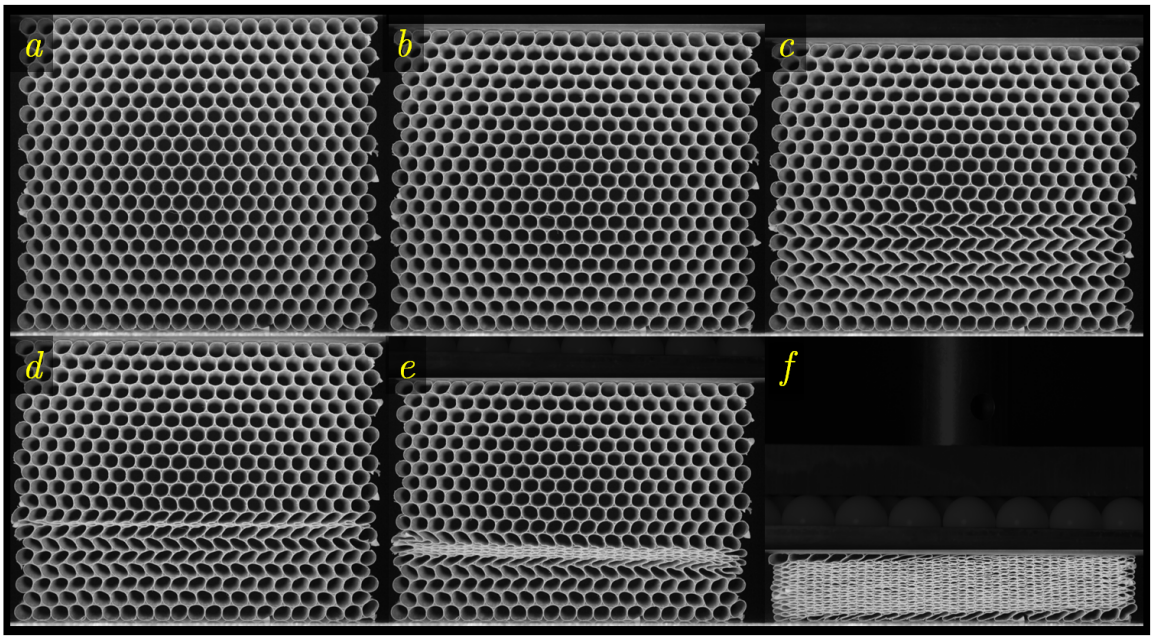

Figure 2.4: Deformation sequence of a 21×21 size honeycomb under inplane quasi-static compression loading.

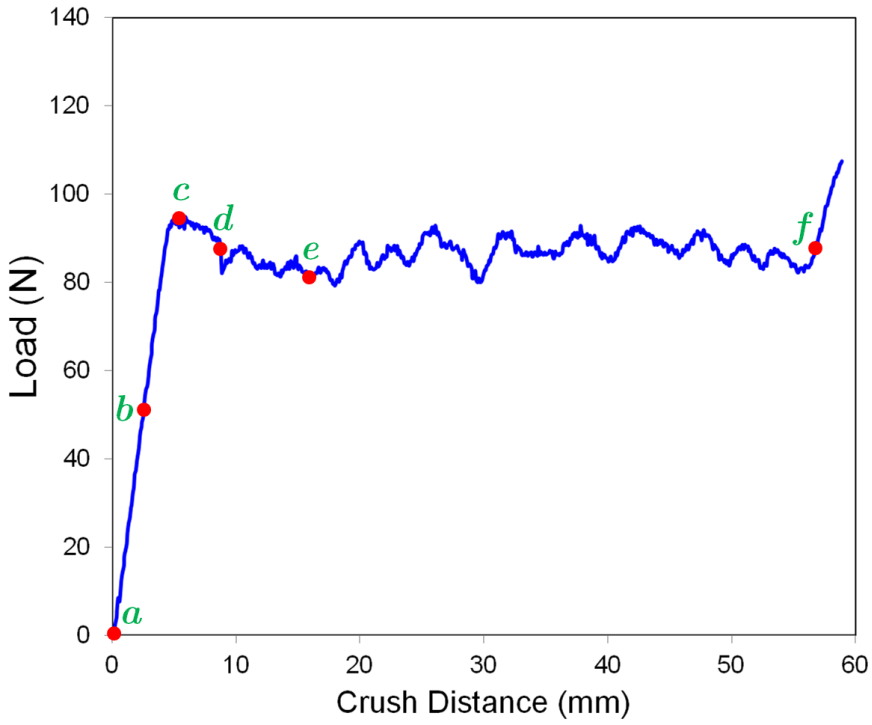

Figure 2.5: Load vs. crush distance for the inplane static crushing of a 21×21 size honeycomb.

This continues untill progressive collapse has propagated into all the rows in the structure.

(f) The structure has entered the densification region as all the cells have begun contacting one another.

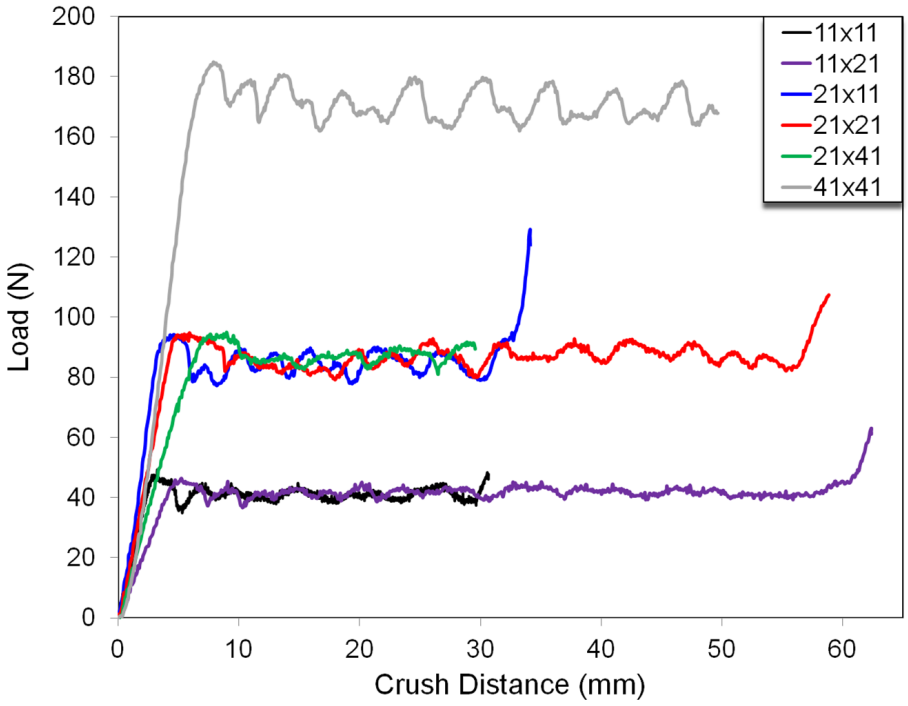

Figure 2.6: Load vs. crush distance for the inplane static crushing of a few finite size honeycombs.

Figure 2.6 shows the load vs. crush distance response for honeycombs of sizes 11×11, 11×21, 21×11, 21×21, 21×41 and 41×41. Observe that the plateau load does not depend on the number of rows along the specimen height. This is not surprising because the collapse mechanism in the plateau regime occurs row-wise and information about the number of rows along the height should not matter. Figure 2.7 shows that the plateau load varies linearly with the specimen width. However, the parameters sensitive to number of rows are stiffness of the linear regime and the densification limit. In the aforementioned sizes, the macroscopic strain to achieve

densification is approximately 0.78. This value would be higher for honeycomb with a higher t/R ratio.

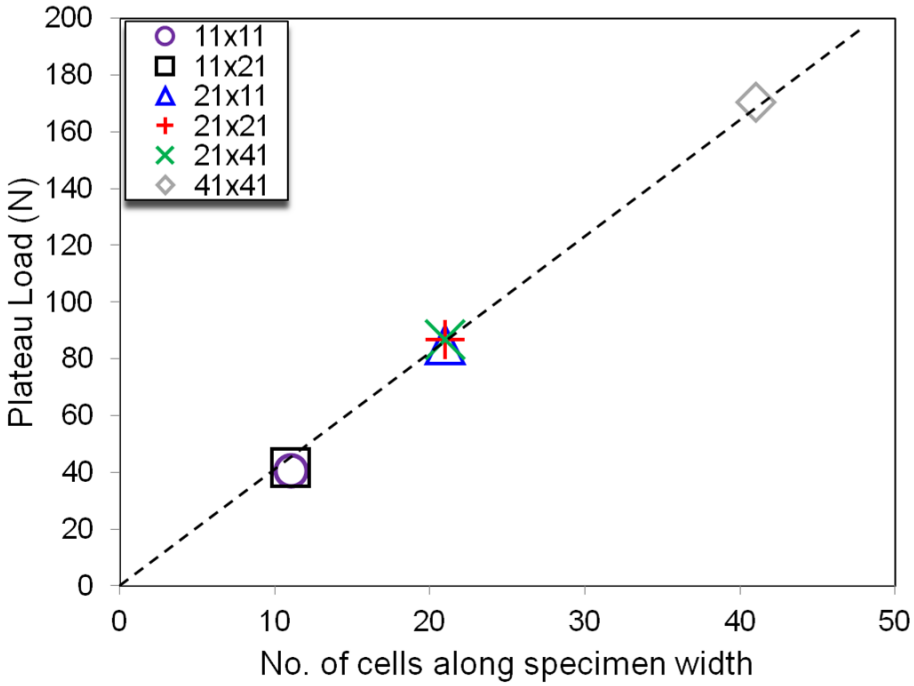

Figure 2.7: Variation of plateau load with number of cells along the width.

2.2.3 Local Measurements in the vicinity of First Collapse

Next, using a 11×11 size sample, the cell deformation in the vicinity of first collapse is studied quantitatively. Manual measurement of points from a series of images is undertaken because the small wall thickness makes it difficult to use an automated measurement procedure such as digital image correlation (DIC). The deformation sequence up to the first collapse row is shown in Figure 2.8. For comparison, the load vs. crush displacement plot is given in Figure 2.9 . Localization occurs in the second row from the bottom. From the images obtained from the test, cells in the layer above the first collapse row are chosen as shown in Figure 2.12. These are marked A, B, C and D. The displacements of these points along the x and y directions are indicated in Figure 2.10 and Figure 2.11 respectively. Rotation of these cells are obtained by

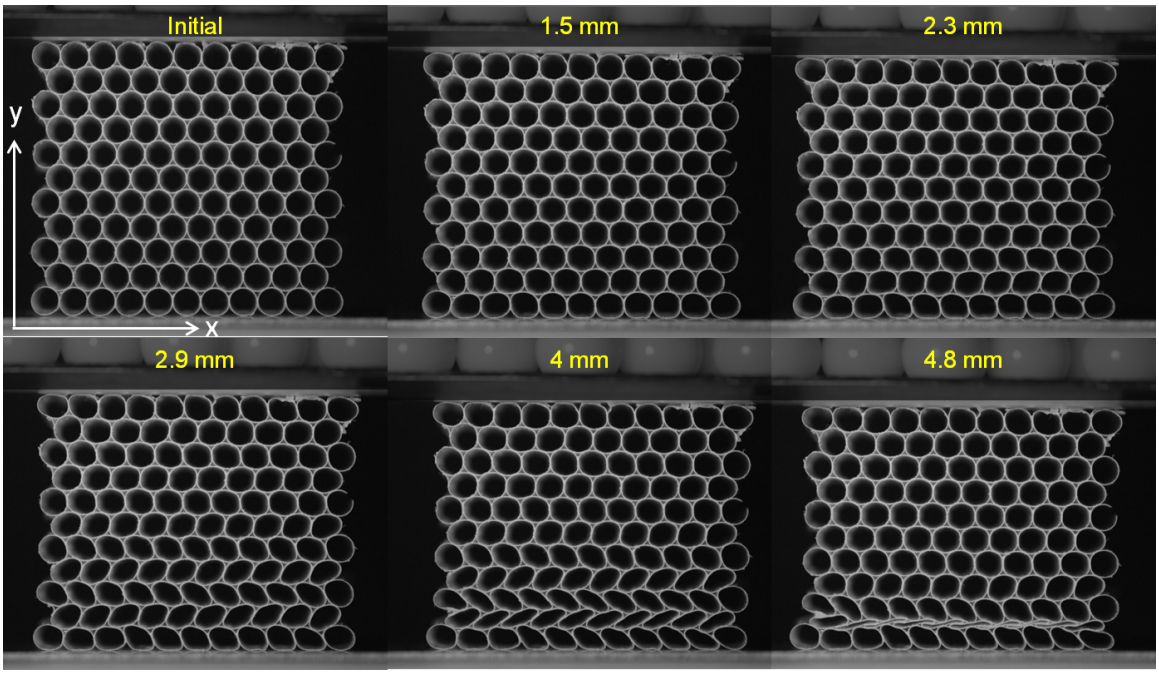

Figure 2.8: Deformation sequence of 11×11 honeycomb under static compression. Second row from the bottom is the first to collapse.

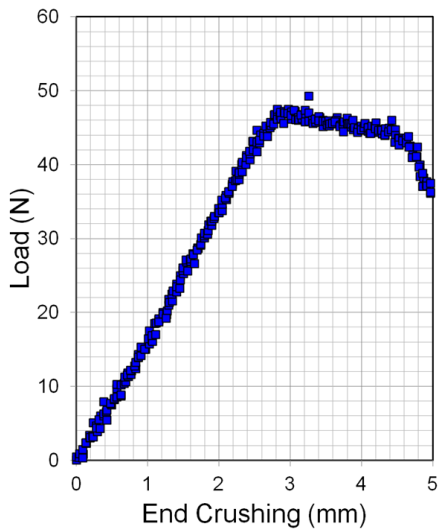

Figure 2.9: Load vs. crush distance response for a 11×11 size specimen under inplane compression, shown up to first collapse event.

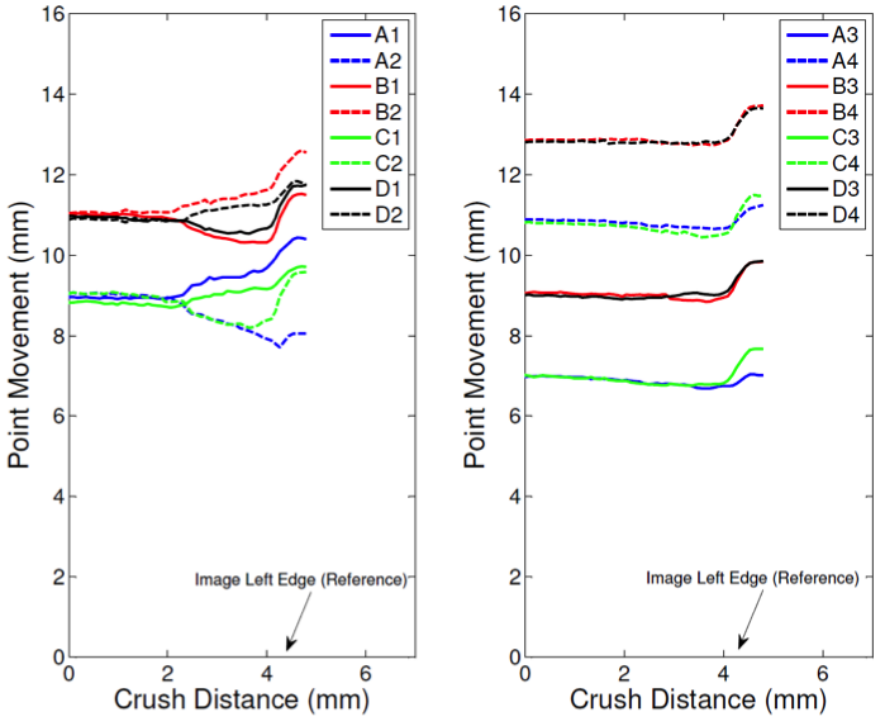

Figure 2.10: Movement of points 1-4 on cells A, B, C and D along the x-direction, as a function of the crush distance.

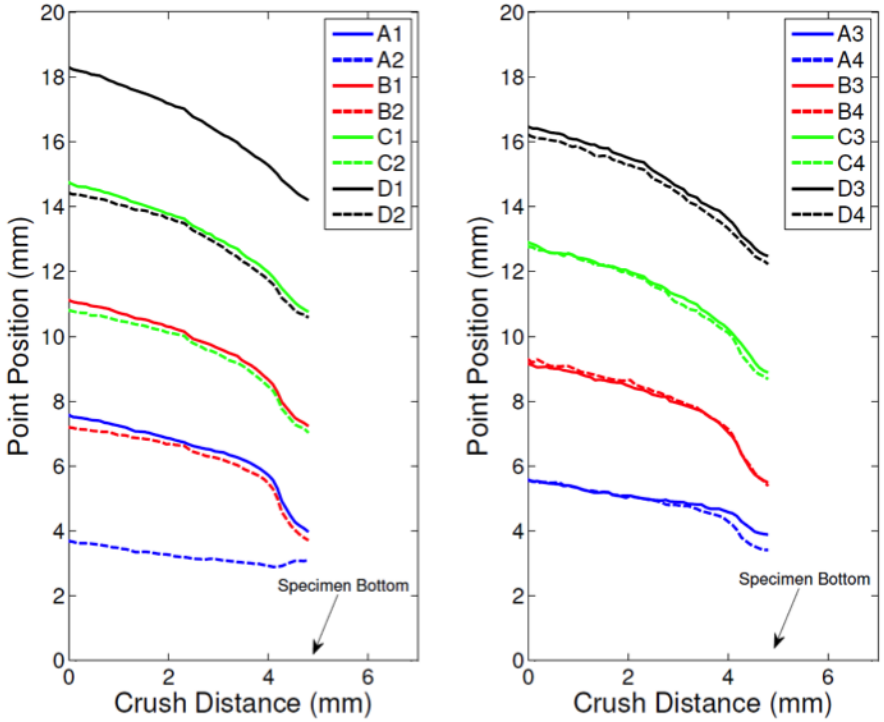

Figure 2.11: Movement of points 1-4 on cells A, B, C and D along the y-direction, as a function of the crush distance.

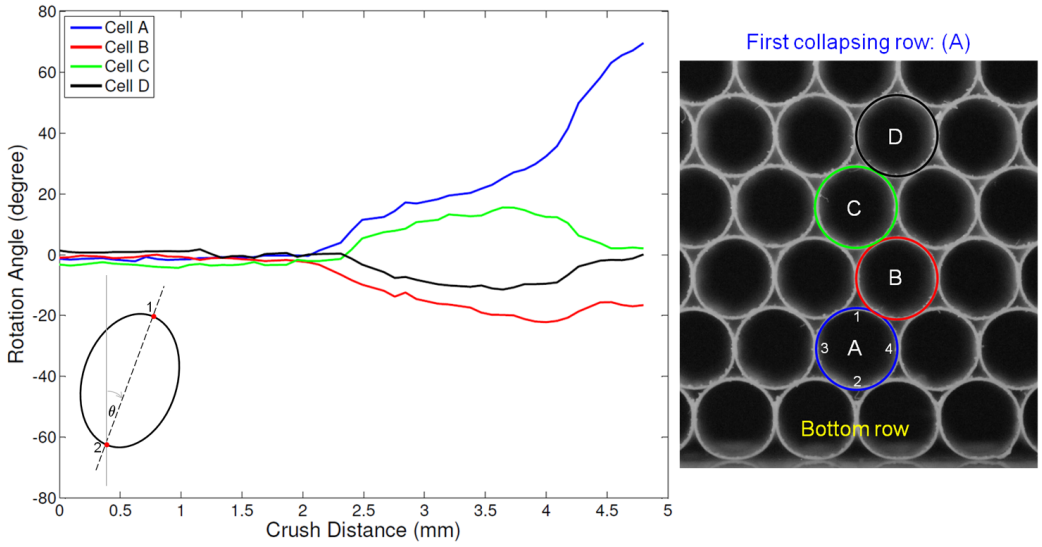

Figure 2.12: Rotation of cells in the vicinity of first collapse row.

carefully measuring dispacements at four points at the top, bottom, left and right most points in the cell. These points on the cell are illustrated in Cell A as 1, 2, 3 and 4. The rotations for the corresponding cells are also shown in Figure 2.12. These are plotted as a function of the crush distance of the moving crosshead that is crushing the specimen from the top. Initially, cells do not rotate up to a crush distance of 2 mm and the structure is in the linear regime. Next, the cells A and B start rotating in opposite directions followed by cells C and D. The magnitude of rotations are equal for pairs A-B and C-D up to crush distance of 3.5 mm to maintain compatible deformation pattern between these two rows. Thereafter, rotations in the cell increase rapidly at crush distance of about 4.2 mm. This signals the unstable collapse in row A. Notice a dip in the load signal in Figure 2.9 around the same crush distance value. Simultaneously, the neighboring rows (B, C, D) relax, which is reflected as a change in the sense of rotation for these cells. Rows that have higher imperfection magnitude start to deviate first. Overall, the plot in Figure 2.12 suggests row with cell A collapses first because it was the first to start deviating from the stable linear path compared to other rows on account of higher imperfection levels.

2.2.4 Single cell Representation

Is it possible to predict the plateau load corresponding to the inplane crushing of the honeycomb?

As seen earlier, the deformation mechanism in the plateau region (the structure's post buckling path) is complex. It would be difficult to arrive at an analytical model to successfully capture such progressive localization behavior. However, from Figure 2.12, it is clear an initial elastic instability causes the initiation of collapse in the first layer. The initial ovalization instability occurs across few layers, of which one layer begins to collapse and the neighboring layers relax. Also, the load at collapse is not greater than the limiting load dictated by the initial ovalization instability. Hence, it is worthwhile to check if the limiting load can be computed by examining the buckling of a single cell. To do this, the internal force distribution at all six loading points in a cell (contact with nearest neighbors) has to be measured. Unfortunately, such information cannot be gleaned from experiment and has to be calculated numerically. Moreover, before the onset of instability, the global response is linear which suggests that the cells are subjected to proportional loading. That is, for a cell with θ measured counterclockwise along the positive x-axis, the loads at the right side ($\theta = 0$) and the left side ($\theta = \pi$) are each in proportion and each of the remaining loads at $\theta = \pi/3,\ 2\pi/3,\ 4\pi/3$ and $5\ \pi/3$ by a scale factor β. The objective here is to see how β depends on specimen size and also how it varies within the honeycomb structure of a particular size.

To measure β, finite element simulations are carried out on honeycombs of sizes 5×5, 7×7, 11×11, 15×15, 25×25 and 31×31. Each honeycomb model is subjected to inplane compression loading. For each specimen size, four cells are chosen and the value of β is measured. One cell is chosen at the specimen's geometric center and three others are randomly selected. Figure 2.13 shows the results from such a procedure. The average value of β is 0.58. There is a scatter in β values for the two

smallest sizes, i.e. for 5×5 and 7×7 size models. The disparity is due to cells on the free boundary. The boundary effect is stronger for smaller sized specimens. Notice that for larger sizes, the value of β chosen at random points in the specimen is close to the mean value 0.58. Interestingly, for the smaller size specimens, the β at the center cell is close to the mean β value. This is shown in Figure 2.14a. Therefore, it is concluded that for this system, the value of $\beta = 0.58$ should hold for larger size specimens as well.

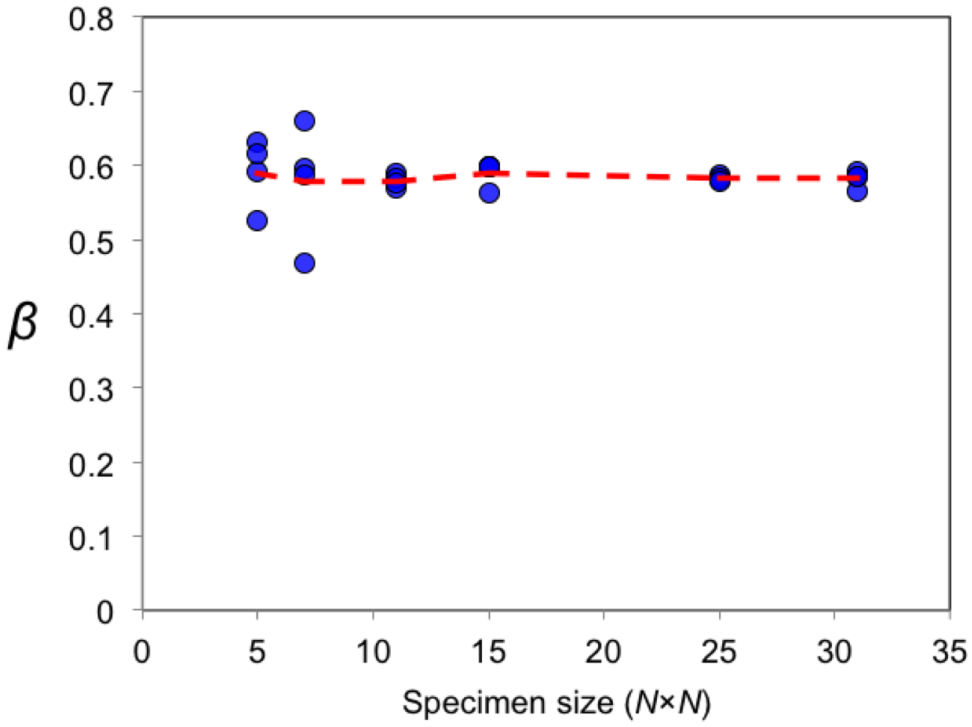

Figure 2.13: Load factor β as a function of specimen size. Dashed line corresponds to the β for each size.

Next, the knowledge of β is used to arrive at a simplified single cell model which would give an estimate of the plateau load. Figure 2.14 shows two idealized models for an isolated cell (Figure 2.14a) in the honeycomb. Figure 2.14b shows the first step in the simplification of the isolated cell. Here, concentrated loads are assumed to be act at the six contact points. Essentially, the loads having contributions along the vertical directions (at $\theta = \pi/3,\ 2\pi/3,\ 4\pi/3$ and $5\ \pi/3$) are unknowns (P) while the

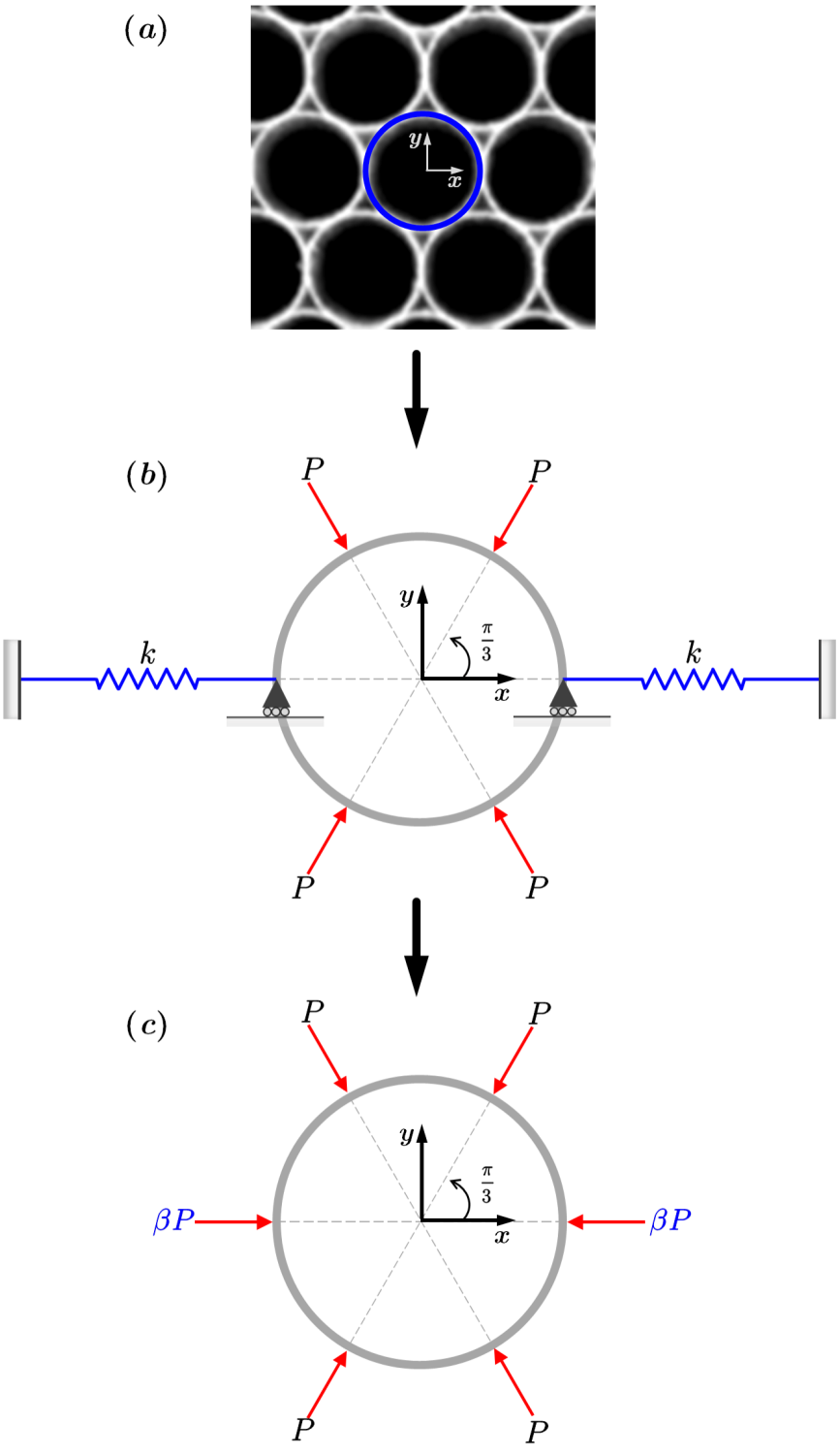

Figure 2.14: Representing an isolated cell with forces acting at six points.

right and the left points (at $\theta = 0$ and π) are represented by springs which have a form $k = \beta_k(EI/R^3)$ where β_k is an unknown spring constant. The ends of the spring are fixed. Such an arrangement with springs would allow rigid body motion along the x-direction during collapse as seen in the experiment. This can be further simplified by replacing the springs with equivalent forces (see Figure 2.14c) that are a fraction of the unknown force P by a factor β which was shown earlier. This model is only valid for a linear buckling analysis. This is because the "prescribed" proportional loading is only valid up to the onset of buckling. The finite element simulations are carried out on a ring geometry (Figure 2.14c), which is meshed using 126 two node beam (B21) elements in ABAQUS with only elastic properties and average dimensions. The critical buckling load P_{cr} for this single cell model equals 2.42. The critical buckling mode of the RUC is shown in Figure 2.15. The prebuckling mode of deformation using the value of $P = Pcr$ is examined by using a static solver. Figure 2.16 shows a comparison of the simulated prebuckling mode with the prebuckling mode from experiment just before ovalization. We can then calculate the total applied load per cell at the instance of buckling is $Q_{1-cell} = 2P_{cr}\sin(\pi/3)$. Then, for a specimen with N cells along the width, the applied load at the onset of instability can be calculated as $Q_{N-cell} = 10\sqrt{3}(N-1)P_{cr}$. For a 11×11 sized specimen, the load for collapse is calculated to be 41.95 N compared to the experimentally obtained plateau load of 41.18 N for specimens 11 cells wide. Therefore, the single cell model, as described here does a good job of predicting the plateau load corresponding to the inplane crushing of a circular cell honeycomb. This could be used for design studies to estimate energy absorption. Furthermore, such an approach for other cell shapes is left for future study.

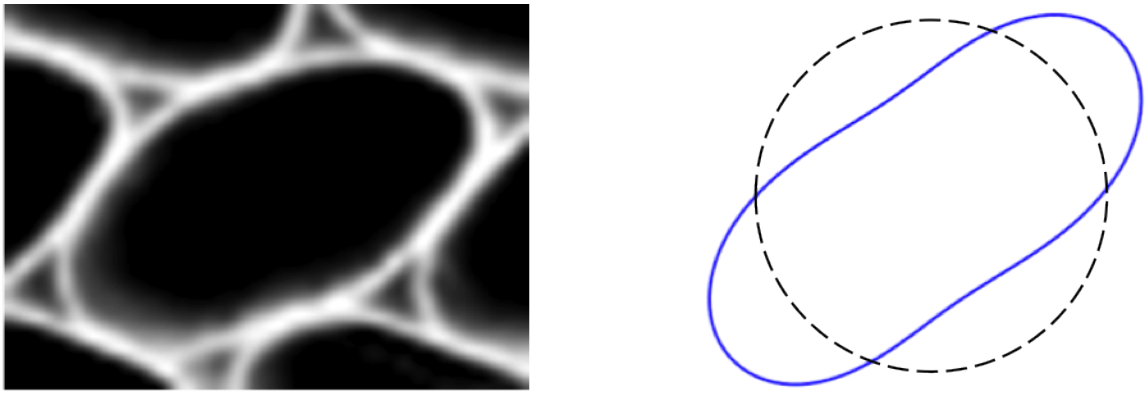

Figure 2.15: Experimentally observed anti-symmetric ovalization mode (left) compared with the simulated mode for a single cell (right).

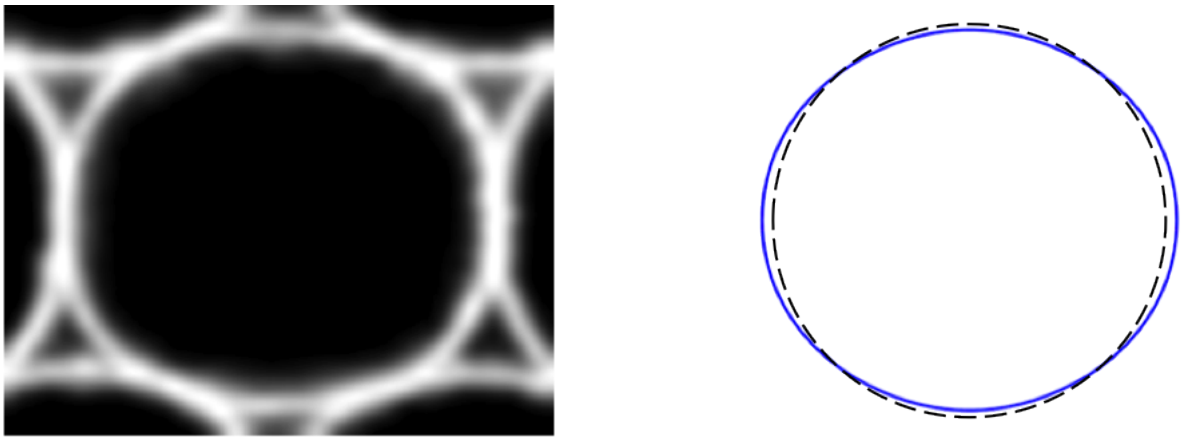

Figure 2.16: Experimentally observed doubly-symmetric prebuckling mode (left) compared with the simulated mode for a single cell (right) for P just less than P_{cr}.

2.3 Part II: Out-of-plane Crush Response

2.3.1 Introduction

As will be seen later, the out-of-plane (or axial) crushing of circular cell honeycomb exhibits a response that is closely related with the classical cylindrical shell buckling problem because the individual cells are essentially thin-shells. Thus, it is useful to first understand the behavior of an isolated cylindrical shell under axial compression. When axially compressed, a circular cylindrical shell initially exhibits a stiff load response in the prebuckling regime. Here, the shell undergoes purely uniform axisymmetric deformations which means that with some length shortening, there is a uniform increase in the diameter. At some critical load P_{cr}, the shell rapidly buckles into either an axisymmetric or non-axisymmetric (doubly periodic) mode as seen in Figure 2.17. The theoretical critical buckling load for a cylindrical shell with radius R, wall thickness t that is made up of material having elastic modulus E and Poisson's ratio ν, is (Brush & Almroth (1975))

$$P_{cr} = \frac{2\pi E t^2}{\sqrt{3(1-\nu^2)}} \tag{2.6}$$

and the theoretical critical end-shortening value is

$$\Delta_{cr} = \frac{P_{cr} L}{2\pi R t E} \tag{2.7}$$

However, in contrast to beams or plates under axial compression, extensive research has shown that cylindrical shells are highly imperfection sensitive (Singer et al. (2002)). This means that for an axially compressed shell, the measured buckling load (P_{exp}) can be much lower than the theoretical critical buckling load P_{cr}. In fact, the measured buckling load can be as low as $0.2P_{cr}$ depending on the R/t ratio and the severity of initial unintended geometrical imperfections and misalignment in load-

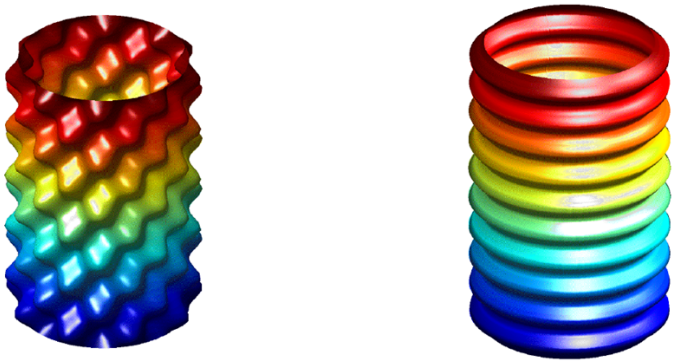

Doubly-periodic mode

Axisymmetric mode

Figure 2.17: Two eigenmodes of a axially loaded cylindrical shell.

ing. Initially, the cause of such a discrepancy was widely debated. A major insight into the role of initial imperfections was made by von Kármán & Tsien (1941). Koiter (1945) was one of the first researchers to rigorously demonstrate the influence of initial imperfections on the shell buckling response using asymptotic analysis. He later analyzed the imperfection sensitivity of a cylindrical shell with axisymmetric imperfections using bifurcation analysis (Koiter (1963)). The factor by which the measured buckling load (P_{exp}) is lower than the theoretical buckling load P_{cr} is called the knockdown factor $\alpha = P_{exp}/P_{cr}$. Figure 2.18 shows representative load vs. end-shortening responses of perfect and imperfect cylindrical shells under axial compression. It has been verified experimentally (see Brush & Almroth (1975)) utilizing several cylindrical shells that α decreases with an increase in the R/t ratio. This means that the imperfection sensitivity increases with increase in the R/t ratio. For $R/t < 1,500$, the knockdown factor α has been approximated in NASA SP 8007 using an empirical relation (Weingarten et al. (1965))

$$\alpha = 1 - 0.901 \left[1 - \exp\left(-\frac{1}{16}\sqrt{\frac{R}{t}} \right) \right] \tag{2.8}$$

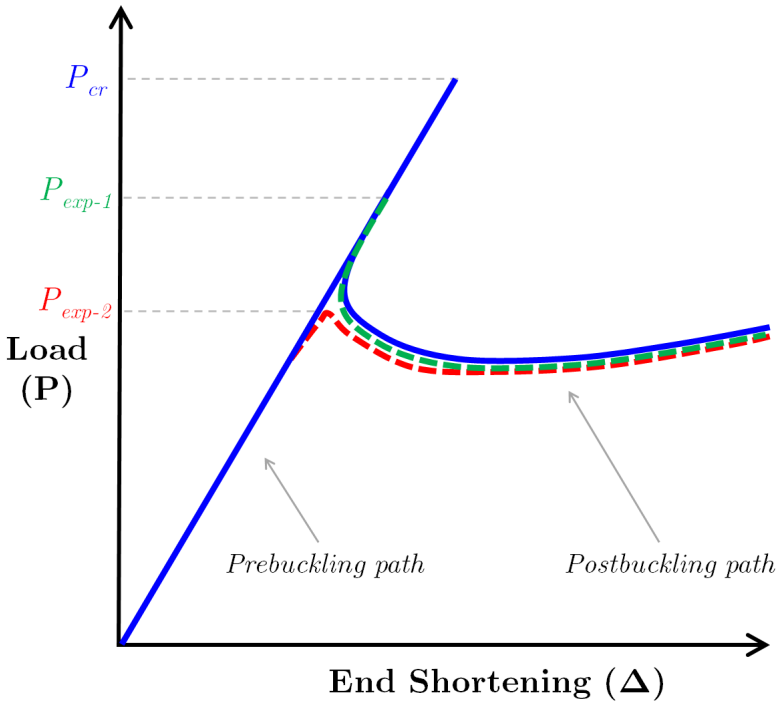

Figure 2.18: Load vs. end-shortening response for perfect (blue) and imperfect thin cylindrical shells (green and red). Critical buckling load is P_{cr} for a perfect shell. The magnitude of imperfection in shell corresponding to the red curve is higher than that corresponding to the green curve.

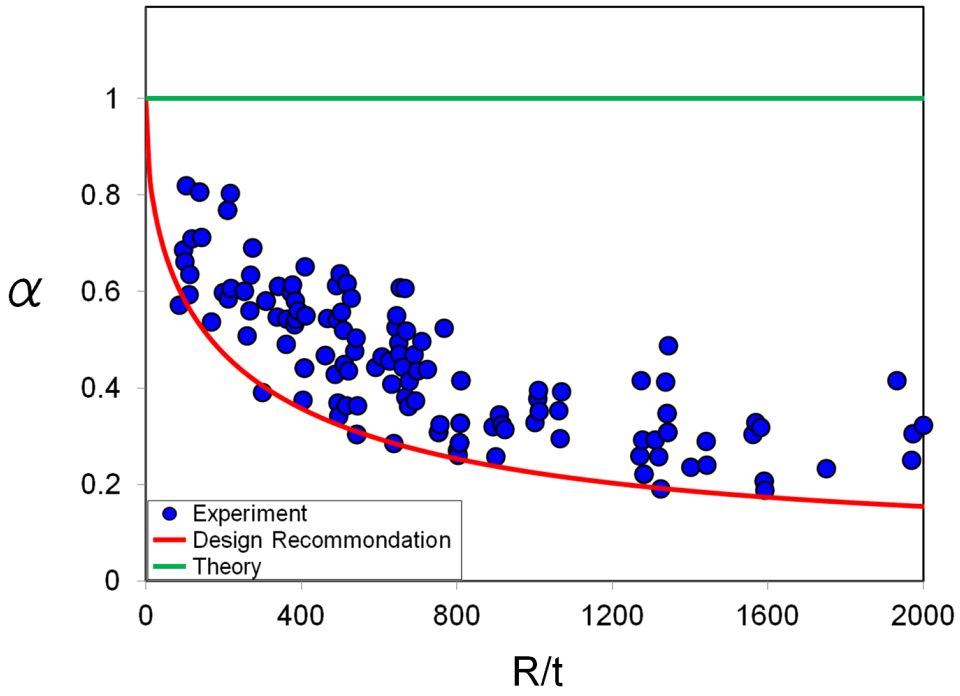

Figure 2.19: Experimental data on the knockdown factor α as a function of R/t ratio for shells under axial compression (Digitized from Seide et al. (1960)).

However, the post-buckling strength is only mildly affected by imperfections.

2.3.2 Past Work

The static out-of-plane crushing (see Mellquist & Waas (2002) and Mellquist & Waas (2004)) of circular cell honeycombs is briefly reviewed here. Mellquist & Waas have extensively studied the static out-of-plane crush response of polycarbonate honeycombs through experiments. They tested specimens composed of cells ranging from 1 to 169. The honeycomb cells were of radius (R) 1.588 mm and having wall thickness (t) of 0.128 mm. The length (L) of the cell was 25.4 mm in the out of plane direction. The Young's modulus of the polycarbonate material was 2,420 N/mm^2 and Poisson's ratio (ν) 0.3. Axial static tests were conducted to understand the response of honeycomb specimens containing different numbers of cells. The specimens were rigidly mounted on the loading frame by bonding with flat pieces of aluminum. The specimens were subjected to compression using displacement controlled loading. The initial part of the macroscopic stress-strain plot was characterized by a region of stiff linear response. A maximum stress, Σ_{peak} was attained (Figure 2.20). Macroscopic strain of 0.02 was reached and there was no noticeable radial deformation until this point. Macroscopic strain of a honeycomb of undeformed length L crushed by Δ is defined as $\epsilon = \Delta/L$. Immediately thereafter, a well defined localized concertina buckling mode was formed around the circumference of the specimen leading to a drop in the load. More folds were formed at a constant load, referred to as the plateau load until the specimen had fully crushed. This type of failure was observed in all the specimens containing different numbers of cells N. A plot showing the values of peak and plateau loads normalized per cell for cell number N is shown in Figure 2.21.

A finite element model of the honeycomb was developed using ABAQUS® to simulate the axial static crush response of polycarbonate honeycombs. Thin shell, eight-noded elements were used to create 1-cell, 3-cell, 4-cell, 5-cell and 9-cell models.

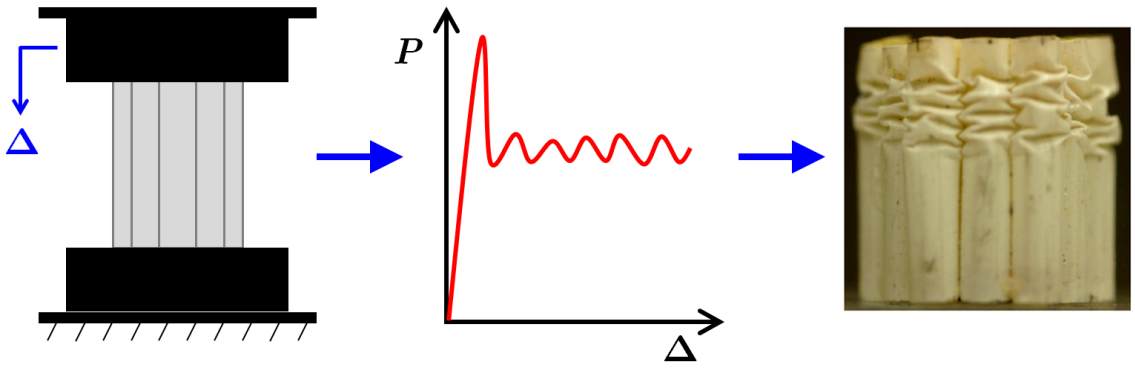

Figure 2.20: Sketch of honeycomb specimen under displacement controlled loading (left). Representative load response showing a prominent peak and plateau region (center). Localized concertina-diamond buckling mode in the deformed specimen (right).

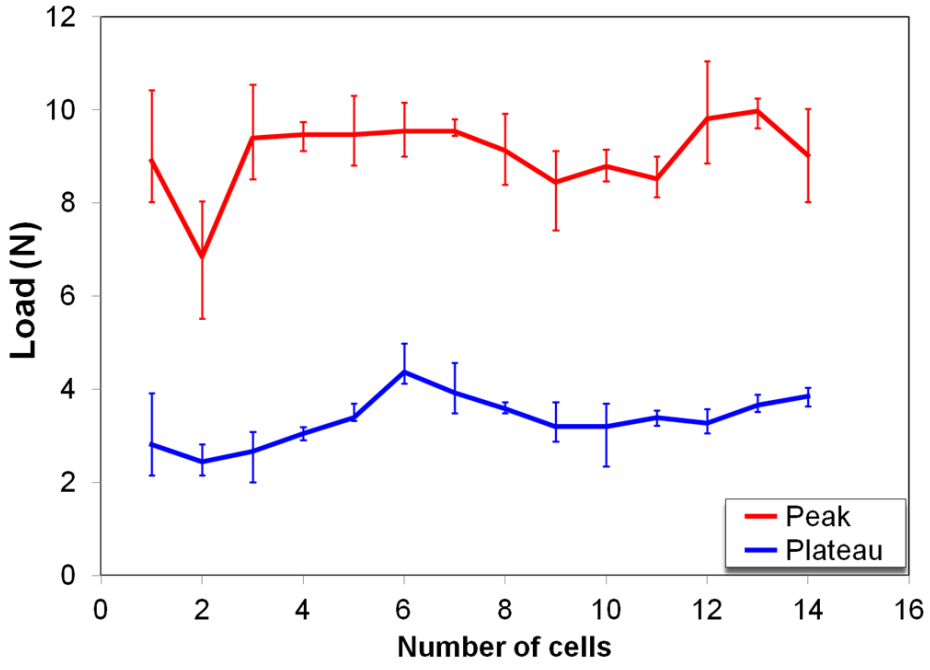

Figure 2.21: Variation of peak and plateau loads as a function of cell number N. (extracted from Mellquist & Waas (2004))

The simulations were carried out using nonlinear geometry and the modified Riks method. The modified Riks method recalculates the model stiffness matrix at every specified time step thus capturing all stable as well as unstable equilibrium solutions. The boundary conditions used in the model were identical to those used in the experiments. Both the end faces were constrained against rotations. The bottom face was constrained against translations. The top face was constrained against translations except along the length of the honeycomb.

Since each cell in the honeycomb cluster is a thin-shell, their crush response will be sensitive to the amount of geometric imperfections. In most cases, even if the maximum imperfection amplitude is known, the information on the exact distribution of imperfections in the structure is not known. However, geometric imperfections can be reasonably represented by seeding the perfect mesh with a linear combination of eigenmodes (Arbocz (1987)). In their study, Mellquist & Waas (2004) used the first three eigenmodes of the structure to seed the perfect geometry. They found that an imperfection magnitude of 0.2% of the shell thickness produced the best agreement with the experimental results. Material nonlinearity of the wall material was introduced in the model by using the J_2 incremental theory of plasticity. The material response was modeled using the uniaxial stress strain response of the polycarbonate material, which is given in Figure 2a in Chung & Waas (2002a). The simulations predicted maximum loads which are in the range of the experimentally measured values but was not able to correctly predict the plateau load seen in the experiments. The concertina-diamond mode of deformation obtained from the simulation closely matched with that observed in their experiment (Figure 2.22).

It is not surprising that the Riks solver could not capture the post-buckling (plateau) regime. The Riks solver is based on finding equilibrium solutions past the point of instability. Around the point of instability, numerous equilibrium paths can co-exist and it is not guaranteed that the Riks solver can find the correct equilib-

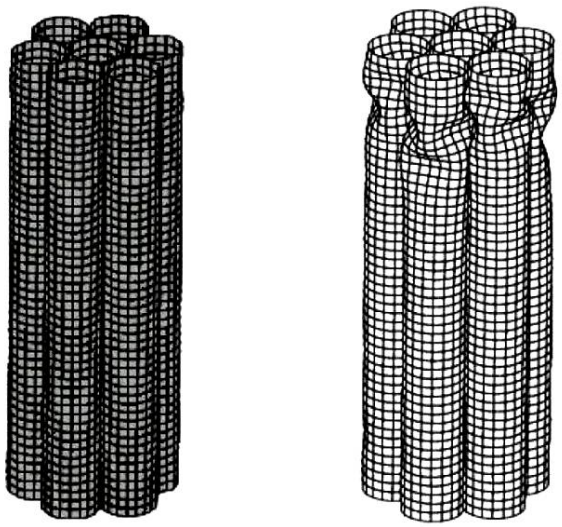

Figure 2.22: An imperfection seeded mesh of a 7 cell specimen (left). The deformed structure obtained from static Riks crush simulation with concertina-diamond mode of deformation (right). (Mellquist & Waas (2004))

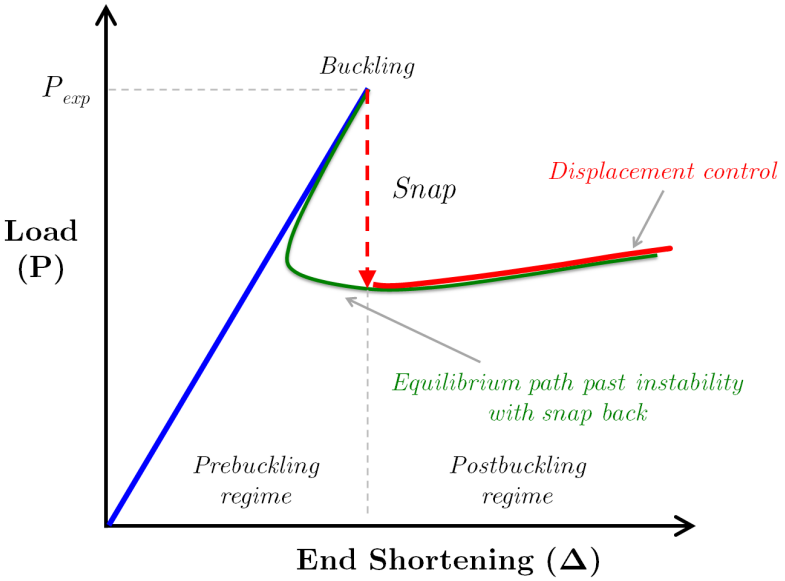

Figure 2.23: Features of shell buckling depicted with a representative load vs. end-shortening response depicting displacement control loading path and equilibrium solution path. Notice the sudden drop in load past the buckling point under displacement control loading. Critical buckling load is P_{exp}.

rium path. In certain cases, if the imperfection magnitude in the model is not high enough, the solver is unable to find any solutions in the vicinity of the instability. This would result in a drawback of unloading the structure because the unloading path is the only available equilibrium configuration. A better choice would have been the use of a Dynamic Explicit solver with displacement control[1]. Being numerically much more efficient, this method is much like the displacement controlled experiment. Recall that during displacement control, the snap-back (seen in equilibrium solutions of imperfection sensitive structures) is replaced by a sharp drop (load-snap) in load which can be easily captured by the Dynamic Explicit solver. Figure 2.23 provides a representative plot with features encountered in thin-shell buckling. The actual equilibrium path (that has the well known "snap back") is shown in green while the scenario under displacement control loading is shown in red.

Mellquist & Waas concluded that scaling in terms of the number of cells per specimen had no influence on the crush load per cell. Also, the average of the peak stress Σ_{peak} and the plateau stress $\Sigma_{plateau}$ per cell, for the various specimens was constant. They also observed that, for a specimen with a given number (N) of cells, the variations in maximum and plateau stress for various experimental trials depended strongly on the axes of symmetry of the loading face of the specimen. The more the number of symmetry axes, lesser the fluctuations in the values of Σ_{peak} and $\Sigma_{plateau}$. Therefore, it was inferred that the specimens having a higher number of symmetry axes were stable and less sensitive to imperfections.

[1]The static axial crushing of honeycombs is numerically simulated using a Dynamic/Explicit solver in Chapter V of this dissertation.

2.4 Conclusions

In this chapter, the circular cell honeycomb was introduced. Next, the compression mechanisms of circular cell honeycombs in the inplane and in the out-of-plane directions was discussed. It was seen that honeycombs crush mechanism in these directions is distinct. However, common features linking each of their response is progressive collapse which are controlled by instabilities. An approximate model to predict the inplane plateau load was presented based on the single cell representation.

CHAPTER III

Dynamic Crush Response of Unfilled Honeycombs: Out-of-Plane direction

3.1 Introduction

[1] In the present chapter, the axial crush response of circular cell polycarbonate honeycombs is the subject of investigation.

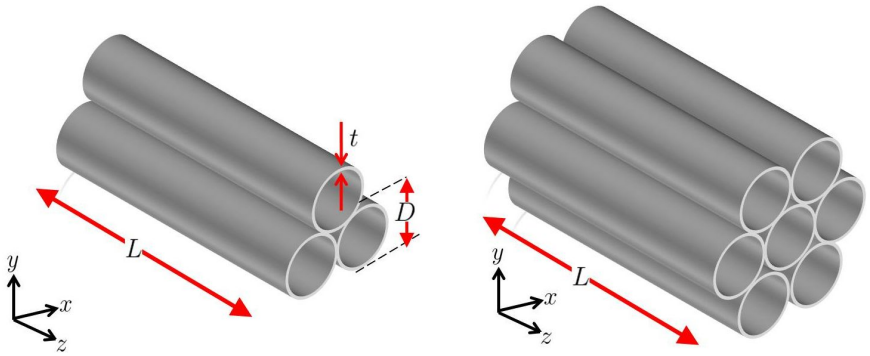

Figure 3.1: Diagram of the 3 and 7-cell circular polycarbonate honeycomb.

A key parameter that characterizes the crashworthiness and which gives a measure of the energy absorption capacity of these structures is the axial *crush load*. The crush load (also referred to as the plateau load in some studies, for example, Papka

[1]Parts of this chapter are published in D'Mello, R. J., Guntupalli, S., Hansen, L. R. & Waas, A. M., "Dynamic axial crush response of circular honeycombs," *Proceedings of the Royal Society A: Mathematical, Physical and Engineering Sciences*, 468, pp. 2981-3005, 2012.

& Kyriakides (1994)) is defined as a state of near constant load where progressive collapse of the structure occurs. The effect of crush load of circular polycarbonate honeycombs with respect to scaling in terms of the number of cells per specimen under quasi-static axial loading was experimentally studied by Mellquist & Waas (2002). They concluded that scaling in terms of number of cells had no significant effect on the axial crush load per cell. Wierzbicki & Abramowicz (1983) studied the axial crushing of metallic tubes and reported that the mean crush force depends on the thickness (t) of the shell as $t^{5/3}$. Wilbert et al. (2011) studied the quasi-static axial crush response of hexagonal cell Al-5052-H39 honeycomb panels experimentally and through explicit finite element simulations. They reported that the fold initiation starts at the center of the specimen and the specimen progressively crushes towards either ends. Wu & Jiang (1997) studied static and dynamic axial crush response of metallic honeycombs and reported that the crush load was proportional to the impact velocity. Baker et al. (1998) studied the static and dynamic response of high density metal honeycombs. They reported that the dynamic plateau stress was about 50% higher than the quasi-static value. Vural & Ravichandran (2003) studied the dynamic compressive response of balsa wood (a naturally occurring cellular material) along the grain direction using a modified split Hopkinson pressure bar. They showed that initial failure stress was highly sensitive to loading rate and that the plateau stress was insensitive to the strain rate. Recently, Hou et al. (2011) used a nylon split Hopkinson pressure bar system with beveled ends of different angles to study the combined shear-compression dynamic response of hexagonal honeycombs. They concluded that for a given angle of loading, there was strength enhancement when compared with the quasi-static loading. Hong et al. (2008) conducted quasi-static and dynamic crush tests of 5052-H38 honeycomb specimens under out-of-plane inclined loads. They reported that as the impact velocity increased, the normal crush strength increased but the shear strength was relatively unaffected. Xue & Hutchinson (2006) proposed a continuum

constitutive model to simulate the dynamic strengthening behavior of square honeycomb cores during multi-axial dynamic loading. Their model takes into account inertial resistance, inertial stabilization of webs and material strain-rate dependence. Mohr & Doyoyo (2006) developed a constitutive model (finite strain, orthotropic and rate-independent) for metallic honeycombs based on the plateau stress.

The foregoing literature review indicates a gap in analytical and computational studies related to the deformation response of honeycombs at high loading rates, validated by experimental data, with respect to assessing energy absorption and collapse. The studies of Hong et al. (2008), and Hou et al. (2011) on aluminum hexagonal cell honeycombs, show an increase in energy absorbing capacity at elevated crush rates, but similar findings with respect to circular cell honeycombs and for direct axial crush at elevated rates are absent. A central goal of this study is to extend the findings reported in Mellquist & Waas (2002) to the elevated strain rate regime and to understand the dynamic crush response of a non-metallic honeycomb material with a view to increasing the specific energy absorption (energy absorbed per unit weight). To this end, note that hexagonal and square cell honeycombs are essentially flat plates arranged vertically as a collection whereas, the circular cell is a vertical thin shell, with curvature, which provides a rich plethora of folding dynamics during the axial collapse stage. While the circular shell has been studied in isolation in many prior studies, (see Brush & Almroth (1975)) the interaction of many connected shells and the significance of tailoring this interaction to exploit energy absorption has not been studied before in the dynamic regime. This is an area that requires further study and understanding because of its practical significance related to use in the design of efficient energy absorbing devices in the automotive and aerospace engineering sectors.

Experimental and associated numerical results of the axial dynamic crush response of 3-cell and 7-cell polycarbonate honeycombs are presented with emphasis on

the crush load, fold initiation, fold progression and mode of collapse. The deformation response of specimens with larger number of cells can be gleaned from the 7-cell specimen results as will be discussed later. To the author's knowledge, this study is the first of its kind concerning the dynamic out-of-plane crush response of circular polycarbonate specimens over a range of crush velocities. The features of axial collapse in circular cell honeycombs are important for development of a macroscopic continuum theory (Xue & Hutchinson (2006)), which can adequately predict collapse stresses in honeycombs of given physical and material properties. Even though localization of deformation may preclude such a task, a continuum model is indispensable in the analysis of sandwich panels which may contain thousands of cells. To this end, the dynamic axial crushing of honeycombs is carried out using two methods, each providing a unique set of loading characteristics and facilitating a range of input crush velocity; (a) the wave loading device (WLD) method , and (b) the direct impact method (DIM). From the details to follow, the loading from the WLD setup is primarily due to stress waves, particularly during initial stages of loading, whereas the loading in the DIM setup is from inertia loads. Next, the dynamic out-of-plane crushing of circular cell polycarbonate honeycombs is described.

3.2 Test Preparation

3.2.1 Honeycomb Dimensions

3-cell and 7-cell circular honeycomb specimens made out of polycarbonate were used in this study (Figure 3.1). An accurate measurement of physical properties of polycarbonate material and geometric properties of the honeycomb cell respectively is crucial to correctly characterize the dynamic crush response of the honeycomb panels and also to create finite element models. First, samples were prepared with 7-cell specimens cast in cylindrical molds using epoxy resin and hardener at room

temperature. The top face of the hardened sample was polished carefully with dry emery papers of increasing grit sizes in a polishing wheel and was finally polished with a diamond paste with particle size of 5 μm. Several samples were prepared and their micro-section of the cell was studied under an optical microscope (Figure 3.2). As can be seen in Figure 3.2, the cells in the honeycomb panel are in contact with each other not at a point, but over a finite length, which is referred to as the cell adhesion length (l). Variations in the cell dimensions were observed across the samples and the mean value appended with the standard deviation is provided. Cell wall thickness (t) was 78 $\pm$ 3 μm, the double wall thickness (t_D) was 166 $\pm$ 4 μm, the cell adhesion length (l) was 245 $\pm$ 23 μm and the cell radius (R) was 2.026 $\pm$ 0. 025 mm. The length (L) of the specimen along the axial direction, measured separately was 25.4 mm.

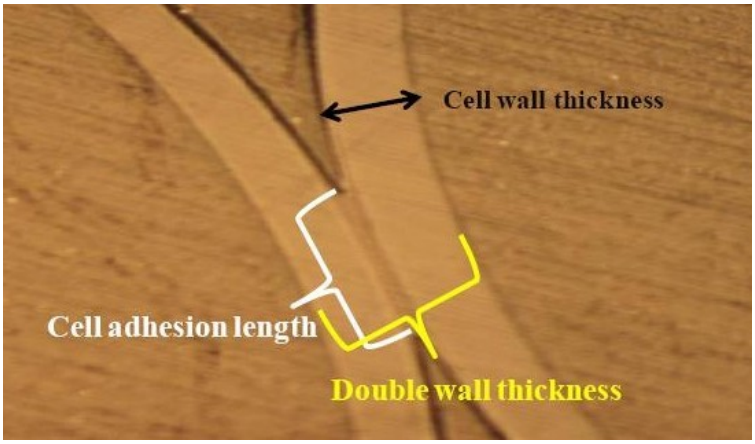

Figure 3.2: Micro-section of the contact site of two cells in the polycarbonate honeycombs as seen under an optical microscope.

3.2.2 Polycarbonate elastic properties & static axial crush load

Next, the elastic modulus of the polycarbonate material was determined using the measured cell dimensions. A single cell was carefully isolated from the honeycomb panel and was mounted to a table-top uniaxial compression test setup. This cell was subjected to displacement controlled compression loading in the in-plane direction to

obtain the stiffness data. Such a test was carried out on 10 samples. The experiments gave a consistent measure of the stiffness measuring 24.1 ± 2.3 N/mm. The factors that amount to the uncertainty in stiffness measurements arise from uncertainty in the cell dimensions (radius, thickness) and also due to the presence of geometric imperfections. A cell subjected to this type of loading is one where the boundary conditions of contact change with the extent of deformation. Therefore, finding an analytical solution form to match the experimentally obtained stiffness is difficult. The problem configuration was simulated using finite elements using the commercially available software ABAQUS/Standard in performing the modulus extraction. The value of the elastic modulus of polycarbonate was assumed to be same in the in-plane as well as in the out of plane direction. Different trial elastic modulus values were used to match the honeycomb cell stiffness from this analysis to the honeycomb cell stiffness that was experimentally measured. The elastic modulus (E) backed out from this analysis was 2,330 ± 222 N/mm^2. Next, axial static crush experiments were conducted on 3-cell and 7-cell specimens. The specimens were crushed at a rate of 0.033 mm/s using an INSTRON machine. The crushing occurred via concertina-diamond folds, the folds propagating from one end of the specimen to the other. The plateau load obtained for the 3-cell specimen was 44 ± 4 N whereas for the 7-cell, the value was 120 ± 7 N. The crush loads obtained will be used to compare with the dynamic crush experiments, in order to determine whether loading rate influences the crush response.

3.2.3 Measurement of experimental data

The dynamic force sensor used in this experiment is a PCB Piezotronics model 208C02. The force sensor was calibrated by the manufacturer. In the experiments that are described in the following sections, the data from the force sensor are acquired at the rate of 1.6×10^6 samples per second. The raw data are first filtered to remove the

high frequency noise such that only the frequencies above the upper limit of the design frequency (90 KHz) of the sensor are eliminated. These data are called *raw data* in the load response plots to follow. The raw data is additionally smoothened using a basic 3^{rd} order Savitzky-Golay averaging filter in MATLAB. These data, which is referred to as *filtered data*, will be plotted alongside the raw data. The raw data will be used to compute estimates of crush/plateau loads and plateau stresses. The discharge time constant of the force sensor is greater than 120 seconds, a duration which is orders of magnitude higher than the time scale of the crush event. The displacement information and mode of collapse is obtained using a high speed camera. Images are collected at the rate of 50,000 frames per second. The images acquired have spatial resolution of 0.33 mm and 0.2 μs temporal resolution which is adequate in obtaining the displacement information through pixel measurements.

3.3 Experiments: Wave loading device (WLD) method

3.3.1 Setup & Procedure

A *wave loading device* (WLD) is utilized to study the dynamic crush response of 3-cell and 7-cell honeycomb specimens. The experimental setup of the WLD is shown in Figure 3.3. The transmitter bar far end is held against a thick rigid immovable steel plate to prevent its movement when the honeycomb specimen is being loaded. The specimen is carefully mounted between the incident bar and the force sensor that was instrumented on the transmitter bar. The end faces of the specimen are positioned at the geometrical center of the incident bar face and the end-cap face to avoid misalignment during impact. The striker bar is fired from the gas gun at a known pressure ($200 - 1{,}000$ psi range) and it impacts the incident bar head on. A compressive stress pulse travels from the impacted end along the length (L_s) of the incident bar with a longitudinal stress wave velocity c_s. When the stress pulse reaches

the specimen end of the incident bar, the pulse reflects back as a tensile pulse in the incident bar and a small part of it travels as a compressive pulse in the specimen. The specimen is thus loaded in compression. The time taken to crush the entire specimen ($L = 24.5$ mm) is much longer compared to the crush duration due to the stress wave. Limited crush length (≈ 1.3 mm) is attained in the first period of crushing due to stress waves.

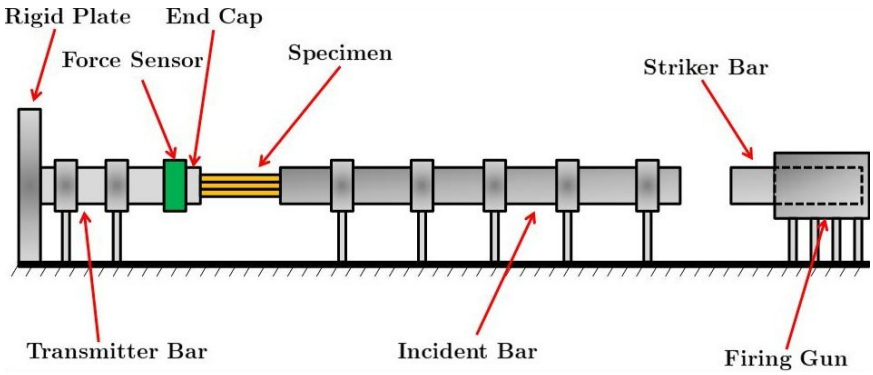

Figure 3.3: Schematic showing the experimental setup of the wave loading device (WLD) . The honeycomb specimen is positioned between the incident bar and the end cap of the force sensor.

The time taken for the next cycle of crushing is equal to the roundabout trip of the stress wave, i.e. time taken to cover a distance equal to $2L_s$. The motion of the incident bar is found to be a ramp-rest sequence (Figure 3.4). The plot in Figure 3.4 is obtained by tracking the position of the incident bar end in contact with the honeycomb, by performing pixel measurements of the high speed images obtained. The cross-sectional diameter of the hardened steel bars is 12.7 mm. This dimension is much smaller compared to the length ($L_s = 1{,}828.8$ mm) of the incident bar. The diameter of the hardened steel striker bar is 12.7 mm and has a length of 304.8 mm. One dimensional wave theory states that the fundamental longitudinal wave velocity (c_s) in a material depends on the elastic modulus (E_s) and density (ρ_s) and is given

by the relation (see Kolsky 2003)

$$c_s = \sqrt{\frac{E_s}{\rho_s}} \tag{3.1}$$

where the elastic modulus (E_S) of the bar material is 210 GPa and the mass density (ρ_s) is 7,800 kg/m^3. From Equation 3.1, the stress wave velocity is calculated to be 5,225 m/s. Utilizing Equation 3.1, the time interval (ΔT_{1-D}) between successive tensile stress waves to reflect from the specimen end of the incident bar is 0.70 milliseconds. This time interval agrees very well with the time interval ($\Delta T_{EXP} \approx$ 0.68 milliseconds) between two successive loading events measured from the experiment (Figure 3.4). Note that this time interval is independent of the gas gun firing pressure or the striker bar velocity. This time interval depends on the stress wave velocity and the length of the incident bar. However, the velocity of impact of the striker bar has a direct relation with the velocity of crushing during the ramping motion of the incident bar. The ramp-rest motion ceases to exist as time progresses because the stress waves in the incident bar gradually wanes out due to damping losses and due to wave interference resulting from multiple reflections in the incident bar. Thereafter, the motion of the bar is mainly due to rigid body motion with lower crush velocities as is seen clearly in Figure 3.4. Therefore, the 1-D wave theory is sufficient to satisfactorily explain the mechanics of ramp-rest motion encountered in this study. Note that one is not concerned with the wave interactions in the incident bar beyond the first reflection at the specimen end. In other words, the incident bar mainly serves as a projectile with ramp-rest loading profile. Also, from the high speed images, it is observed that the transmitter bar does not move when the specimen was being loaded. This observation can be explained due to two reasons: (1) the rigid, immovable plate acts as a momentum trap thus absorbing any stress waves that get transmitted through the specimen, and (2) the high mechanical impedance[2]

[2]Mechanical impedance at any point in a structure is the ratio of the applied force at the point

mismatch at the specimen-transmitter bar interface curtails the ability of the stress waves to pass from the specimen into the transmitter bar. Moreover, note that the intensity of the initial stress pulse that was transmitted through the specimen, till this point, is significantly reduced due to high impedance mismatch at the incident bar-specimen interface. Hence, unlike in a regular SHPB setup, the transmitter bar plays no active role in the WLD experiment, except for restraining the honeycomb in the out-of-plane direction. In summary, the success of the WLD method is in making use of a momentum trap (via the thick, immovable plate) and due to use of SHPB material (hardened steel) that has high impedance mismatch with the test specimen (polycarbonate) such that, in effect, the load that the specimen experiences is that arising from the stress waves in the incident bar.

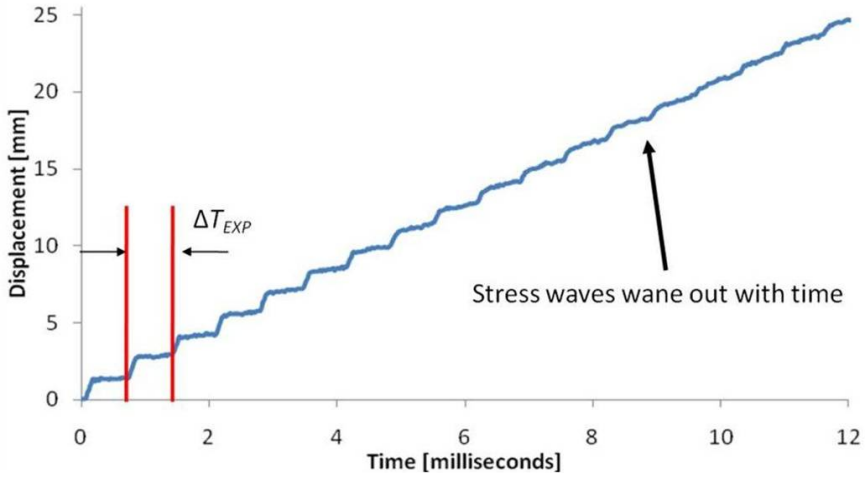

Figure 3.4: Typical rest-ramp displacement of the incident bar at the specimen end. The time interval ΔT_{EXP} for two successive ramp motion is shown. As the stress waves get weaker as time progresses, the velocity of the specimen end of the incident bar tends to that of the rigid body motion of the incident bar.

to the particle velocity at the same point. Qualitatively, it is a measure of how much a structure resists motion when subjected to force.

3.3.2 Results

When the 3-cell and 7-cell specimens were subjected to crush velocities ($v_c \approx 11,000-12,000$ mm/s range) in the WLD setup, a characteristic deformation response is observed. The load-time plot for the 3-cell specimen is shown in Figure 3.5 and the images of corresponding deformation sequence is shown in Figure 3.6. For the 7-cell specimen, the load-time plot is shown in Figure 3.7 and the corresponding images during the initial stages of deformation is shown in Figure 3.8. A steep near-linear rise is seen initially and the load rose to a maximum value, referred to as the peak load. Up to this point, the deformation in the specimen was purely axial and the stiff resistance to the moving bar gave rise to the initial peak load. Thereafter, the first localized axisymmetric concertina-diamond folding began accompanied by a drop in the load. The preference of fold initiation immediately after the peak load is attained depends on the inherent geometrical imperfections present. Fold initiation is typically observed at both ends of the specimen. The folds continues to form as long as the incident bar is in motion. Also, transient elastic folds are observed near the ends of the specimens, which recovers back to the undeformed state in the rest period. After the end of the initial ramp step, the bar momentarily rests. Here, the load recorded fluctuates about a mean value with smaller amplitude due to the residual stress waves in the specimen. No new folds are formed during the rest period. However, the specimen exhibits hoop-like or breathing vibration modes (which are clearly visible in high-speed movies of the experiment). During the second ramp step, the load momentarily rises with fold formation and drops at the end of the ramp step. This process continues until the specimen is completely crushed as new folds are formed progressively along the length of the honeycomb cell. The load recorded, beyond the initial phase where fold formation takes place, is referred to as the *crush load*. The crushing process occurs either (a) from one end with folds formed up to the other end, or (b) simultaneously at both ends. The deformation characteristics explained

above hold for both the 3-cell and 7-cell specimens. For the 3-cell specimens, the peak load recorded is approximately 150 N and the crush load measured was 54 $\pm$ 14 N compared to the static crush load of 44 $\pm$ 4 N. For the 7-cell specimens, the peak load recorded is 335 N and the crush load measured is 159 $\pm$ 22 N compared to the static crush load of 120 $\pm$ 7 N. Here, the mean crush load estimate is calculated as the integral average for the loads recorded over successive ramp sections except for the first ramp movement (corresponding to the initial linear response). The uncertainty indicates standard deviation in this load level across various experimental trials.

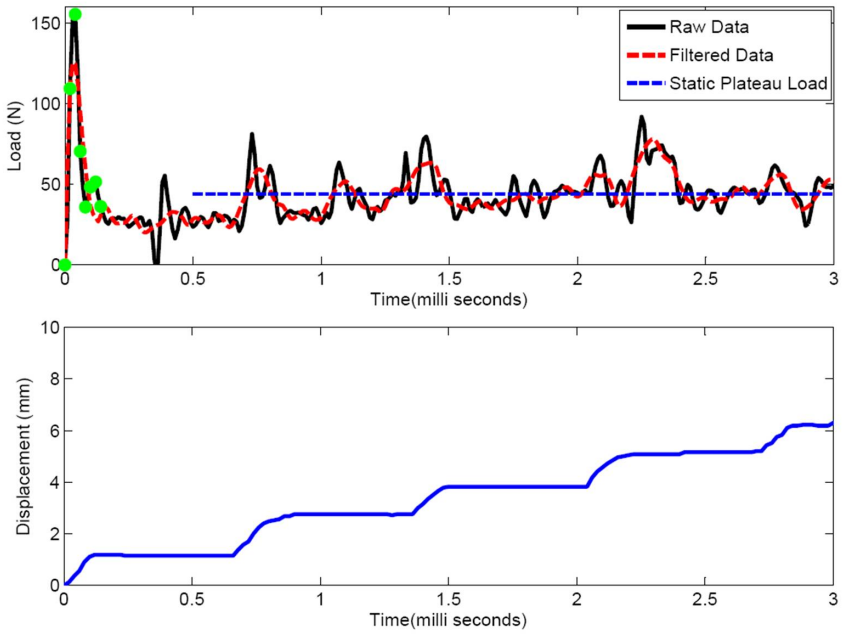

Figure 3.5: Plot showing the initial deformation response of the 3-cell specimen under dynamic crush loading using the WLD method. Load-time plot (top) and ramp-rest displacement of the transmitter bar (bottom). Observe that the crushing takes place during successive ramping phases. The first ramp ends at $t = 0.14$ milliseconds (ms). The load at time $t = 0$, $t = 0.2$ ms, $t = 0.4$ ms, $t = 0.6$ ms, $t = 0.8$ ms, $t = 0.12$ ms and $t = 0.14$ ms is shown in green (top).

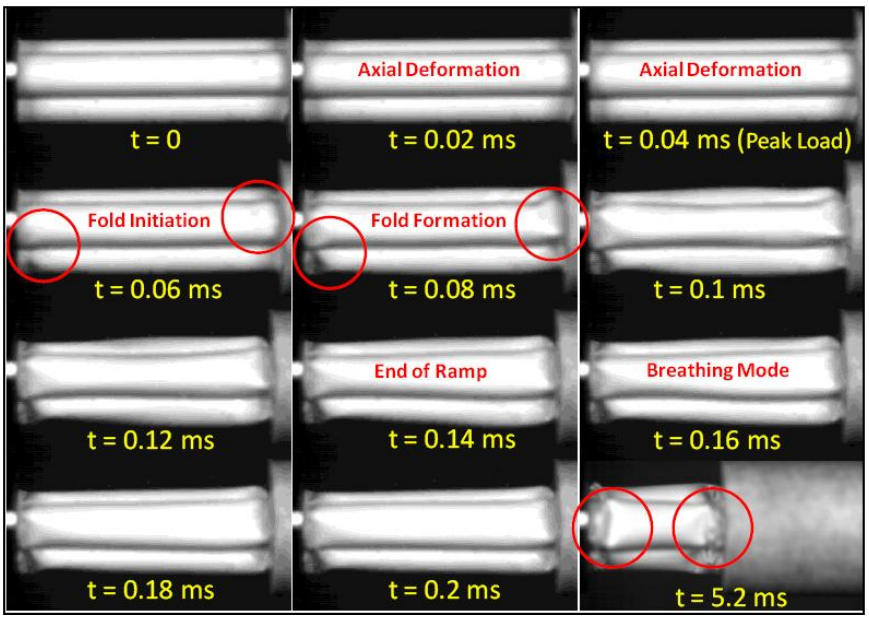

Figure 3.6: Images of the initial stages of deformation in a 3-cell specimen loaded in the WLD setup from $t = 0$ to $t = 0.2$ ms. The last image shows the deformed state of the specimen at a later time $t = 5.2$ ms. In this sample, crushing took place with folds progressively forming at either ends of the specimen

3.4 Experiments: Direct impact method

3.4.1 Setup & Procedure

To observe the behavior of honeycombs at lower crush velocities, the specimens are impacted directly with the striker bar (Figure 3.9). This experimental procedure is referred to as the *direct impact method* (DIM). The DIM is used to achieve crushing in the honeycomb cell by a striker bar moving at a uniform velocity. The specimens are bonded to the end-cap of the force sensor at its geometrical center, and positioned directly in front of the gas gun. The striker bar is then fired from the gas gun and it impacts the sample head-on with uniform velocity ($v_c \approx$ 4,000 – 5,000 mm/s). Various firing pressures are utilized as inputs for striker bar firing. A piezoelectric force sensor is instrumented on the transmitter bar. The far end of the transmitter bar is fastened tightly to a rigid, immovable steel plate to avoid any movement of

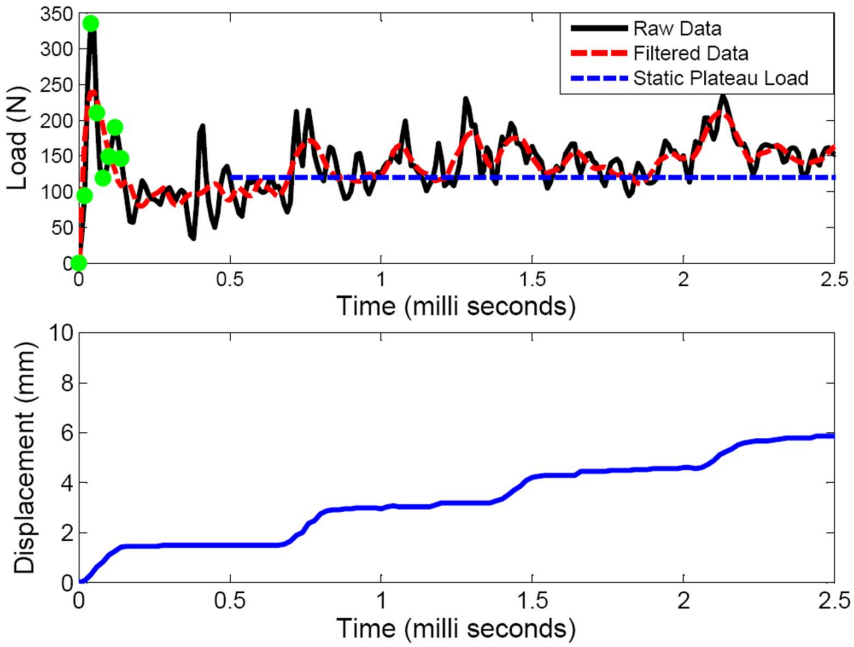

Figure 3.7: Plot showing the initial deformation response of the 7-cell specimen under dynamic crush loading using the WLD setup. Load-time plot (top) and ramp-rest displacement of the transmitter bar (bottom). Observe that the crushing takes place during successive ramping phases. The first ramp ends at $t = 0.14$ milliseconds (ms). The load at time $t = 0$, $t = 0.2$ ms, $t = 0.4$ ms, $t = 0.6$ ms, $t = 0.8$ ms, $t = 0.12$ ms and $t = 0.14$ ms is shown in green (top).

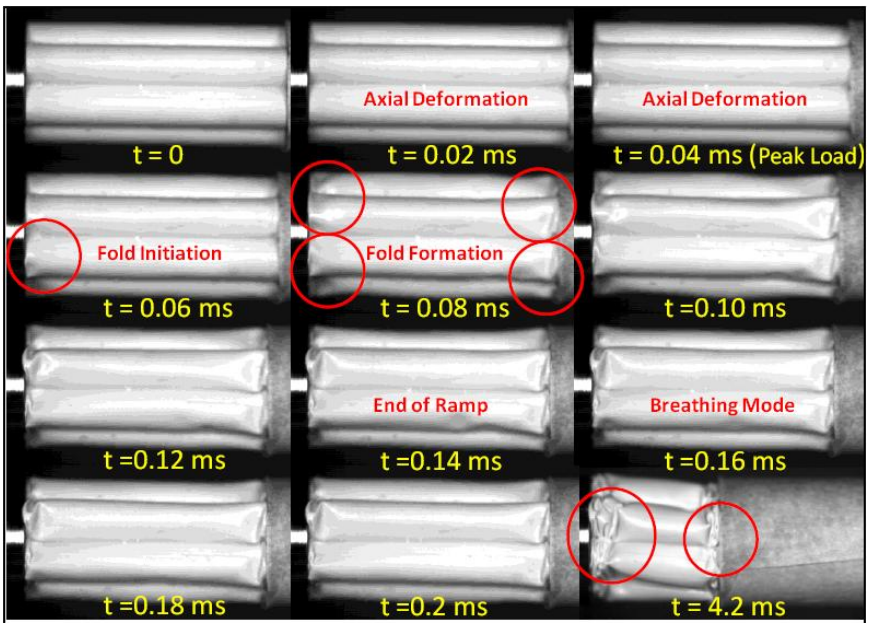

Figure 3.8: Images of the initial stages of deformation in a 7-cell specimen loaded in the WLD setup from $t = 0$ to $t = 0.2$ ms. The last image shows the deformed state of the specimen at a later time $t = 4.2$ ms. In this sample, crushing took place with folds progressively forming at either ends of the specimen

the bar before the specimen has crushed completely. The DIM produces lower crush velocities than the WLD. Between the WLD and DIM, a disparate range of crush velocities can be obtained.

3.4.2 Results

During the initial stages of deformation of the 3-cell and 7-cell specimens loaded by the DIM, the load rises nearly linearly during the stage where the deformation is dominated by the axial motion with little or no radial deformation. For the 3-cell specimens, it is observed that when the first fold initiates at the crushing end, there is a prominent peak at the end of the initial rise (Figure 3.10). In contrast, there is no peak at the end of the initial rise when the fold formation initiates at the far end of the specimen (Figure 3.11). For the 7-cell specimens, the load plot and the images from the high speed camera are provided in Figure 3.12. Here, there is no prominent

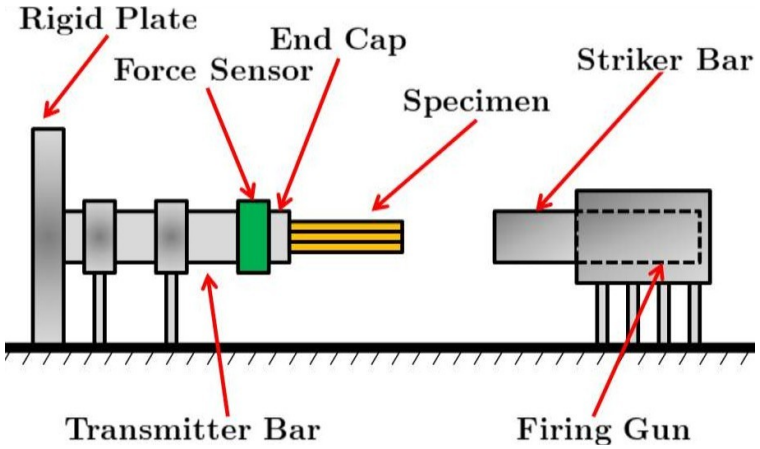

Figure 3.9: Schematic showing the setup for the direct impact method. The honeycomb specimen is positioned sufficiently close to and directly in front of the striker bar. The specimen is bonded to the end cap of the force sensor.

peak at the end of the initial region. Since collapse due to fold formation results in a drop in the crush load, the effect of fold formation at a particular end has an effect on the presence or absence of a peak in the load history that is recorded by the force sensor at the far end of the specimen. If folding initiates at the far end of the specimen, the drop in load is instantly captured by the force sensor, as the far end is in contact with it. Thus, no prominent peak is seen in this case. During crushing at high velocities, the specimen is not in dynamic equilibrium. If the fold formation starts at the impact end, the effect of this collapse does not reflect immediately at the far end of the specimen, which is still stiff. Therefore, a prominent peak is seen at the end of the initial region if fold initiation takes place at the impacted end of the specimen. Soon after the initial rise, fold formation occurs causing the load to drop. This pattern is observed for both 3-cell and 7-cell specimens. Thereafter, as the striker bar is crushing the specimen, the folding progresses from the fold initiation end to over the length of the specimen. The crush load measured for the 3-cell specimens is 51 $\pm$ 7 N (compared to the static crush load of 44 $\pm$ 4 N) while that for the 7-cell specimen is 157 $\pm$ 15 N compared to the static crush load of 120 $\pm$ 7 N). The mean crush load value is calculated as the integral average of points in the plateau region

and the uncertainty is the standard deviation of the crush load.

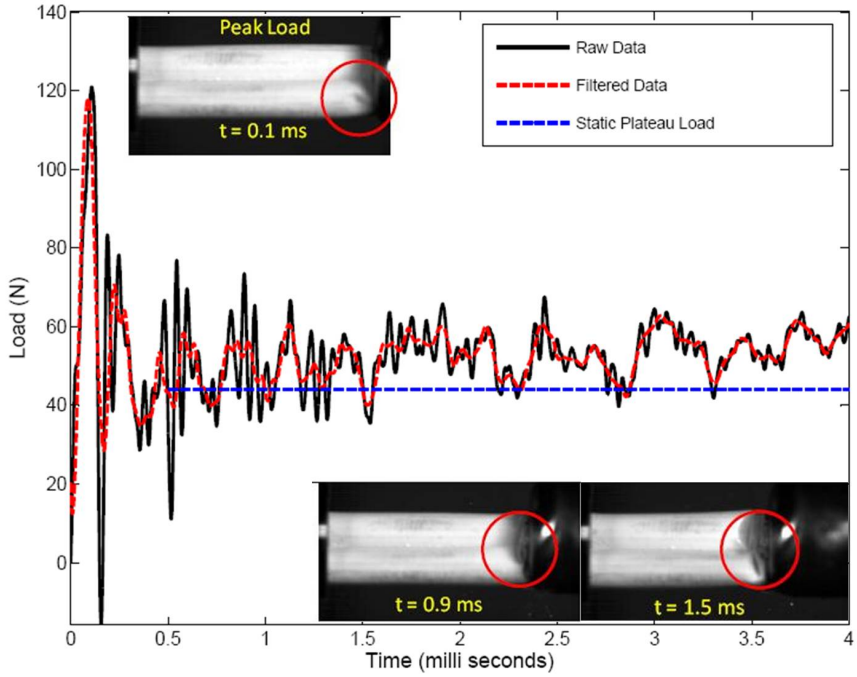

Figure 3.10: Load-time plot of the 3-cell specimen when impacted directly by the striker bar. The first fold occurs at the impact end and clear peak is observed at 0.1 ms. The fold formation continues progressively from the impact end of the specimen as the striker bar crushes the specimen.

3.5 Finite Element Model

3.5.1 Introduction

Finite element (FE) analysis is carried out using the commercially available software ABAQUS® to simulate the dynamic axial crush response of the 3-cell and 7-cell honeycombs in the out of plane direction. Here, 3-cell and 7-cell honeycomb specimens are modeled as uniform circular shells with the average measured cell dimensions. In the honeycomb specimens, each cell is in contact with its neighbor through outer wall to wall adhesion. It is assumed that during dynamic crushing, there is no delamination at the contact surfaces. Therefore, the FE model considers the contact site to be composed of a single unit of adhesion length (l) 250 μm with double wall thick-

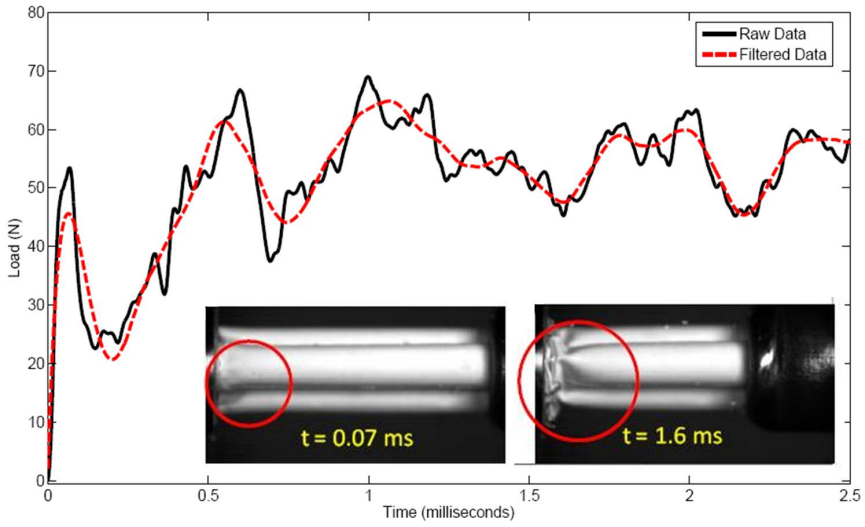

Figure 3.11: Load-time plot of a 3-cell specimen when directly impacted by a striker bar. There is no prominent peak. The first fold starts soon after the linear region ends ($t = 0.07$ ms) at the far end of the specimen. Folds continue to form progressively from the far end of the specimen.

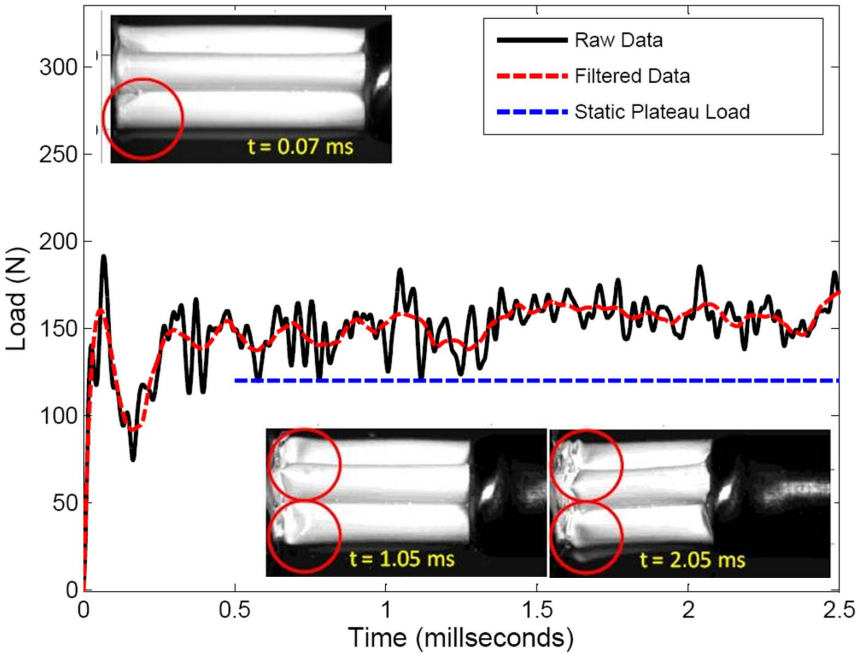

Figure 3.12: Load-time plot of a 7-cell specimen when directly impacted by a striker bar. The first fold starts soon after the linear region ends ($t = 0.07$ ms) at the far end of the specimen. Folds continue to form progressively from the far end of the specimen.

ness (t_D) 160 μm. A uniform finite element mesh is generated using linear 4-noded S4R elements with the elements having an aspect ratio ≈ 1. A convergence study (with respect to the plateau load) was conducted and the results presented use the converged mesh. The model contained 125 elements along the axial length and 60 elements along the circumference. The 3-cell model contains 22,696 elements and the 7-cell model contains 52,959 elements.

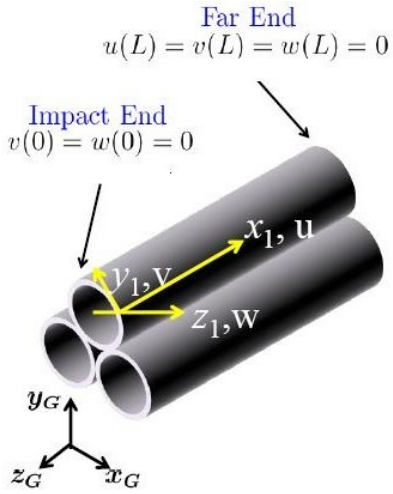

Figure 3.13: Diagram showing the boundary conditions used on the honeycomb during eigenbuckling analysis. These boundary conditions are also used for crush simulations. x_1, y_1 and z_1 are the local shell co-ordinates on a single cell corresponding to axial (u), circumferential (v) and radial (w) displacements. x_G, y_G and z_G are the global co-ordinates for the model.

3.5.2 Eigenbuckling Analysis

Shell structural response is influenced by unintended geometrical imperfections, such as out-of-roundness, non-uniform wall thickness and uncertain boundary conditions that produce non-uniformities in load. Amongst these, geometrical imperfections play a major role as is well established in the shell buckling literature (Babcock (1983), Brush & Almroth (1975)). Therefore, the current models must account for geometric imperfections present in the honeycomb specimens. The imperfect geometry is modeled as perfect cylinders that have been perturbed by a linear combi-

nation of the eigenbuckling modes of the honeycomb. Mathematically, if the buckling mode shapes are represented as $u_n(x_l, y_l) = \phi_n(x_l, y_l)$, $v_n(x_l, y_l) = \psi_n(x_l, y_l)$ and $w_n(x_l, y_l) = \chi_n(x_l, y_l)$ (where u, v and w denote displacements along the axial, circumferential and radial directions respectively), then the location of a point on the perfect shell mid-plane with coordinates, $(X_l, Y_l, 0)$ is perturbed to new coordinates (X_l^P, Y_l^P, Z_l^P) where $X_l^P = X_l + \sum_{i=1}^{N} A_i\phi_i$, $Y_l^P = Y_l + \sum_{j=1}^{N} B_j\psi_j$ and $Z_l^P = \sum_{k=1}^{N} C_k\chi_k$. The shell local axes, x_l, y_l and z_l are indicated in Figure 3.13, and the symbols A_i, B_j and C_k are the amplitudes of the perturbations. Linear buckling analysis is conducted in ABAQUS/Standard to extract the eigenbuckling mode shapes for the 3-cell and 7-cell models. The purpose is to use these modes to seed the perfect geometry to arrive at a model with geometrical imperfections, as the specimens used in the experiment are not geometrically perfect and also their initial shape cannot be measured with sufficient ease and accuracy. The boundary conditions (Figure 3.13) imposed here are as follows. The impact end surface of the cell is constrained in translation along the in-plane direction (x and y) and the far end surface of the cell is constrained in displacement along all three translational degrees of freedom (x, y and z directions). Lanczos algorithm is used as it is most suited for solving large sparse generalized eigenvalue problems (Morris (1990)) such as linear buckling problems. Lanczos solver also is better than subspace solvers for buckling of shells in particular that have closely spaced eigenvalues. Note that all analyses reported here have used only a single eigenmode to perturb the initial geometry and therefore, strictly, one must not expect the imperfections in the model to resemble geometrical imperfections that may be present in the real structure. For every eigenmode chosen to seed the perfect geometry, a quantity called as the *imperfection amplitude* (δ) is defined. If a specimen of wall thickness t is seeded with a mode shape of maximum

radial amplitude (Δw_{max}), the imperfection amplitude is

$$\delta = \frac{\Delta w_{max}}{t} \tag{3.2}$$

The upper limit of imperfection amplitudes are obtained from the deviation from the perfect circular geometry (15% of wall thickness) in the radial direction of the specimen. The maximum values of δ are chosen such that the initial linear slope of the crush response is not significantly different from that measured from the experiment. Two eigenmodes for each of the 3-cell and 7-cell specimens were chosen as the seeding modes to perturb the perfect geometry (Figure 3.14).

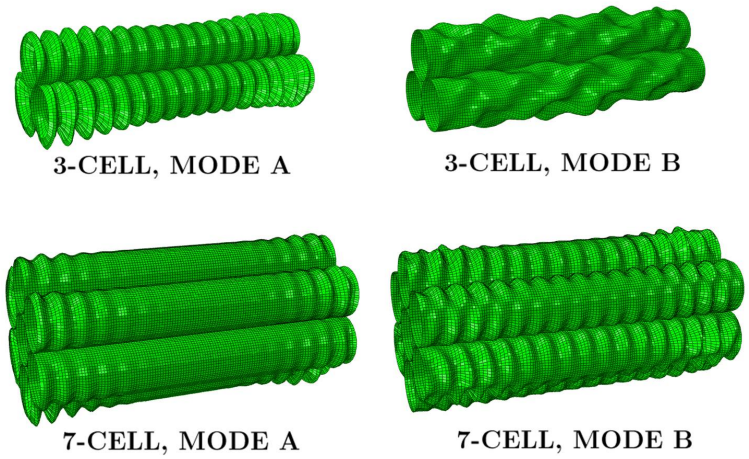

Figure 3.14: Eigenmodes for 3-cell and 7-cell honeycomb models that are chosen to perturb the mesh for explicit FE simulations. Mode A corresponds to the lowest eigenmode and Mode B is chosen corresponding to higher buckling load.

3.6 Dynamic Crush Simulation

3.6.1 Introduction

The dynamic crush FE simulation of 3-cell and 7-cell specimens is carried out in ABAQUS/Explicit. The displacement-time information for the WLD and DIM cases is taken from the experiment using the high speed images. The explicit integration

algorithm is ideal for solving large problems because the cost of computation increases linearly with problem size.

Polycarbonate is a strain rate dependent material and this dependency is incorporated in the numerical crush simulation. Mulliken & Boyce (2006) have provided the rate dependent compressive behavior of polycarbonate for strain rates 10^{-4} s^{-1} $\leq \dot{\epsilon} \leq 10^{4}$ s^{-1}. From their work, the values of true yield stress (σ_y) for various compressive strain rates are tabulated and used in the dynamic crush simulations. The initial yield stress (σ_0) is taken to be 66 MPa under static loading ($\dot{\epsilon} \approx 10^{-4}$ s^{-1}). Note that from the $\sigma_y - \dot{\epsilon}$ plot in Figure 3.15, there are two distinct regions - Region I (10^{-4} s^{-1} $\leq \dot{\epsilon} \leq 10^{2}$ s^{-1}) and Region II ($\dot{\epsilon} > 10^{2}$ s^{-1}). In Region II, the yield strength increases much faster with strain rate when compared to that in Region I. Polycarbonate does not exhibit strong strain-hardening response (for $\epsilon \leq 0.4$, which is much larger than the local strain values at cell walls during crushing). Therefore, for given strain-rate, the response past the elevated yield stress is modeled as perfectly plastic. The viscoelastic properties are not modeled because it is assumed that the stress relaxation effects are small to negligible owing to the small time duration in which the crushing takes place.

Friction coefficient of $\mu = 0.31$ is assumed for both polycarbonate-polycarbonate contact and polycarbonate-steel contact to simulate sliding behavior between these two types of surfaces during crushing. For each type of imperfections discussed in the previous section, simulations are conducted with imperfection amplitudes ranging from $\delta = 0.1\%$ up to 5%. The imperfection is applied to the shell geometry at the start of the ABAQUS/Explicit run. In the experiment, the specimen ends were held by frictional contact and this effect is neglected in the FE model. The boundary conditions used in the dynamic run are as follows: only axial movement is allowed and no rotation constraints are applied on the impact face; whereas the far end of the

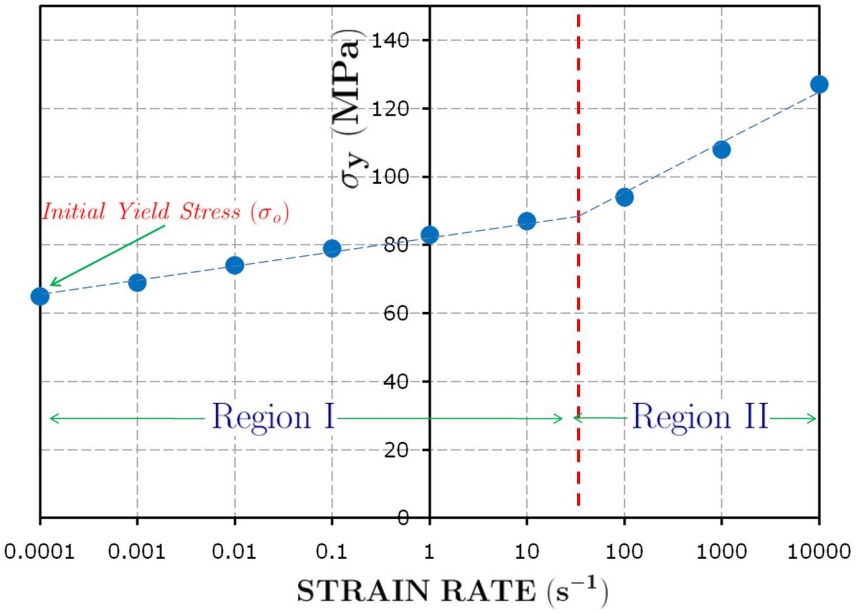

Figure 3.15: The rate dependent compressive behavior of polycarbonate taken from Mulliken & Boyce (2006). Note the two regions where polycarbonate exhibits different rate dependent behavior.

specimen is only constrained in translation. For the crush simulations, the incident bar (WLD test) and the striker bar (DIM test) are modeled with coarse mesh using hexahedral solid elements (C3D8R) with material properties of hardened steel. In the WLD simulation, the striker bar is not modeled because, (1) the displacement information from the high speed camera is known and (2) the wave propagation effects of the specimen are not significant due to high impedance mismatch between hardened steel incident bar and polycarbonate honeycomb at the interface.

In the WLD simulation, the input for the displacements prescribed for the incident bar end is a sequence of near perfect ramp-rest inputs. The actual ramp displacement measured from the experiments strictly does not vary linearly with time. Moreover, the displacement-time input for various experiments varied slightly in displacement values, but the duration of the ramp for each loading cycle was consistent. To reduce the simulation run-time, the start and end points of each ramp are averaged and only values at the end points are provided in the displacement-time input for the 3-cell

and 7-cell FE simulations. Representative crush velocity of 5,000 mm/s was used as input to the striker bar for all the 3-cell and 7-cell FE models simulating the DIM experiments. The center node along each contact strip is constrained against out of plane motion to prevent beam-like global buckling. This point constraint is valid as it does not over-constrain the structure and does not interfere with the physics of axial crushing.

3.6.2 Simulation Results and Discussion: Wave loading device (WLD) method

In the initial stages of loading, the deformation in the 3-cell and 7-cell specimens is purely axial and the load rises linearly to a peak. This observation agrees well with that seen in the experiments. Thereafter, folds appear on either sides and the load drops. The folds disappear at the far end of the specimen and the folding progressed at the impacted end. Fold formation takes place as long as the impacted end is in motion and the load rises again in the process. During the rest period, the cells are seen to exhibit hoop-like vibrational modes, similar to the ones observed in the experiment. Here, the load fluctuates about a value lower than that when the impacted end is in motion. When the next ramp step occurs, the load rises again with more fold formation. The load drops when the impacted end comes to rest. This cycle continues and the simulations run for a crush length of approximately 10 mm. For the 3-cell model, the crush load obtained from the simulation is 50.45 $\pm$ 12 N when compared to the mean crush load of 54 N measured from the experiment. The images from the simulations for 3-cell and 7-cell models are shown in Figure 3.16. For the 7-cell model, the crush load obtained is 158.8 $\pm$ 12.2 N compared to the experimental mean crush load of 159 N. The load-time and displacement-time plots for 7-cell specimen for varying imperfection amplitudes are shown in Figure 3.17. The average and standard deviation calculation for the plateau load from FE simulations

is performed only during the ramping motion of the incident bar. The mode of collapse is by concertina-diamond fold formation which is similar to the mode of collapse seen in the experiments. It is not possible to do a side by side comparison of the experiment and the simulation, since the FE analysis uses a rendition, based on initial eigenmode shaped geometrical imperfections, of the actual model. It was observed from the simulation results that the type and amplitude of imperfections had no effect on the collapse mode and little effect on the peak and crush loads. Also, irrespective of the severity of imperfections with regard to the type of modes considered, the fold initiation takes place at either end soon after the peak load is attained. These observations are encouraging and lends credence to the method of analysis that has been adopted.

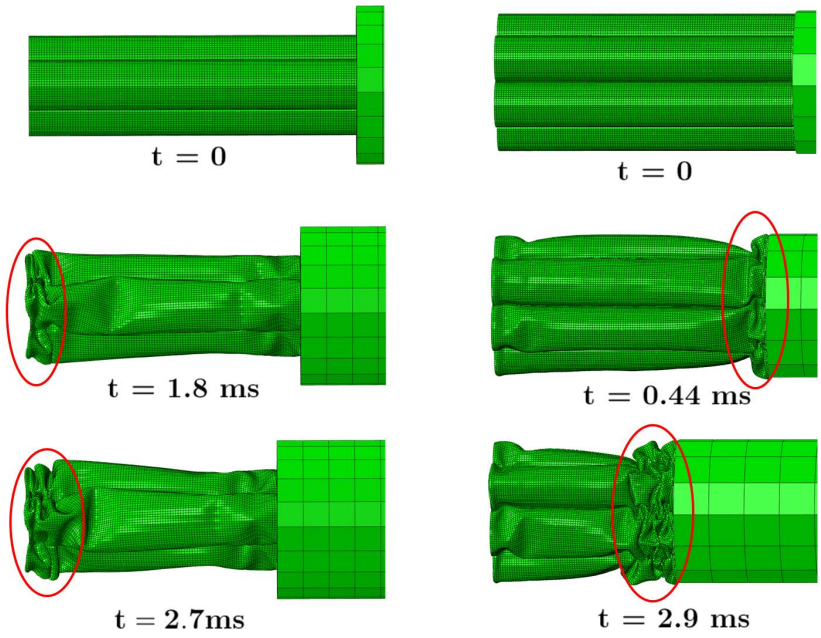

Figure 3.16: Images from the FE dynamic crush simulation of 3-cell and 7-cell models with WLD inputs. The folds appear soon after the peak load is attained. The collapse occurs through the localized concertina-diamond mode.

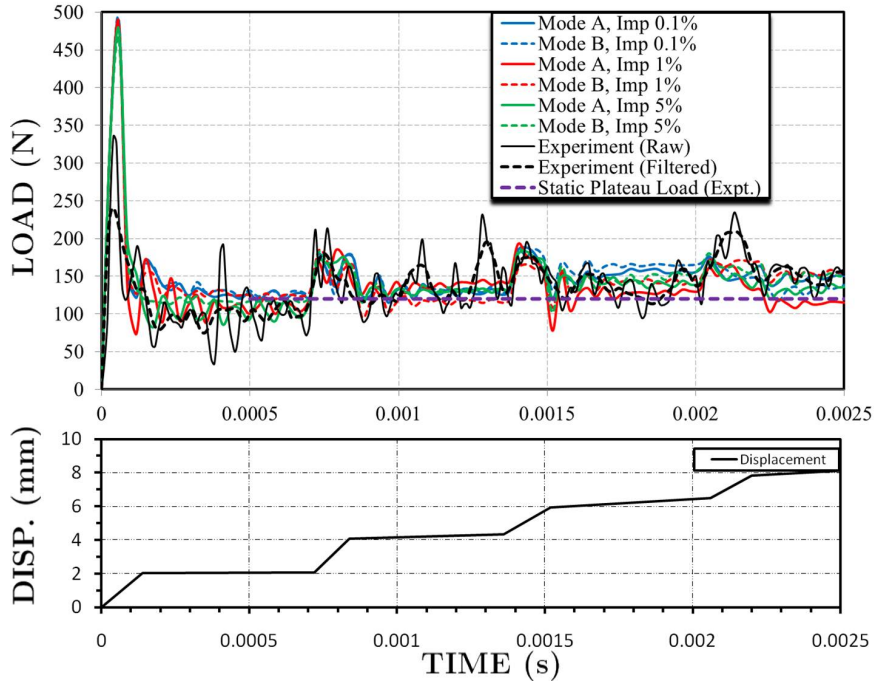

Figure 3.17: Load-time plot for 7-cell specimen FE simulation with the ramp-rest WLD input. The mean plateau load level (120 N) for static crush of 7-cell honeycomb is shown for comparison.

3.6.3 Simulation Results and Discussion: Direct impact method

During the initial stages of loading, the load rises to a peak (maximum) load. The deformation in the specimen is only axial up to this point. Folding initiated near the ends of the specimen and the load drops quickly. New folds are formed due to the constant rate of crushing and the load stabilized at an approximately constant level, which is referred to as the *crush load*. In the 3-cell model, it is seen that the impact end of the specimen which shows localized deformation, recovers elastically nearly to the original shape. The load decreases for a while immediately after the peak and stabilizes at the crush load. The folding progresses from the region where fold initiation takes place towards both the sides of the specimen. The images from the simulations for 3-cell and 7-cell models are shown in Figure 3.18. The load-time and displacement-time plot for a 7-cell model for various imperfection amplitudes are shown in Figure 3.19. For the 7-cell model, fold initiation takes place at both ends

and the specimen progressively crushes from these ends. The crush load observed for the 3-cell specimen is 50.54 ± 8.4 N compared to the experimentally measured mean crush load of 51.5 N. For the 7-cell specimen, the crush load obtained from the simulation is 148 ± 14.2 N compared to the crush load value of 157 N seen in the experiments. Hence, the estimate of crush loads during progressive collapse is close to that measured from the experiment.

It is noted that the difference in peak collapse load between simulation and experiment is large, especially in the case of the DIM study. The peak loads measured from the experiment varies significantly among specimens (from no noticeable peak, to about 190 N as seen in Figure 3.12 for the 7-cell specimen) whereas the crush load is consistent. In contrast, in the WLD case with 7-cells, the variation in the measured peak load was somewhat consistent between 330 - 400 N. One of the reasons for this difference in the peak value is due to unknown and unintended geometrical imperfections present in the sample. Furthermore, in the DIM experiment, there is uncertainty as to the angle of the striker bar with respect to its "straightness" in trajectory. This reduction in the peak collapse load due to misalignment in loading (as shown by Wilbert et al. (2011) for hexagonal aluminum honeycomb system) is another reason for large difference in the initial peak load value.

3.6.4 Variation of local strain rates and plateau stress with crush velocity

Next, variation of local strain rates with the crush velocity for the 3-cell and 7-cell models is discussed. When the honeycomb crushing occurs, the strain rates experienced by the honeycomb walls are different for varying crush velocities. From the explicit FE simulations carried out on the 3-cell and 7-cell models, several locations are monitored on the cell walls where severe fold formation occurs. For a given model and crush velocity, strain rates are found to not differ by a significant amount in magnitude. At a typical such location, the time histories of these quantities are averaged,

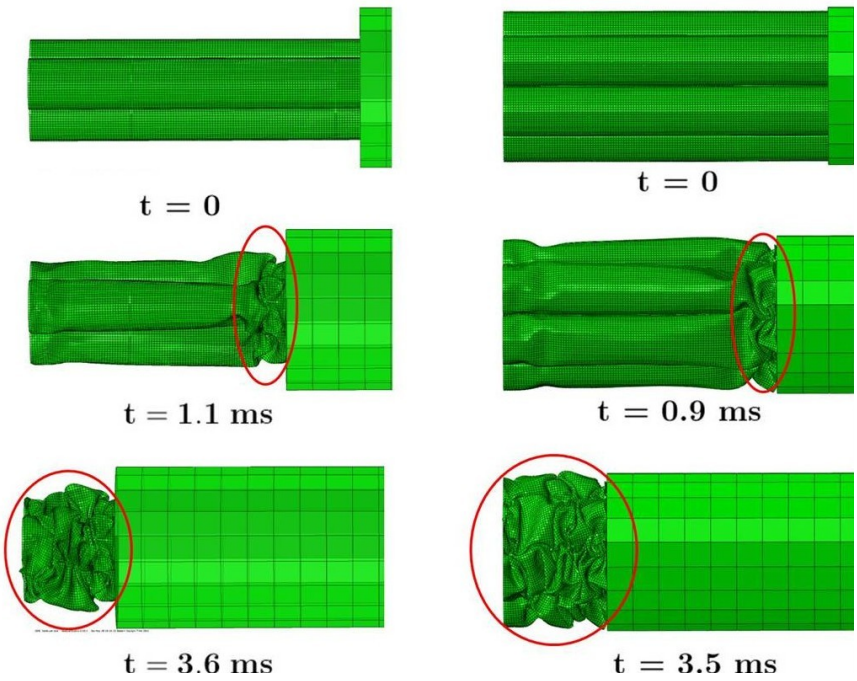

Figure 3.18: Images from the FE dynamic crush simulation of 3-cell and 7-cell models with loading velocity 5,000 mm/s (DIM simulation). Crushing occurs through the concertina-diamond mode.

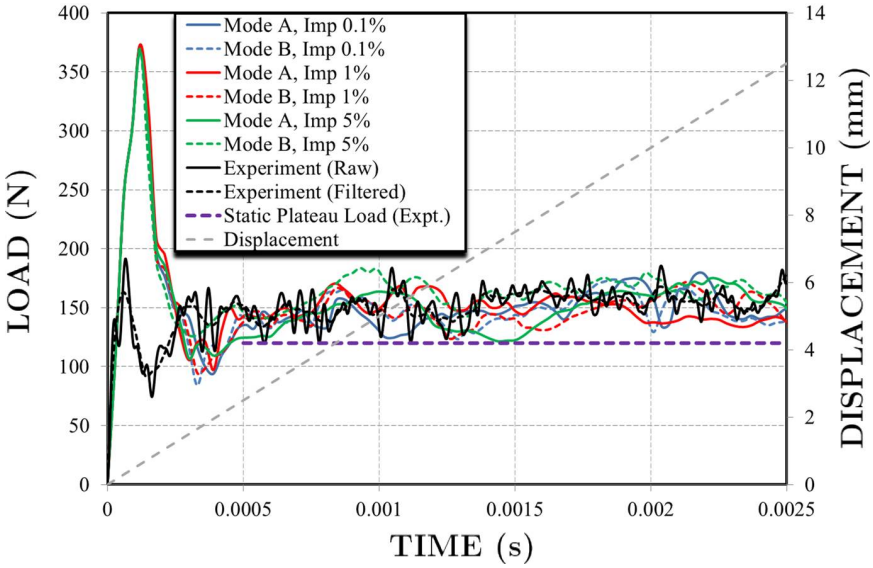

Figure 3.19: Load-time plot obtained from FE simulation for 7-cell specimen being crushed at the rate of 5,000 mm/s (DIM simulation). The mean plateau load level (120 N) for static crush of 7-cell honeycomb is shown for comparison.

and the variation of (averaged) strain rates and plateau stress with various crush velocities are provided in Figure 3.21, along with the maximum amplitudes of strain rates over the time history. The results show that with an increase in crush velocity, strain rate and crush loads increase. At such locations, the bending and membrane strains were found to increase with increase in crush velocity. Furthermore, the model predictions are seen to agree with the experimental data corresponding to the crush velocity of 5,000 mm/s. It is also observed that for a given crush velocity, the strain rate values for a 3-cell and 7-cell model are not significantly different, suggesting that results for specimens with a larger number of cells would be similar. This is verified with DIM simulations of 3-cell, 4-cell, 7-cell, 13-cell and 19-cell models that were each crushed at a velocity of 5,000 mm/s. A plot showing normalized values (i.e. load per cell) of the crush and peak loads for the mentioned cell numbers, is shown in Figure 3.20. It is observed that the plateau load per cell for the 7-cell model is higher than that for the 3-cell model by $\approx 40\%$ Ḟor the 13-cell and 19-cell specimens, the plateau load per cell is $\approx 8\%$ and $\approx 20\%$ respectively higher than the 7-cell specimen, suggesting that this load asymptotes to a constant value of ≈ 24 N as can be seen in Figure 3.20.

With reference to Figure 3.21, note that for an increase in crush velocities, the normalized plateau stress (calculated as $P_{plateau}/NAE$ where $P_{plateau}$ is the average plateau load, $A = 2\pi Rt$ is the true contact area, E is the static Young's modulus of polycarbonate and N is the number of cells in the specimen) slightly increases indicating that rate effects do play a role in the axial crush response. The normalized plateau stress calculated from the static 3-cell and 7-cell experiments are also provided in Figure 3.21 to enable comparison with the dynamic crush experiment DIM. The normalized plateau stress values for static crush experiments are lower than the DIM experiment (at crush velocity 5,000 mm/s) and FE predictions provided, thus indicating the presence of rate effects. More specifically, comparing the dynamic crushing

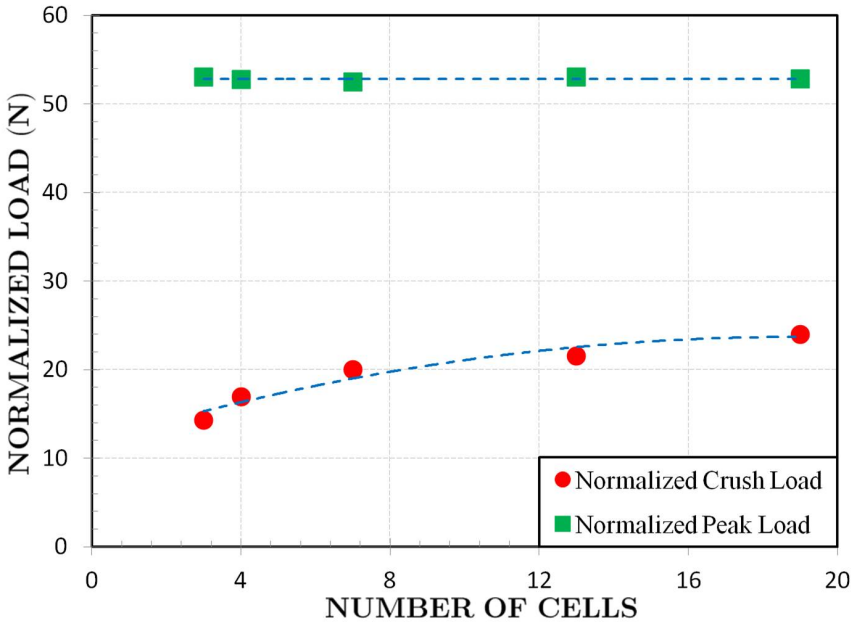

Figure 3.20: Plot showing the FE simulated crush and peak load values that are normalized by number of cells for 3-cell, 4-cell, 7-cell, 13-cell and 19-cell specimens. Each of the specimens were crushed at the rate of 5,000 mm/s (DIM simulation) to study the effect of cells-per-specimen on the crush and peak load.

(at 5,000 mm/s to the static crushing), the Figure 3.21 shows only a slight increase for the 3-cell specimen, i.e. an increase of about 5% compared to an increase of about 10% for the 7-cell specimen. The comparatively higher increase in load for the 7-cell specimen is due to the higher degree of lateral constraint that is provided to the cells as the number of cells increase. Figure 3.22 shows the contribution of a single cell in a 3-cell model and an outer layer and innermost layer cell in a 7-cell model when these corresponding 3-cell and 7-cell specimens were crushed at a uniform velocity of 5,000 mm/s. Amongst the three types of cells distinguished here, the plateau load levels is largest for the innermost cell in the 7-cell model (most constrained with 6 double wall sites along the circumference) and is lowest for a cell in the 3-cell model (least constrained with 2 double wall sites along the circumference). Moreover, the lateral constraint has the effect of slightly delaying the first failure event as can be seen from the peak loads in Figure 3.22.

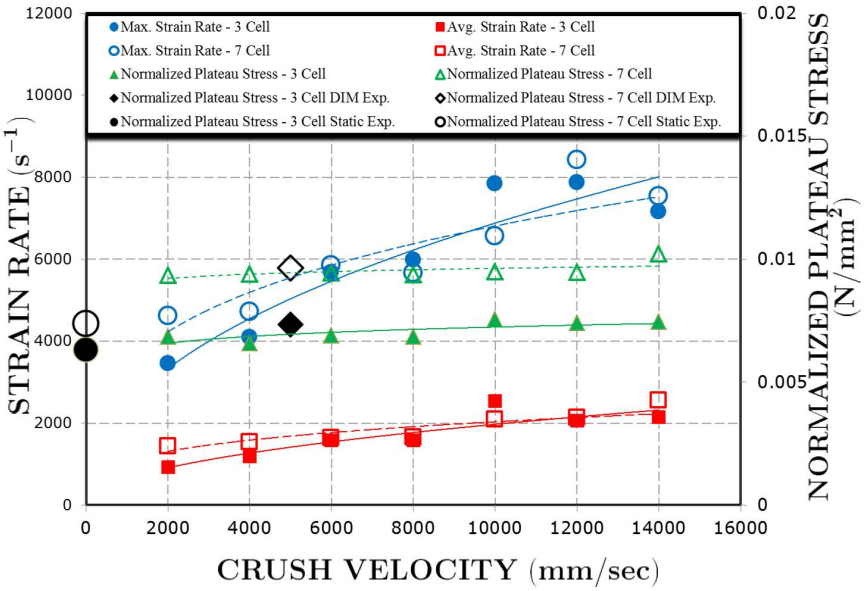

Figure 3.21: Plot showing the variation of material strain rate and normalized plateau load per cell with crush velocity for 3 and 7-cell models. For crush velocity of 5,000 mm/s (Direct impact method), the experimental normalized plateau stresses for the 3 and 7-cell are also shown. The normalized plateau stress, a non-dimensional quantity, is calculated as $P_{plateau}/NAE$ where $P_{plateau}$ is the plateau load, $A = 2\pi Rt$ is the true contact area and E is the polycarbonate Young's modulus for an N-cell honeycomb. Also shown is the normalized plateau stress for 3-cell and 7-cell static crush experiments.

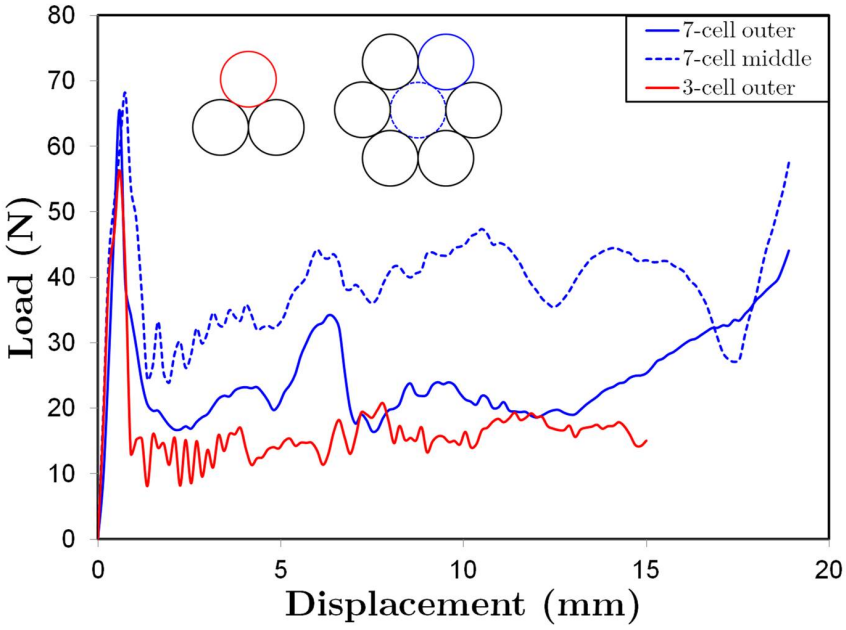

Figure 3.22: Plot showing the load response for the outer cell for a 3-cell model and outer and innermost cells in 7-cell model and pointing towards the influence of lateral constraints at the double-wall site on the plateau load.

3.7 Conclusions

The crush response of 3-cell and 7-cell circular cell honeycombs was studied using two methods - the wave loading device (WLD) method and the Direct impact method (DIM). The crush velocities seen in the WLD method are higher ($\approx$ 12,000 mm/s) compared to those in the DIM ($\approx$ 5,000 mm/s). The collapse of 3-cell and 7-cell specimens occurred over a constant state of crush load at these crush velocities. Mean crush loads for the specimens measured from the WLD experiments were slightly higher compared to that measured from DIM experiments. Moreover, higher crush load levels were measured in the DIM experiment for 3-cell and 7-cell honeycombs compared to corresponding static crush experiments, thus clearly showing the presence of rate effects in the crush response. The peak load measured from the WLD experiment was higher than that from the DIM. This is evident because the deceleration force upon impact increases when the crush velocity is larger. The crush

initiation took place at one or both ends of the specimen. The mode of collapse of the honeycombs was through localized concertina-diamond fold formation that progressively propagated from the specimen ends until the entire specimen had crushed. A series of FE simulations were conducted using eigenbuckling modes to approximate the imperfect geometry of the honeycomb. These simulations satisfactorily captured deformation features observed in the experiment, thus providing a meaningful way to estimate the energy absorption of clusters of cells. Beyond the stiff initial response, the load at which progressive collapse took place was found to be fairly close to that measured from the experiments. Moreover, the plateau load occurring with the concertina-diamond mode of collapse was found to be insensitive to the type and amount of geometrical imperfections.

CHAPTER IV

Static Compression Response of Filled Honeycombs: Inplane direction

4.1 Introduction

[1] In the previous chapter, the dynamic axial crushing of 3-cell and 7-cell honeycombs was presented. The focus of this chapter is the study of energy absorption under uniaxial inplane compression of a "composite" circular cell honeycomb (D'Mello & Waas (2013)). The base honeycomb structure is filled with an elastomer (PDMS) and these specimens are referred to as *filled specimens* to distinguish these from the base unfilled honeycomb which are referred to as *unfilled specimens*. The static out-of-plane crush loading of a composite honeycomb with polyurethane as filler material has been reported previously in D'Mello & Waas (2012). The circular cell polycarbonate honeycomb panels used in the present work were obtained from Plascore Inc., Zealand, MI, USA.

[1]Parts of this chapter are published in D'Mello, R. J. & Waas, A. M., "Inplane crush response and energy absorption of circular cell honeycomb filled with elastomer," *Composite Structures*, 106, pp. 491-501, 2013.

4.2 Inplane crushing of unfilled honeycomb

In Chapter II, the inplane static crush response of unfilled honeycomb was presented. For sake of clarity, the inplane crushing of 11×11 size honeycomb is briefly discussed here. The mode of failure and crush load from this experiment are used for comparison purposes with the filled crush experiment to follow.

Unfilled honeycombs of size 11×11 are subjected to inplane compression at a loading rate of 0.033 mm/sec in an INSTRON screw driven loading device. The specimen is compressed between a steel plate attached to the machine base and an aluminum platen screwed to the load cell that is attached to the moving crosshead of the INSTRON machine. The faces of the bottom plate and loading platen in contact with the honeycomb are lubricated to minimize the influence of friction on the compression response. The load vs. displacement plot along with the deformed shape is shown in Figure 4.1. During the initial stages of compression, the cell geometry deviates from circular shape to one which is symmetric about vertical and horizontal axes passing through the center. This doubly-symmetric deformation mode occurs uniformly in each of the cells in the specimen. The accompanying load response is linear and corresponds to the structure's *prebuckling* deformation regime.

Localization in the form of row-collapse initiates across two rows at a crush distance of 2.8 mm (equivalent to a macroscopic strain value of 0.07). In the collapsing layers, the doubly-symmetric deformation mode in the cells changes to an unsymmetric shear-type collapse mode. The first localization zone varies from one sample to another, and is controlled by the severity of unintended geometrical imperfections present in the structure. The load drops slightly until complete collapse of the layer has occurred. The load slightly rises and starts to drop once again when the localization spreads to the adjacent row. Similarly, new rows progressively collapse and this process occurs over a fairly constant load called the *plateau load*. The plateau region occurs in the *postbuckling* regime of the compression response. The row-wise

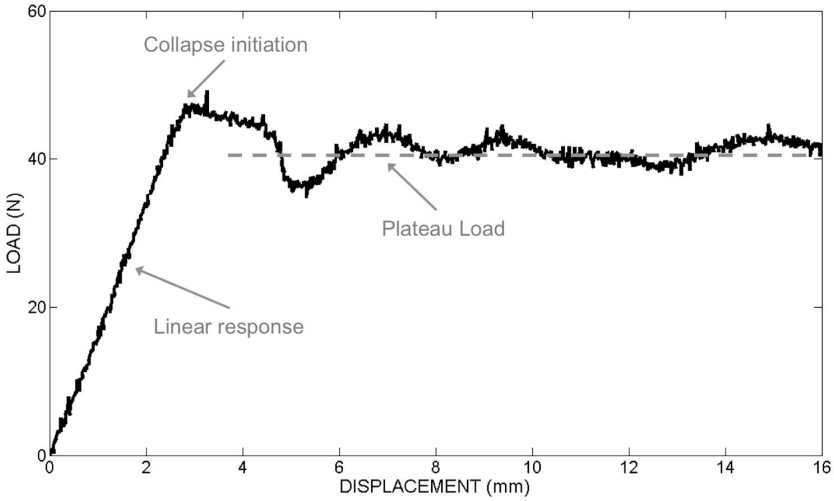

Figure 4.1: Load-displacement plot obtained from the static inplane compression of an 11×11 size unfilled honeycomb specimen.

collapse of the unfilled honeycomb is shown in Figure 4.2. The plateau load is found to be approximately 41 N. The plateau load is the reaction load measured by the load cell in the experiment, and thus represents an integral average of the load over the cross-sectional area of the specimen. The lengthy plateau region enables large amount of energy absorption, thus making these materials attractive for energy absorption applications where weight is critical. Detailed accounts of the mechanics of in-plane crushing of circular cell polycarbonate honeycomb are provided by Papka & Kyriakides (1998) and Chung & Waas (1999) for quasi-static crushing and by Chung & Waas (2002a) and Chung & Waas (2002b) for impact crushing and also under biaxial loads.

4.3 Inplane crush response of filled honeycomb

4.3.1 Introduction

Using the unfilled honeycomb as a benchmark, any increase in the load carrying capacity and improvement in the energy absorption capability can be investigated for similar specimens that are filled with soft elastomer. This section describes the

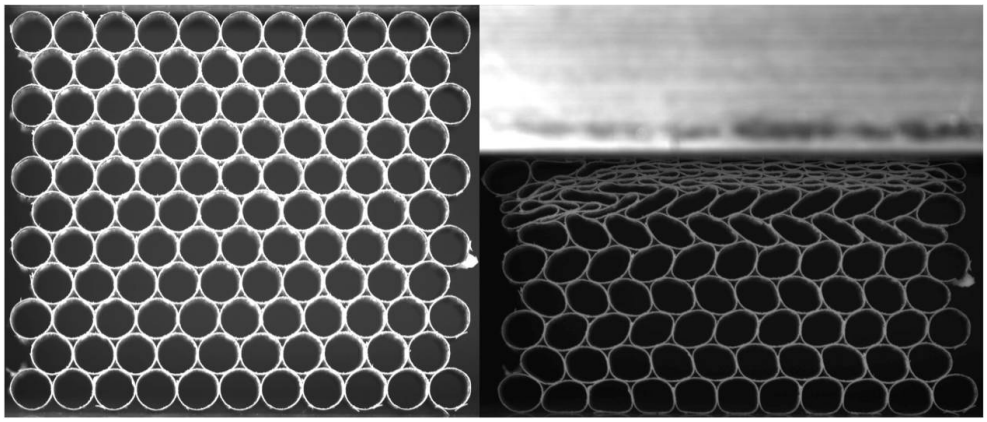

Figure 4.2: Row-wise collapse (right) mode in inplane compression of unfilled honeycomb (left).

inplane compression of polycarbonate honeycomb that is filled with PDMS elastomer. First, honeycomb specimens of size 11×11 are filled with the PDMS mix and the air bubbles removed in a vacuum chamber. Next, the sample is heated at 100°C for 45 minutes and left to cure for two days at room temperature. Inspection of the cured specimens reveals that no adhesion exists between the PDMS filler and the surrounding polycarbonate cell walls. The weight of the filled 11×11 size specimen is 43.5 g and is approximately 13-fold higher than the weight of the unfilled 11×11 size specimen. The filled specimens are subjected to inplane compression (crush rate of 0.033 mm/sec) using an INSTRON machine. The specimen is held in the INSTRON machine similar to the unfilled honeycomb experiment, that is, between flat steel plate attached to the machine base and an aluminum platen screwed to the load cell attached to the moving crosshead of the INSTRON machine. The faces of the base plate and loading platen in contact with the specimen at the bottom and top respectively, are lubricated to minimize the influence of friction on the compression response of the filled honeycomb specimen. Load is recorded at 10 Hz using a 1,000 lbf capacity load cell. The experiments conducted on several samples were consistent in the load vs. deformation response. The load vs. displacement plots obtained from these uniaxial compression experiments are shown in Figure 4.3. The deformation

sequence for Sample # 1 in Figure 4.3 is shown in Figure 4.4. Two distinct deformation regimes are identified with regard to Figure 4.3 - the *pre-failure* and *failure* regime that are described next.

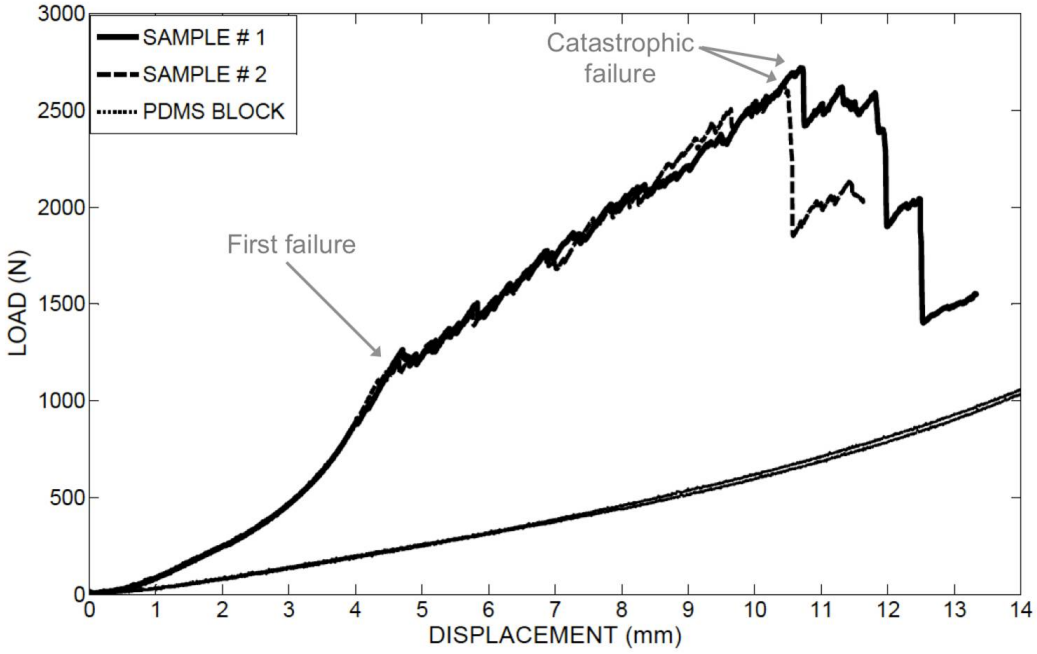

Figure 4.3: Load vs. displacement plot of the compression response of 11×11 size filled honeycomb. Also shown is the response of a PDMS block of identical size. To make a comparison, the plateau load in the 11×11 size unfilled honeycomb is approximately 42 N.

4.3.2 Pre-failure regime

During the initial stages of loading, cells deviate from circular geometry and deform to a doubly symmetric shape; and this deformation pattern is fairly homogeneous across all the cells. Note that this deformation pattern is similar to that seen in the unfilled specimen's prebuckling response. This deformation regime is seen up to a crush distance of approximately 4.5 mm, and is referred to as the *pre-failure region* (before the onset of failure). In the pre-failure region, the specimen response is nonlinear unlike that observed in the unfilled honeycomb where the response was fairly

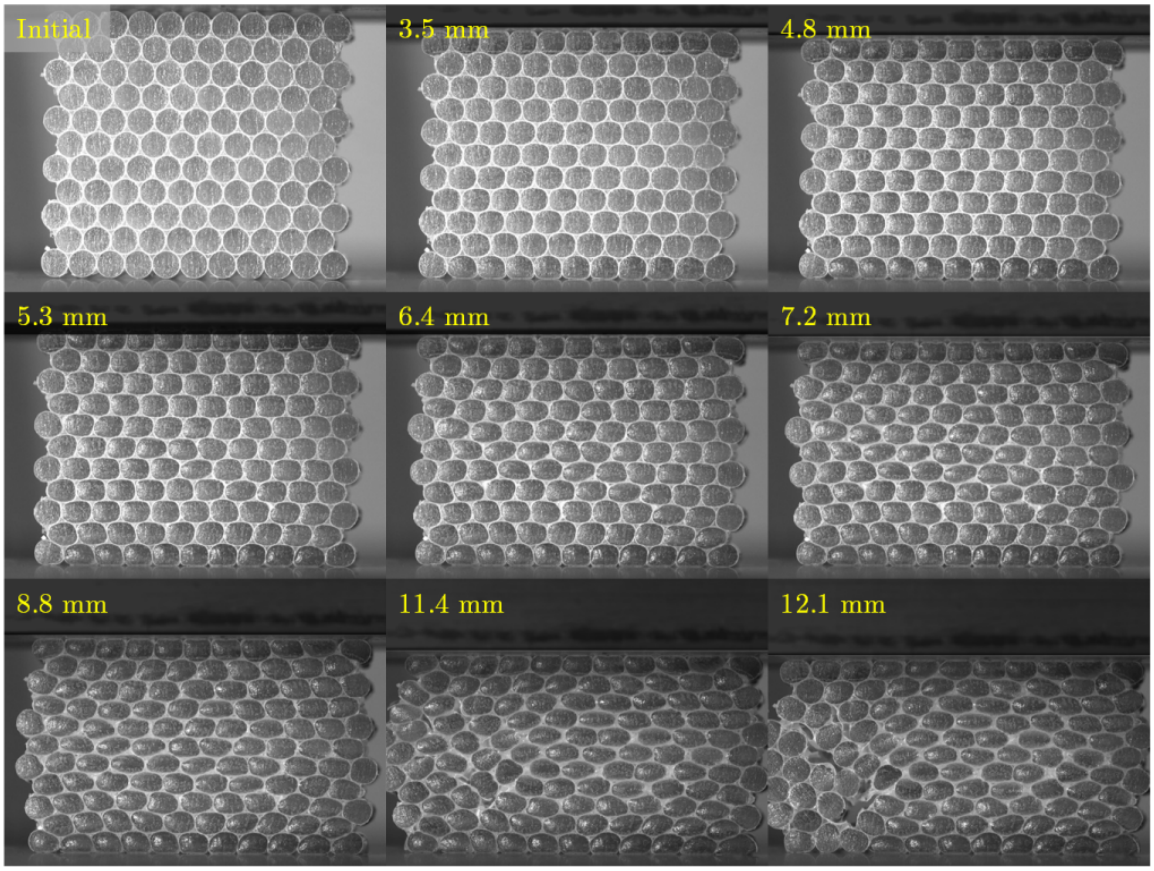

Figure 4.4: Deformation sequence of a 11×11 size filled honeycomb

linear. This observation suggests that the non-linear response of the PDMS polymer strongly influences the overall non-linear behavior of the filled specimen. From the images, it is observed that with increasing crush distance, the PDMS filler bulges outwards along the out-of-plane direction owing to the incompressibility of the polymer and due to lack of out-of-plane constraints on the honeycomb face.

4.3.3 Failure regime

The presence of the filler prevents the row-wise collapse of cells. This resistance to cell wall collapse delays the onset of failure in the filled honeycomb by a mechanism different from row-wise collapse that was observed in the unfilled honeycomb. The onset of failure occurs at a crush distance of approximately 4.5 mm with localization

near the center of the specimen. The first and second localization sites for a specimen are shown in Figure 4.5. Cells near the localization site rotate (Figure 4.6). The behavior of cells in the vicinity of first failure is discussed later using a digital image correlation study. The localization is triggered by longitudinal wall tearing (mode I cracking) near the double wall contact site and is accompanied by an audible sound. On a few samples, cell wall-to-wall debonding is also observed along with the predominant wall tearing failure. The load vs. displacement plot shows significant reduction in the stiffness. Across various experimental trials, the first localization site varies from sample to sample but is predominantly seen near the center rows of the specimen. With increasing crush distance, the localized cell-to-cell failure and longitudinal tearing spreads to several disconnected regions in the specimen. Each localized failure is characterized by a slight drop in the load and is seen in Figure 4.3, for displacement values of 4.5 mm and higher. During the spread of damage across the specimen, the stiffness is fairly constant. As seen from the images, the filler material does not relax considerably, thereby maintaining the overall positive stiffness in this regime.

In the final stages, the localized failure regions spread across the specimen until a weak-plane (oriented at 60° with the horizontal) is formed that is favorable for global failure in shear. The specimen fails catastrophically with prominent failure planes forming an X shape. An image of the failed specimen is shown in Figure 4.7. The catastrophic failure event is accompanied by a sharp load drop and this event occurs at a crush distance of 10.8 mm (macroscopic strain value of about 0.28). The test is terminated soon after the large drop in load. The individual PDMS filler material (within cells) relax to their undeformed configuration.

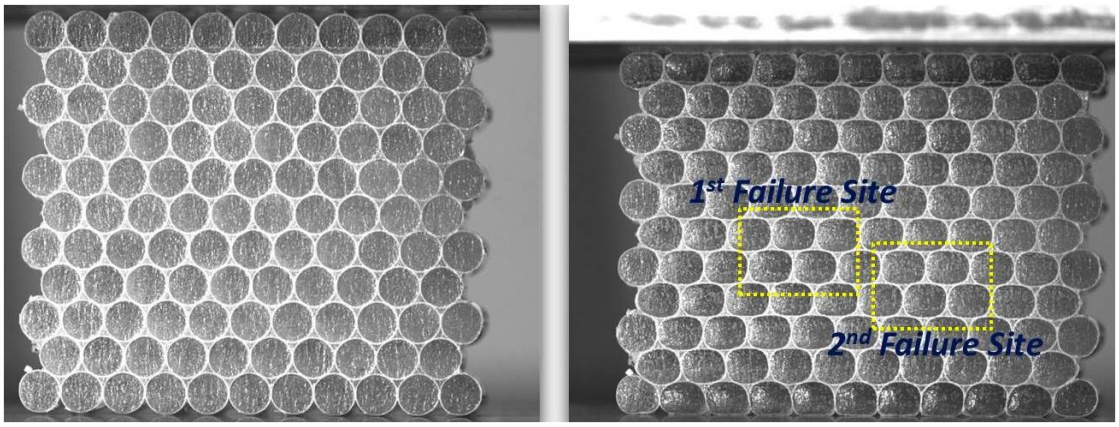

Figure 4.5: Undeformed filled specimen (left). Image prior to first failure showing first and second localization sites (right). Notice the doubly-symmetric deformation mode in the cells (right).

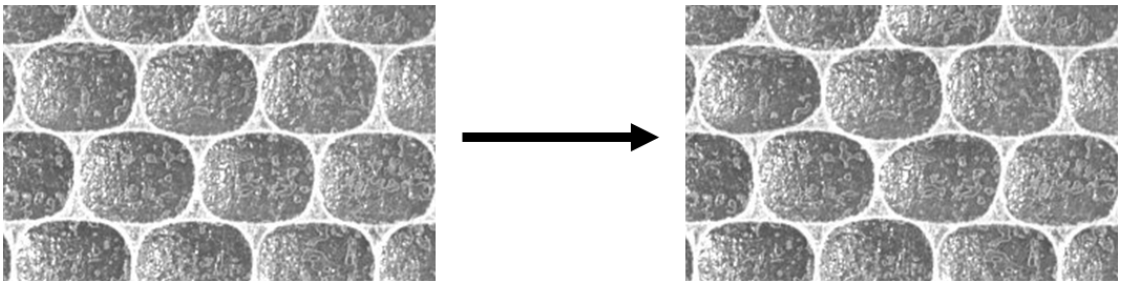

Figure 4.6: Images showing the first localization site prior to localization (left) and at the onset of localization (right).

4.3.4 Synergistic response & energy absorption

The fundamental differences in energy dissipation mechanisms between the filled and unfilled specimens is presented. In the unfilled specimens, once localization due to row collapse starts, the energy dissipated is independent of crush distance as collapse occurs at a somewhat constant load level (Figure 4.1). However, in the filled sample, after the onset of failure, the energy is effectively stored in the filler (stiffness is positive) even though some dissipation occurs during progressive damage in the cells (Figure 4.3). Thus, the rate of energy stored in the filler material is greater than that dissipated in wall fracturing and due to relaxation in the filler material as a

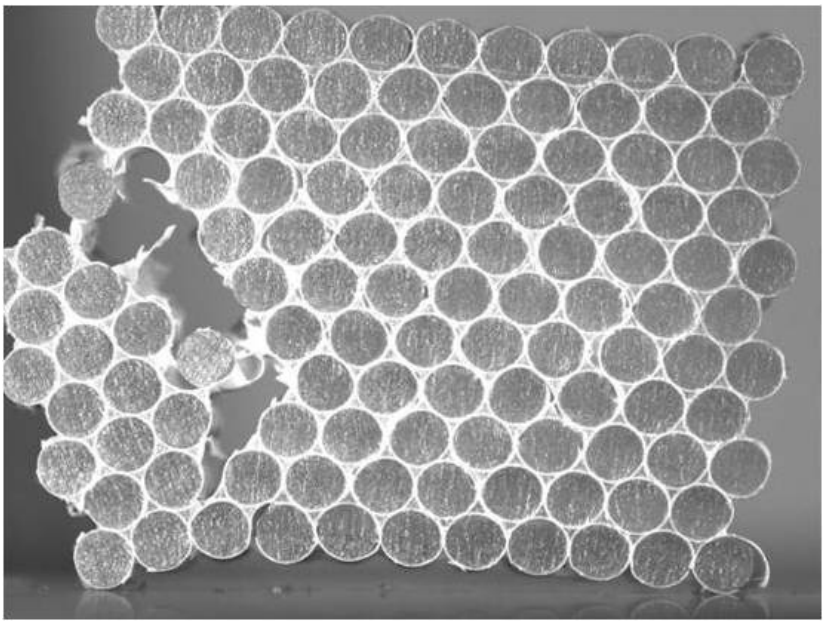

Figure 4.7: Specimen unloaded immediately after catastrophic failure. Notice the global shear-like failure to the left.

consequence of localization. Therefore, in the filled specimens, large amounts of strain energy is first stored in two stages (a) from start to first failure (nonlinear stiffness region) and (b) first-failure regime to catastrophic regime (stiffness is constant). A major portion of the stored energy is at once dissipated during catastrophic failure.

Comparing the deformation response of the individual components as a function of the end-crushing distance up to catastrophic failure, it is seen that the load carried by the filled specimen is much higher compared to the sum of the loads carried by the unfilled honeycomb specimen and a PDMS block of the same volume as that of the filled specimen. This behavior points towards a synergistic effect in the load carrying capability in the filled honeycomb. The load at onset of failure is 1,100 N, roughly 24-fold higher when compared to the unfilled first failure load of 41 N. Also, the load at catastrophic failure is approximately 2,600 N that is 58-fold higher than the plateau load of a similar 11×11 sized unfilled honeycomb. This observation suggests that the confinement of PDMS filler within the individual cells and the cell's inability

to collapse (collapse is eliminated in this case; however, other softer filler materials may lead to cell collapse, also in filled specimens) are mechanisms responsible for the attainment of very high load levels in the filled specimen.

Let us compare the energy absorbed by the filled and unfilled honeycomb. The energy absorbed is calculated as the area under the $P - \Delta$ response. The energy absorbed by the unfilled honeycomb from the start of loading and prior to densification (corresponding to a macroscopic strain of about 0.9) is 1.43 J. In the filled specimen, noting that most of the stored energy is dissipated at once during catastrophic failure, the energy absorbed by the filled specimen from start of loading till catastrophic failure at Δ=11 mm (corresponding to a macroscopic strain of 0.3) is calculated as 15.2 J. Next, the energy absorbed for both types of specimens is normalized by mass. The normalized energy absorbed for the unfilled honeycomb is 427 J/kg, which is greater than 348 J/kg for the filled honeycomb; which makes the unfilled specimen a more efficient energy absorber per unit weight compared to its filled counterpart for this combination of wall material and filler. However, in the unfilled specimen, the energy is absorbed over a smaller crush distance compared to the unfilled specimen, where the absorbed energy is spread over majority of its length. Hence, the filled specimen is useful in applications where large amounts of energy need to be dissipated over shorter crush distances.

4.4 Digital image correlation study

4.4.1 Introduction

To understand the mechanisms of deformation in the pre-failure and the failure regime in the filled honeycomb, it is necessary to have knowledge of the strain distribution across the $x - y$ plane of the deforming specimen. Digital image correlation (DIC) technique is used to study the strain and displacement fields in the specimen.

DIC, a non-contact optical correlation method was developed by researchers from the University of South Carolina in the early 80s (Peters & Ranson (1982), Sutton et al. (1983)). It is a popular technique to obtain deformation measurements on both flat (using two-dimensional DIC) and curved (using three-dimensional DIC) surfaces of deforming solids. A review of the latest advances in DIC technique for aerospace materials is given by Daly (2010).

Two-dimensional DIC measurements on the filled samples are analyzed using commercially available DIC software called ARAMIS. First, the front face $(x, y, z = 0)$ of a filled honeycomb specimen is coated with a thin layer of white paint. Next, a uniform black speckle pattern is created on the white colored back-ground. The speckles serve as markers to track relative displacements on the flat surface of the specimen undergoing deformation. The displacement and deformation information is used by the software to generate strain maps. Note that the strain maps obtained from such an analysis is only a reflection of the strains that are present at the planar surface of the specimen. The nonlinear and large deformation response of the elastomeric filler suggests that the stress distribution at inner sections, which are confined, are expected to be higher than those at the free boundaries located at $(x, y, z = 0)$ and $(x, y, z = L)$.

Images are taken at the rate of 1 frame per second. Test data (load and crush distance information) are acquired at the rate of 10 Hz. Owing to the large amount of inplane deformation, there exists decorrelation that deters a unified DIC analysis of the entire deformation sequence, that is, from the initial undeformed reference state all the way up to the first failure event. Therefore, the DIC analysis is conducted in two stages, *Stage I* and *Stage II* that are described below.

4.4.2 Stage I: Initial up to pre-failure regime

The reference configuration for this stage is the undeformed specimen. The end-shortening value at the end of this stage is 2 mm (macroscopic strain value of 0.05). As seen earlier, the load response of the honeycomb is nonlinear. The deformation field Δ_x along the x-direction is shown in Figure 4.8. Here, in regions located near the center (along the y-direction), the Δ_x value is close to zero. However, for regions from the center of the specimen to the outer edges, this value gets larger. The contours of Δ_x bow inward due to frictional constraints along the x-direction at the top and bottom edges and free surface at the left and right sides.

The normal strain field (ϵ_x) along the x-direction is shown in Figure 4.9a. Within a cell, the strain field is non-uniform, with strain concentration being dominant near the center of the cell. The strains in the center of the cells are tensile, whereas those at the cell-cell contact site are compressive. This pattern is more or less uniform across the face of the specimen in all of the cells. The strain values near the center of the specimen are relatively higher than those at the edges due to higher degree of lateral constraint within the center of the cells. The normal strain (ϵ_y) field along the y-direction (the loading direction) is provided in Figure 4.9b. The strain map shows strain concentration near the center of the cells; and once again, this pattern is more or less similar across the specimen. However, the strains are purely compressive. In summary, the observations from ϵ_x and ϵ_y strain maps point to a biaxial state of compression provided by the cell to the filler material, that is, the filler is undergoing constrained deformation and hence, is a chief mechanism controlling the synergistic load response in the filled specimen.

Next, the shear strain (ϵ_{xy}) map is examined in the pre-failure regime shown in Figure 4.10a. The shear strain field is not pronounced during the initial stages of compression, but increases with an increase in crushing. Unlike strain concentrations seen in ϵ_x and ϵ_y strain maps, diagonal bands develop at 60° with the horizontal and

passing through the points where two cells are in contact. This band formation is a consequence of the circular cells changing to doubly-symmetric geometry in the pre-failure regime. One can also observe some pockets of high shear strains at the corners of the strain map which is an edge effect owing to rotations of corner cells at the loading/reaction platens.

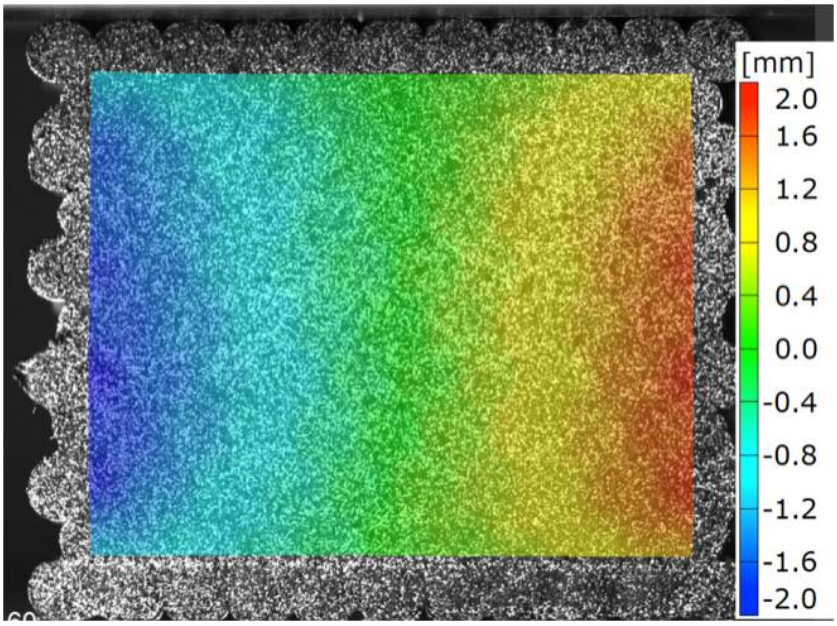

Figure 4.8: Displacement field along the x-direction.

4.4.3 Stage II: In the vicinity of first failure

Next, the DIC analysis is carried out in the vicinity of first failure. The reference state for shear strain (ϵ_{xy}) map calculation is 8 frames before failure. Note that the specimen is loaded through a crush distance of 0.033 mm between two frames. The shear strain field at the onset of failure is shown in Figure 4.10b. The sense of rotation is also shown in Figure 4.10b. Adjacent rows located to the left and right sides of the failure site have more or less similar magnitude of shear strains. The cells in these two rows tend to move sideways towards the specimen's free edge, thereby relieving the

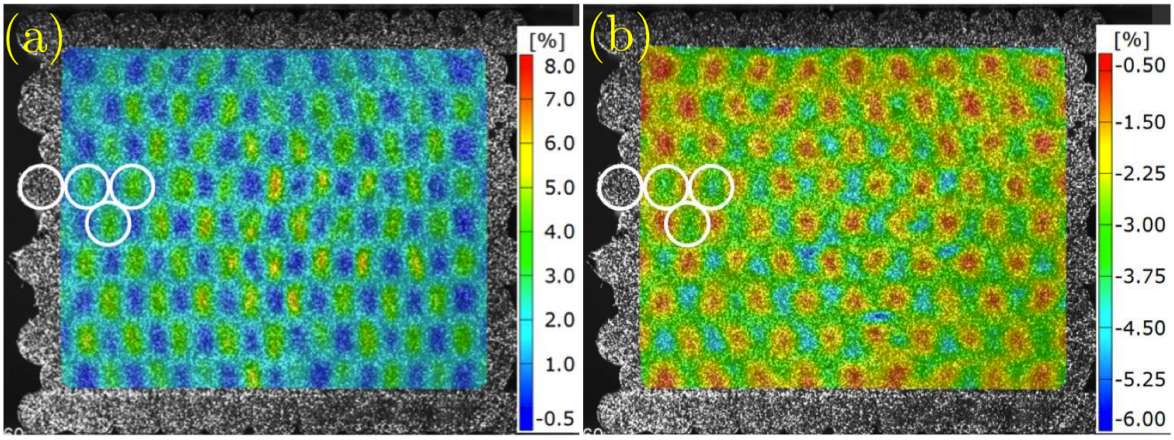

Figure 4.9: (a) Normal strain (ϵ_{xx}) field along the x-direction. (b) Normal strain (ϵ_{yy}) field along the y-direction.

compressive stresses in the sample. The localization also alters the shear strain field across the entire specimen as well. At the first failure site, decorrelation is noticed due to large displacements and rotations. Hence, subsequent localized failure events are not analyzed owing to cracking of the paint surface.

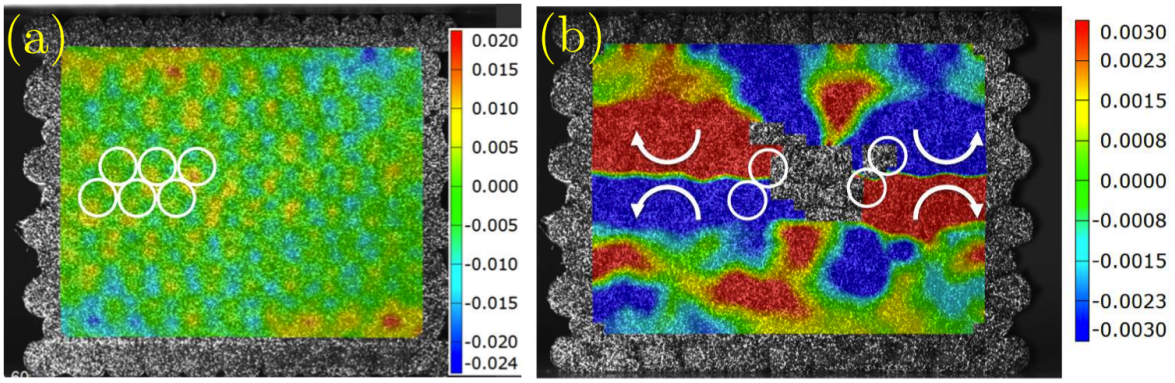

Figure 4.10: (a) Shear strain (ϵ_{xy}) field showing diagonal band formation in the pre failure regime. (b) Shear strain field at first failure. The arrows show sense of rotation of two adjacent rows near the failure site.

4.5 Material Properties

The dimensions of the honeycomb cell were measured using an optical study. The nominal dimensions measured are: cell radius (R) 2 mm, wall thickness (t) 0.080 mm, double-wall thickness (t_d) 0.135 mm, wall-to-wall bond length (L_d) 0.25 mm and out-of-plane length (L) 25.4 mm. Here, the double-wall thickness t_d is the effective thickness of the wall at the contact site of two cells, the contact site having bond length L_d along the cell circumference (Figure 2.1). Thin strips of the wall material were cut along the longitudinal direction and tested under uniaxial tension to obtain the stress vs. strain behavior. The results from these tests are shown Figure 4.11 for three samples. The response displays a linearly elastic part up to a stress value of 20 MPa, followed by a non-linear region which ends at a value of approximately 57 N, finally followed by a strong ductile response up to a nominal strain value of 0.9. Uniaxial tension tests of the wall material were also performed, along the circumferential direction. Several strips were cut along the circumferential direction of the cell wall and were tested. The stress-strain plot corresponding to these tests is shown in Figure 4.12. Here, the behavior is brittle unlike that along the axial direction. Beyond the plastic region, mode-I cracking is noticed accompanied by an instantaneous drop in load. The failure point was either at the grips or away from the grips. Of these, the data obtained from failure away from the grips only is reliable for quantifying the critical strength. Such cases are represented by dashed lines in Figure 4.12. The maximum stress value (σ_{cr}) required for the specimens to tear is 51 $\pm$ 3.9 MPa. Although the wall material property is anisotropic with respect to stiffness as well as post peak behavior as seen in the tensile tests on thin strips, the whole honeycomb cells are modeled as isotropic the for sake of simplicity. That is, the elastic modulus is taken to be that along the longitudinal direction, where the stiffness values were more or less consistent (see Figure 4.11) unlike that along the circumferential direction (see Figure 4.12), where the initial stiffness values

exhibit a wide scatter. This scatter is due to the the uniaxial testing on strips along the circumferential direction that are curved due to residual stresses induced during manufacturing. A more accurate but difficult method to overcome this issue would be subjecting the honeycomb cell to internal pressure testing to back out the critical hoop stress to failure.

The filler material used in this study, PDMS elastomer is available from Dow Corning as Sylgard 184. A sample of PDMS is cast in a cylindrical mold of length 25.4 mm and diameter 22.8 mm. The prepared PDMS specimen is subjected to a uniaxial compression test at crush rate of 0.033 mm/sec using an INSTRON machine. The top and bottom loading surfaces are lubricated to reduce frictional effects on the compression response. This test enables a characterization of the polymer through an appropriate hyperelastic model, that is subsequently used in finite element simulations described later. The sequence of images showing PDMS deformation along with the load vs. displacement plot is shown in Figure 4.13.

4.6 Finite element simulation of the experiment

4.6.1 Model Description

The inplane crush of filled honeycomb is simulated using the commercially available finite element (FE) software ABAQUS® (Simulia (2011)). The finite element model is created using the measured dimensions of the honeycomb microsection. The honeycomb cells are modeled using four-node linear S4R shell elements. The circumference of the cell is discretized with 30 elements and the axial direction is discretized with 6 elements. The nonlinear behavior of the filled honeycomb that is observed from the experiments requires that the entire specimen be modeled in this numerical study. The filler is modeled using a mixture of eight node C3D8R and six node C3D6R solid elements. Since the specimens are compressed via steel plates (at the

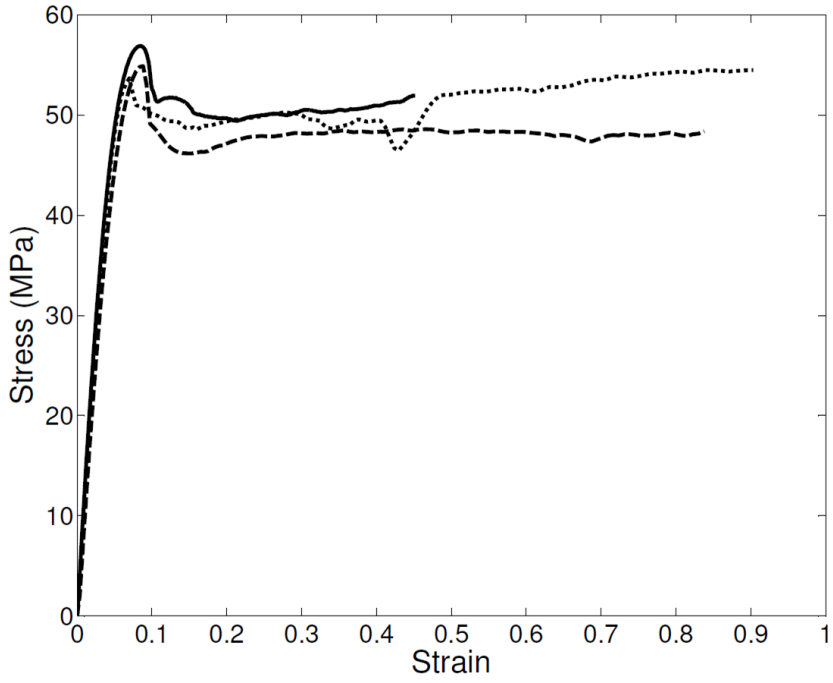

Figure 4.11: Nominal stress vs. strain tensile response of the honeycomb wall (longitudinal direction).

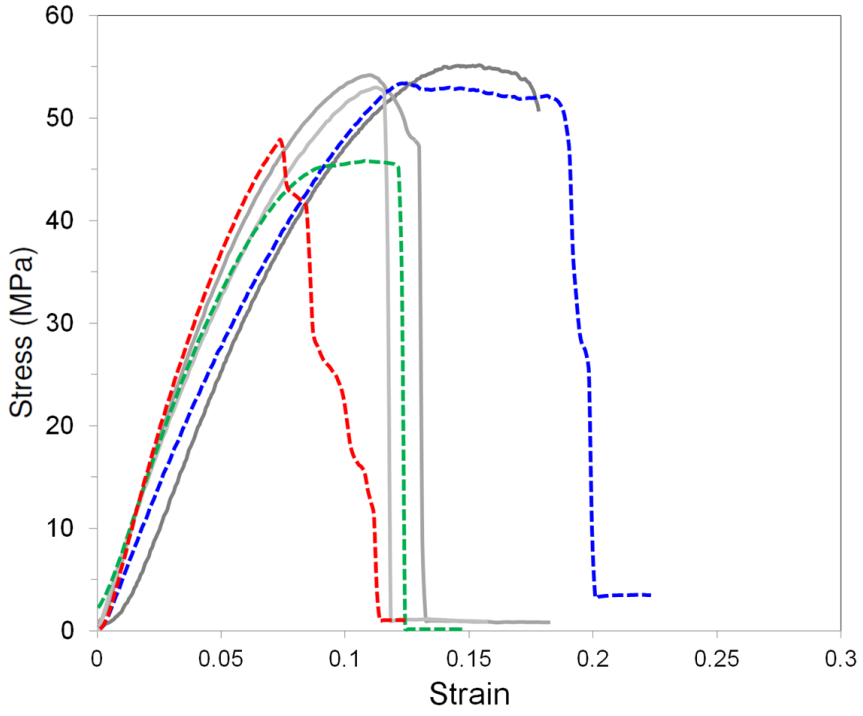

Figure 4.12: Nominal stress vs. strain tensile response of the honeycomb wall (circumferential direction). Curves with dashed lines signal trials where tearing occurred near the center of the strip.

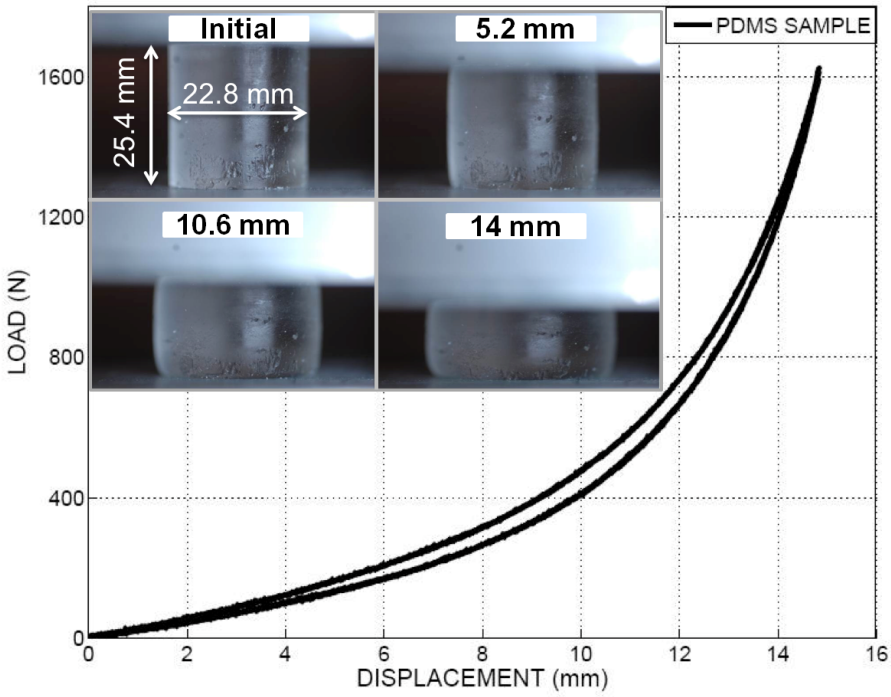

Figure 4.13: Load vs. displacement response for PDMS cylindrical block along with images during compression.

top and at the bottom), the plates are modeled in the FE simulation via solid C3D8R elements with standard properties of steel. The triangular regions between any three cells are modeled with C3D8R elements. The FE model is shown in Figure 4.14.

The polycarbonate material is modeled as an elastic-plastic solid that obeys finite deformation J_2 incremental theory of plasticity with a von Mises yield condition and isotropic hardening (Lubliner (2008)). For this purpose, the measured experimental stress-strain response in uniaxial tension is provided in Figure 4.11. For the PDMS elastomer, the uniaxial compression test data (nominal stress-strain response) from the experiment are used as input using the Marlow Hyperelastic model, available as an option in ABAQUS (Simulia (2011)). The Marlow model is based on the first strain invariant and is preferred when limited test data are available. In the present study, the uniaxial compression data are used in characterizing the PDMS elastomer.

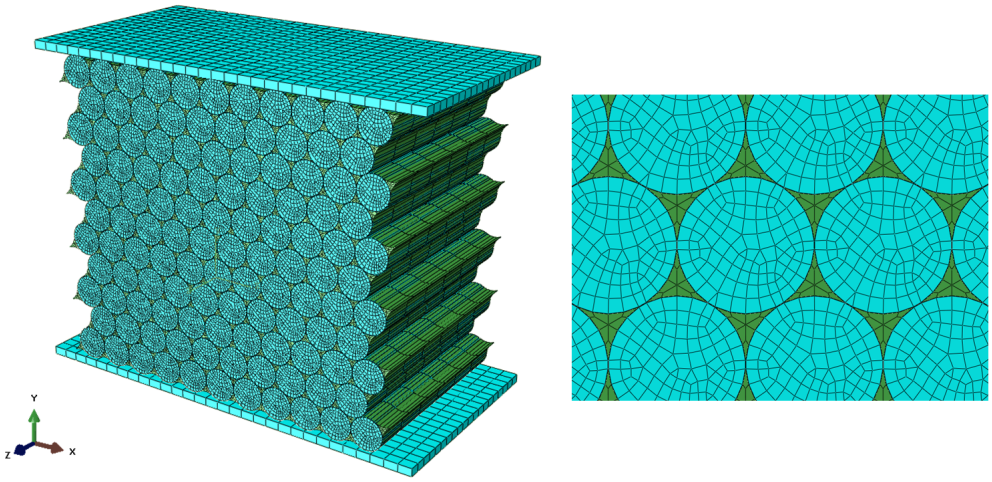

Figure 4.14: Finite element model of the filled honeycomb specimen is shown along with the top loading plate and bottom plate (left). The portion of the front view (right).

As mentioned earlier, the PDMS does not adhere to the cell walls in the filled specimens. Therefore, the contact between the outer curved surface of the PDMS filler material and the inner surface of the honeycomb walls is assumed to be resisted only by friction. Hence, the general contact algorithm with "hard" contact is used to avoid penetration of surfaces during normal contact, and (b) tangential frictional contact with coefficient of friction $\mu = 0.3$. Similarly, since in the experiment, the bottom and top faces of the honeycomb are not restrained along the x-direction, the contact between the honeycomb and top/bottom loading plates are also modeled using (a) "`HARD`" normal contact and (b) tangential contact with an assumed coefficient of friction, $\mu = 0.3$. The coefficient of friction $\mu = 0.3$ assigned to each of the polycarbonate-PDMS and polycarbonate-steel interfaces is only an assumption and was not measured experimentally.

The crush simulation is conducted using ABAQUS/Explicit. A crush velocity of 10 mm/s is applied to the top plate. The bottom plate is constrained in rotation and translation and the top and bottom nodes, near the plates, are constrained in the x-direction. Dynamic explicit solver is chosen to simulate the static experimental

problem because of computational efficiency, and because the problem under consideration involves numerous surface-to-surface contact definitions between the PDMS elastomer and honeycomb wall surfaces.

4.6.2 Smeared Crack Approach

SCA is a continuum approach of modeling fracture in a solid. The SCA was first formulated by Bažant & Oh (1983) as the crack band model and later modified by Rots et al. (1985). The SCA code used for this study follows from the recent work of Heinrich & Waas (2012), who studied the progressive damage and fracture in laminated composites and extended the Rots model to include non-isotropic fracture. Typically, the response of a fracturing solid can be divided into two regimes: (1) the pre-fracturing regime where the tangent stiffness of the stress-strain response is positive which can be described by classical continuum theories, and (2) post-fracturing regime where the tangent-stiffness becomes negative (this is also known as *softening*) is governed by traction-separation laws. In many models where the crack is treated as a strong discontinuity requires the knowledge of the crack path *a priori* - examples include VCCT (Xie & Biggers (2006)), CZM (de Borst (2003)) and DCZM (Xie & Waas (2006)). However, the SCA is advantageous compared to these models in that the crack path need not be known *a priori*.

During the post-fracture regime where softening occurs at the material level, the tangent stiffness becomes negative. Under this condition wave speeds in the material become imaginary and the material cannot be objectively described by the usual stress-strain relationship because the problem becomes ill-posed (Bažant & Cedolin (1991)). If such a problem is implemented in a finite element framework, failure will localize into an element irrespective of its size. Thus, the energy dissipated during fracturing will depend on element size. In the extreme case with the element size being vanishingly close to zero, there would be zero dissipation. Hence, such an

outcome is not mesh objective. *Mesh objectivity* is ensured in the post failure region via traction-separation laws that include a *characteristic length scale*, such that the total energy dissipated is equal to the fracture toughness and is independent of the element size. Next, the essentials of the SCA are presented, as applied to the current problem.

In this method, the local strains ($\boldsymbol{\epsilon}$) are resolved into continuum strains ($\boldsymbol{\epsilon}_{co}$) and crack strains ($\boldsymbol{\epsilon}_{cr}$) in the global coordinate system as

$$\boldsymbol{\epsilon} = \boldsymbol{\epsilon}_{co} + \boldsymbol{\epsilon}_{cr} \tag{4.1}$$

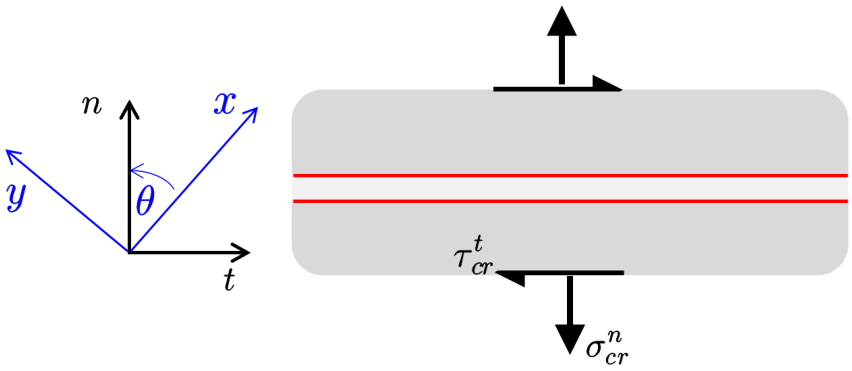

Figure 4.15: Illustration of a crack (red) with local (t, n) and global (x, y) coordinate systems. Also shown are the normal and tangential crack stresses.

In general, the continuum strains that are governed by the usual constitutive laws can be further resolved into elastic and plastic parts as $\boldsymbol{\epsilon}_{co} = \boldsymbol{\epsilon}_{el} + \boldsymbol{\epsilon}_{pl}$. On the contrary, the crack strains ($\boldsymbol{\epsilon}_{cr}$) that become operative once fracture initiates are governed by traction-separation laws. Consider the crack configuration shown in Figure 4.15. The crack strains in the local coordinate system ($\mathbf{e}_{cr}$) can be transformed to the global crack strain ($\boldsymbol{\epsilon}_{cr}$) as

$$\boldsymbol{\epsilon}_{cr} = [\mathbf{N}]\mathbf{e}_{cr} = [\mathbf{N}] \begin{pmatrix} \epsilon_{cr}^{n} \\ \gamma_{cr}^{t} \end{pmatrix} \tag{4.2}$$

where ϵ_{cr}^n is the strain component normal to the crack and γ_{cr}^t is that tangential to the crack surface. Likewise, the global stresses ($\boldsymbol{\sigma}$) are related to the local tractions ($\mathbf{s}_{cr}$) at the crack interface as

$$\boldsymbol{\sigma} = [\mathbf{N}]\mathbf{e}_{cr} = [\mathbf{N}] \begin{pmatrix} \sigma_{cr}^n \\ \tau_{cr}^t \end{pmatrix} \tag{4.3}$$

Here, in the calculation of transformation matrix [**N**], it is assumed that cracks propagate perpendicular to the principal stress directions. At the crack interface, the tractions $\mathbf{s}_{cr}$ and crack separations ($h\mathbf{e}_{cr}$) are related through the secant stiffness matrix [$\mathbf{D}_{cr}$] and a damping matrix [$\mathbf{D}_{da}$] as

$$\mathbf{s}_{cr} = [\mathbf{D}_{cr}]h\mathbf{e}_{cr} + [\mathbf{D}_{da}]h\dot{\mathbf{e}}_{cr} \tag{4.4}$$

where h is the characteristic length scale. The secant stiffness matrix is a diagonal matrix written as

$$[\mathbf{D}_{cr}] = \begin{pmatrix} E_{cr}(\epsilon_{cr}^n) & 0 \\ 0 & G_{cr}(\epsilon_{cr}^n) \end{pmatrix} \tag{4.5}$$

Here, it is assumed that there is no extensional-shear coupling across the crack interface. The damping matrix is written as

$$[\mathbf{D}_{da}] = \begin{pmatrix} \eta & 0 \\ 0 & \eta \end{pmatrix} \tag{4.6}$$

where η is the damping parameter. The damping matrix introduces time dependence on the crack progression and also stabilizes the numerical solution scheme. The crack strain rate can be approximated using finite differences as

$$\dot{\mathbf{e}}_{cr} \approx \frac{\mathbf{e}_{cr} - \mathbf{e}_{cr}^{old}}{\Delta t} \tag{4.7}$$

The constitutive relation for the continuum is

$$\boldsymbol{\sigma} = [\mathbf{D}_{co}]\boldsymbol{\epsilon}_{el} \tag{4.8}$$

where $[\mathbf{D}_{co}]$ is the secent stiffness of the continuum. The above equations when combined gives a relates crack strain hand total elastic strain as

$$\mathbf{e}_{cr} = \left[\mathbf{D}_{cr}(\mathbf{e}_{cr}) + \mathbf{N}^T\mathbf{D}_{co}\mathbf{N} + \frac{\mathbf{D}_{da}}{\Delta t}\right]^{-1}\left[\mathbf{N}^T\mathbf{D}_{co}\boldsymbol{\epsilon} + \frac{\mathbf{D}_{da}\mathbf{e}_{cr}^{old}}{\Delta t}\right] \tag{4.9}$$

Note that the traction-separation law can be written explicitly in terms of the fracture toughness and the crack strains using an appropriate function. A common choice could be either linear or exponential softening. Assuming exponential softening in the form $\sigma(\epsilon_{cr}^n) = \sigma_{cr}\exp(-k_{cr}\epsilon_{cr}^n)$, the fracture energy can be equated to the integral of the traction over the separation to find the unknown constant k_{cr}.

$$G_{IC} = \int_0^\infty \sigma(\epsilon_{cr}^n)hd\epsilon_{cr}^n = \int_0^\infty \sigma_{cr}\exp(k_{cr}\epsilon_{cr}^n)hd\epsilon_{cr}^n \tag{4.10}$$

which gives

$$k_{cr} = \frac{h\sigma_{cr}}{G_{IC}} \tag{4.11}$$

An expression for the secant stiffness is written as $E_{cr}(\epsilon_{cr}^n) = \sigma(\epsilon_{cr}^n)/\epsilon_{cr}^n$ which is

$$E_{cr} = \frac{\sigma_{cr}}{\epsilon_{cr}^n}\exp\left(\frac{-h\sigma_{cr}\epsilon_{cr}^n}{G_{IC}}\right) \tag{4.12}$$

Next, the relation between global stresses and total global strains in the softening

regime is

$$\boldsymbol{\sigma} = \left[\mathbf{D}_{co} - \mathbf{D}_{co}\mathbf{N}\left(\mathbf{D}_{cr} + \mathbf{N}^T\mathbf{D}_{co}\mathbf{N} + \frac{\mathbf{D}_{da}}{\Delta t}\right)^{-1}\mathbf{N}^T\mathbf{D}_{co}\right]\boldsymbol{\epsilon} - \left[\mathbf{D}_{cr}(\mathbf{e}_{cr}) + \mathbf{N}^T\mathbf{D}_{co}\mathbf{N} + \frac{\mathbf{D}_{da}}{\Delta t}\right]\left(\frac{\mathbf{D}_{da}\mathbf{e}_{cr}^{old}}{\Delta t}\right) \quad (4.13)$$

In the computation of the crack strains, the traction-separation law has to be satisfied rigorously. The crack strains in Equation 4.9 are solved iteratively using Newton's method because the above equation is implicit in $\mathbf{e}_{cr}$. Once $\mathbf{e}_{cr}$ are obtained from this iterative procedure, the crack stresses now can be computed in Equation 4.13 at the end of an increment.

The SCA procedure described above is implemented in the finite element model to simulate fracturing in the cell walls via user sub-routine VUMAT. First, the code is specialized for isotropic material behavior under plane stress conditions. Secondly, elastic-plastic response (using J_2 deformation theory) prior to softening is incorporated as shown in Figure 4.16. These modifications take into account the elastic-plastic response of the polycarbonate material; and due to the nature of a planar state of stress in the cell walls that are modeled as S4R shell elements in the simulations to follow. *Deformation theory of plasticity* which is also known as *total strain theory* was developed by Hencky (1924) and Nadai (1931) relates stresses to total strains. This theory is mathematically more easier than the more general *incremental* or *flow theory of plasticity*. Here, the nonlinear plastic deformation is modeled with stress-strain relations where the total strains depend only on total stress via the *secant modulus*, and does not depend on the loading path to reach this final state of stress. The stress-strain response is represented as

$$\sigma(\epsilon) = \begin{cases} E\epsilon & \text{for } \sigma \leq \sigma_y \\ \sigma_y - \frac{k_1}{k_2}\left\{\exp\left(-\frac{k_2}{\epsilon}\right) - \exp\left(-\frac{k_2\sigma_y}{E}\right)\right\} & \text{for } \sigma > \sigma_y \end{cases} \quad (4.14)$$

where the hardening parameters k_1 and k_2 are obtained using a curve fitting procedure with the experimental data for the measured uniaxial stress-strain response for $\sigma > \sigma_y$. Hence, specializing this to the SCA requires that the crack strains be resolved only as $\boldsymbol{\epsilon} = \boldsymbol{\epsilon}_{co} + \boldsymbol{\epsilon}_{cr}$ where $\boldsymbol{\epsilon}_{co}$ includes the plastic strains as well because deformation theory is chosen.

The important parameters in the SCA are: σ_{cr}, the critical stress to initiate tearing; and G_{IC}, the mode I fracture toughness, incorporated through an exponential softening response. Here, σ_{cr} controls the first failure point whereas G_{IC} influences the behavior after the onset of failure.

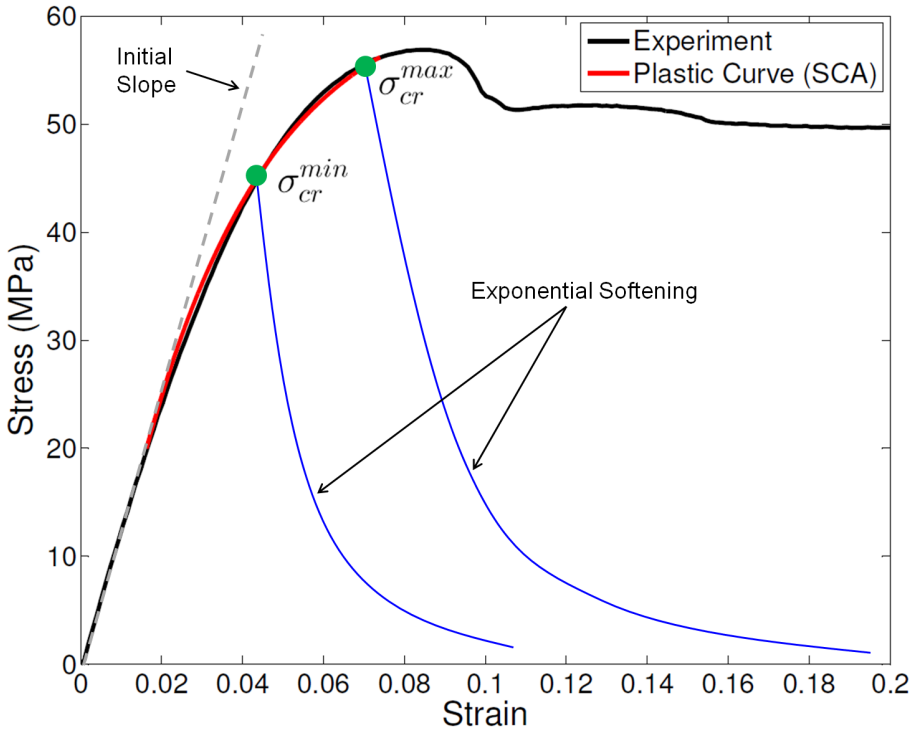

Figure 4.16: Stress-strain response of polycarbonate shown against exponential fit for the plastic part to be used in SCA model. Also shown are the critical stress values $\sigma_{cr}^{min} = 46$ MPa and $\sigma_{cr}^{max} = 55$ MPa, and exponential softening response that is a function of Mode I fracture toughness G_{IC}.

4.6.3 Simulation Results

Recall that in the experiment, the onset of localization is observed near the center of the specimen. Hence, two types of simulations are performed with: (1) *Model A*, with smeared crack band being applicable over 11 cells around the center (2) *Model B*, with smeared crack band being applicable over 28 cells around the center. A schematic showing the crack bands in the honeycomb in Model A and Model B is shown in Figure 4.17. For the cells with no crack band, the continuum elastic-plastic model of polycarbonate was in effect.

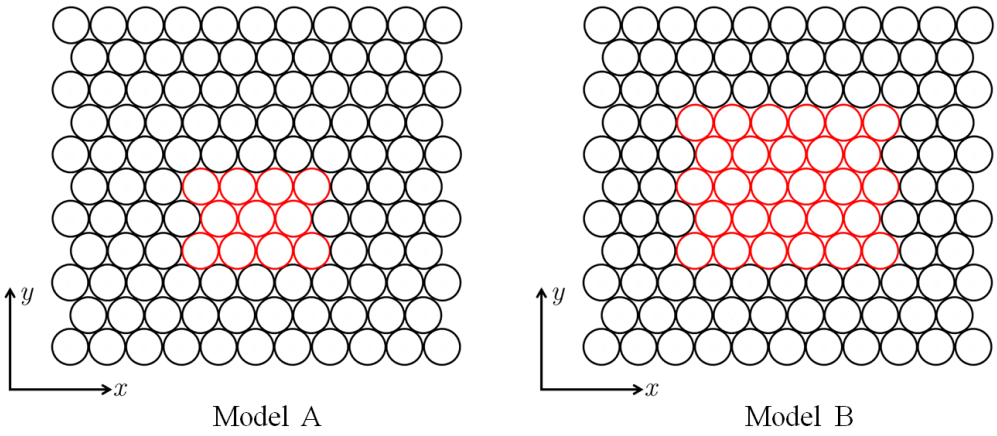

Figure 4.17: Schematic showing 11×11 honeycomb model with SCA (shown in red) being applied in Model A and Model B.

The load vs. displacement plot comparing the simulations and experiments is shown in Figure 4.18. For each set of Models A and B, the simulations were performed using $\sigma_{cr}^{min} = 46$ MPa and $\sigma_{cr}^{max} = 55$ MPa. The value of fracture toughness G_{IC} is taken as 2 N/mm. In the pre-failure region, the deformation response from both the models are in good agreement with the experimental response as seen in Figure 4.3.

In the pre-failure region, the circular cells change to a doubly-symmetric deformation mode and the response is non-linearly elastic. Strain concentration is seen around the center of the filled cells. To enable qualitative comparison with the DIC analysis, the normal strain distribution along the x and y directions is shown in Fig-

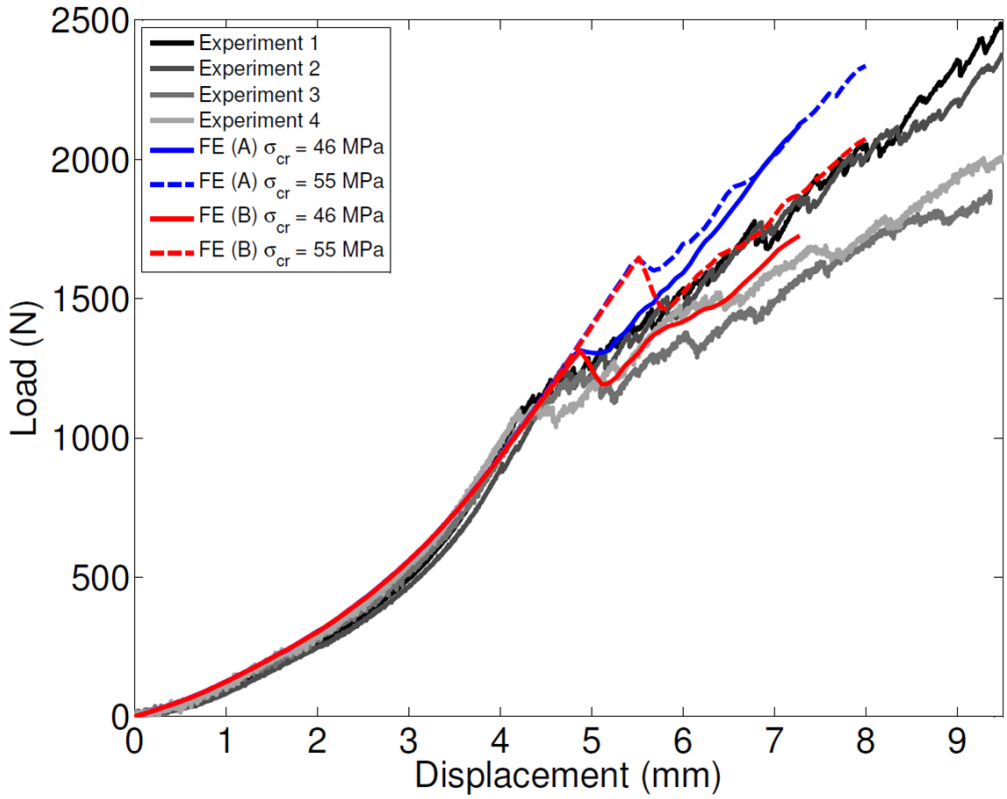

Figure 4.18: Load vs. displacement response of the simulations and of the experiments. Simulations for Model A is shown in blue, whereas that for Model B is shown in red.

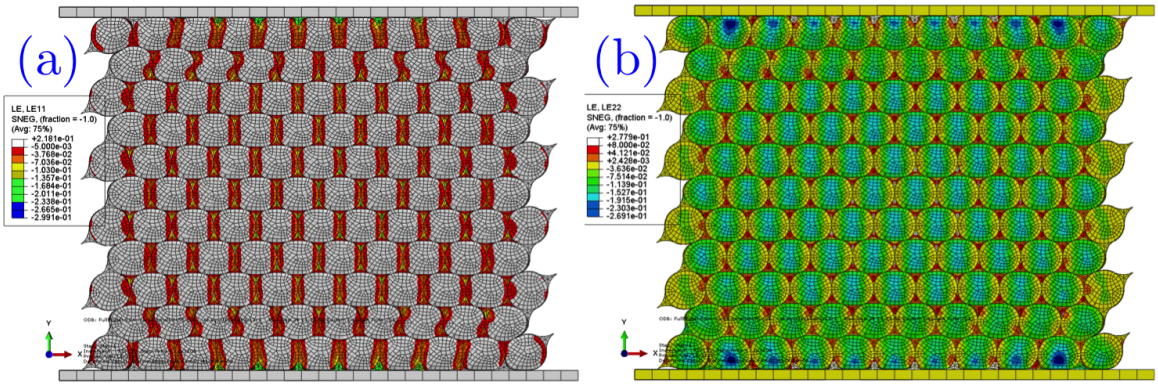

Figure 4.19: (a) Compressive normal strain (ϵ_{xx}) map along the direction perpendicular to the direction of loading. The nature of strains along the center of the cells in the filler is tensile. (b) Normal strain (ϵ_{yy}) map along the direction of loading.

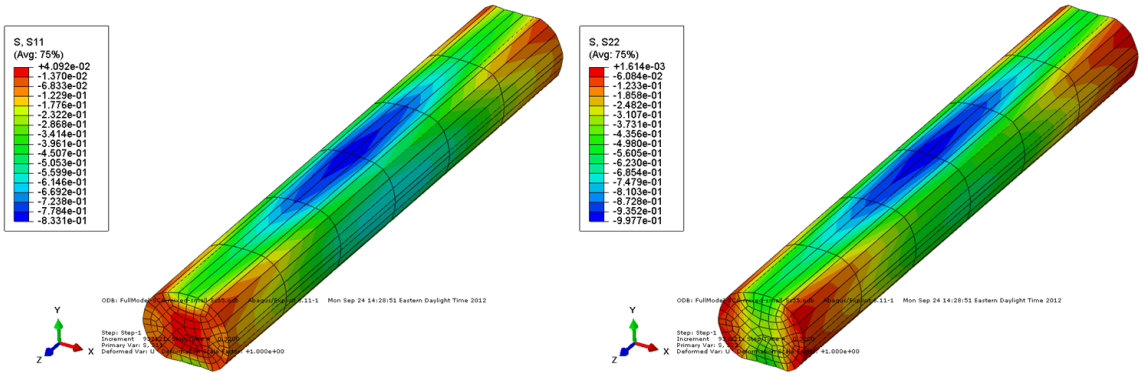

Figure 4.20: Normal stress distributions S_{11} (left) and S_{22} (right) along the x and y directions respectively, for the filler located at the center of the model. Units are in MPa.

ure 4.19. From these strain maps, observe the biaxial state of compression of the PDMS filler material in each of the cells. This behavior is consistent with the strain maps obtained from the DIC analysis that were reported in the previous section. The stress distribution along the x and y directions for the filler located near the center of the model is shown in Figure 4.20. The stresses vary along the length and are lowest at the free ends. The compressive stresses are dominant even along the direction perpendicular to the loading direction, i.e. along the x-direction. This "constrained deformation state" is responsible for the attainment of high load levels in the model.

In the pre-failure region, the cells around the center of the model experience higher stresses compared to those away from the center; hence the localization occurs near the center of the specimen due to wall cracking of the cells around this region. In the case of Model B, the localization phenomenon is shown in Figure 4.21. Observe the similarities with the onset of localization seen in the experiment (Figure 4.6). These features are similar for both models considered in this study. The maximum in-plane principal strain distribution in the cell walls is shown in Figure 4.22. This observation confirms that the *tearing of the cell walls* triggers localization in the specimen.

The simulations are able to capture many important features seen in the ex-

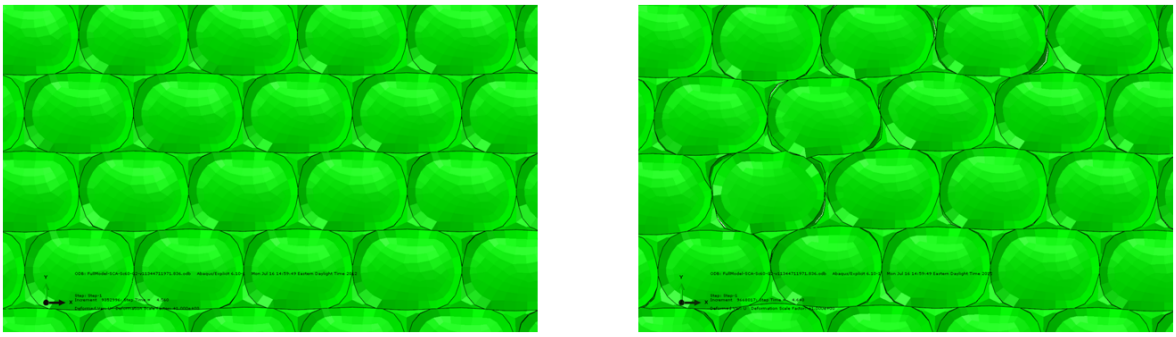

Figure 4.21: Images showing events (a) prior to localization (left), (b) onset of localization (right).

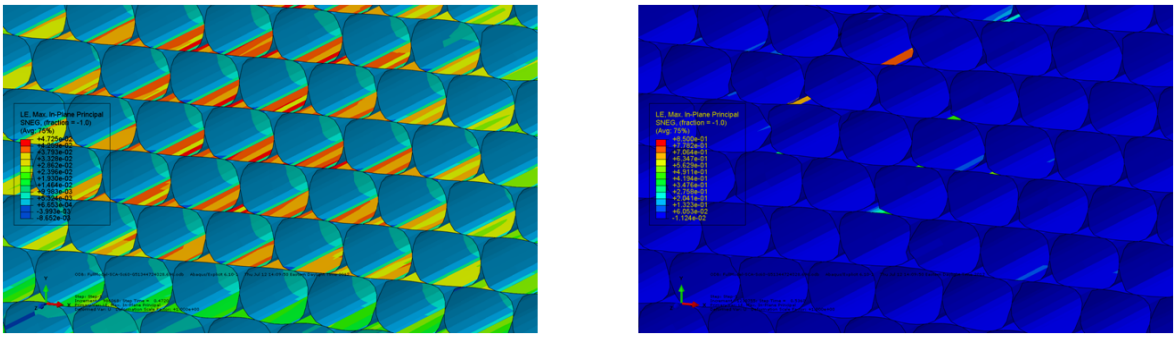

Figure 4.22: Images showing maximum in-plane principal strains in the honeycomb walls (a) prior to localization (left), (b) onset of localization (right).

periments, such as localization at first failure due to wall tearing and deformation response, especially up to the onset of failure. Therefore, the SCA approach is a promising tool that could be used to model wall cracking in the filled honeycombs. However, some differences do exist, especially with regard to the simulation response at the onset of localization, primarily due to the use of an explicit solver of the finite element equations. Recall that in the static experiment, there is no load drop during the onset of failure and the localization is restricted to smaller regions around the center of the specimen. Thereafter, the localized failure is seen to spread to other regions in the specimen with an increase in crushing. This progression of failure oc-

curs at an approximately constant value of stiffness. In contrast, in the simulations performed, the load momentarily drops at the onset of localization. The drop is more for Model B where damage is seen to spread to a much larger region compared to Model A. Moreover, the post failure stiffness in the experiment lies between that of Model A and Model B. Therefore, for Model B, the larger drop in load at first failure and subsequent reduction in stiffness is attributed to the somewhat artificial dynamic nature of the simulation. When tearing is initiated near the center of the model, the energy released due to the release of kinetic energy (note that, the kinetic energy is not suppressed totally in a mass-scaled explicit analysis that aims to simulate a static test) causes surrounding regions to be loaded in excess of the critical stress for tearing. These over-stressed regions initiate premature tears, triggering failure at many points away from the center. This numerical effect can be avoided by applying the crack band scheme selectively to a smaller sized region in the specimen, effectively compensating for the artificial overstress condition.

4.7 Conclusions

In this chapter, experimental and associated computational modeling results for the quasi-static in-plane crush response of a composite circular cell honeycomb filled with PDMS elastomer have been reported. Two important deformation regimes are distinguished in this study (a) the pre-failure regime (b) failure regime. In the pre-failure regime, the specimen exhibited nonlinear response that is controlled by the PDMS filler. Moreover, a synergistic deformation response effect, leading to a larger than expected energy absorption effect is observed, which was explained by appealing to digital image correlation (DIC) analysis of the deformation response and associated finite element based modeling results. The synergistic effect arises out of highly constrained biaxial state of stress in the PDMS filler material. Unlike traditional honeycombs where buckling of the cells is a primary mechanism of energy dissipa-

tion, the mechanism of energy dissipation in the filled honeycombs is due to mode I fracture of the cell walls triggering other localized deformation responses. Fracture triggered localization response in the post-failure regime was confirmed through the finite element (FE) modeling of the experiment. A modified Smeared Crack Approach (SCA) was chosen to simulate cracking in the cell walls. SCA is advantageous in that the crack path need not be prescribed at the start of the FE simulation, instead it is an outcome of the resulting simulations. The deformation response between the experiment and modeling predictions were found to be in good agreement, thus lending credence to the modeling results that can be used to design filled honeycomb structures for tuned-in energy absorption.

From our understanding of the mechanics of filled honeycomb crushing, three important parameters are identified that are useful from design point of view. For a honeycomb having cells of radius R and wall thickness t, the first design parameter is the *relative stiffness* of the filler material and that of the honeycomb, which controls the stiffness of the filled specimen in the pre-failure regime. Also, the extent of the nonlinearity in the pre-failure regime depends on the hardening response of the filler material. The second design parameter is the *mode I fracture strength* (σ_{cr}) that controls the first failure event in the filled response, that is, this parameter governs how early first localization event occurs upon loading. The third design parameter is the *mode I fracture toughness* (G_{IC}) that controls how fast localization spreads in the failure regime, beyond the first failure event. Based on these guidelines, optimal geometry and materials can be chosen to design filled honeycombs for a particular application.

CHAPTER V

Static Compression Response of Filled Honeycombs: Out-of-Plane direction

5.1 Introduction

[1] Several studies have addressed the problem of static axial crush of honeycombs. In particular, Mellquist & Waas (2004) have studied the static, crush response of circular cell polycarbonate honeycombs in the out-of-plane (axial) direction. They reported that after the initial collapse (corresponding to the *peak load*), folding initiates in the structure accompanied by drop in the load. This sudden load drop is termed as *unstable collapse*. Thereafter, the cell continues to carry load at a fairly constant state of load which is referred to as the *plateau load*. They concluded that the localized concertina-diamond fold formation was the dominant mode of failure in these structures. They also reported that scaling, in terms of the number of cells per specimen, has no influence on the plateau load. The out-of-plane static crush response of hexagonal cell aluminum honeycombs have been examined through experiments and explicit finite element simulations by Wilbert et al. (2011). In these honeycombs, the cell walls are flat plates, and the plates are joined along some of the

[1]Parts of this chapter are published in D'Mello, R. J. & Waas, A. M., "Synergistic energy absorption in the axial crush response of filled circular cell honeycombs," *Composite Structures*, 94(5), pp. 1669-1676, 2012.

walls, to neighboring cells, a result of efficient manufacturing as described in Gibson & Ashby (1999).

In this chapter, the out-of-plane axial crush response of filled polycarbonate honeycombs are studied, motivated by our earlier work D'Mello et al. (2012) on high rate axial crush response of unfilled circular honeycombs. The objective of this study is to investigate the influence of the filler on the load response and mode of failure. In particular, a synergistic energy absorption phenomenon is shown, leading to an amplification of energy absorption, as a direct result of the filler material influencing the mode of cell deformation, compared to the corresponding, unfilled honeycomb deformation mode. 3-cell, 7-cell and 19-cell polycarbonate honeycomb microstructures, both, unfilled and filled, are used in the experimental studies. Polyurethane, a soft elastomer is used as the cell filler material. A representative diagram of the 3-cell honeycomb with contact sites is shown in Figure 5.1.

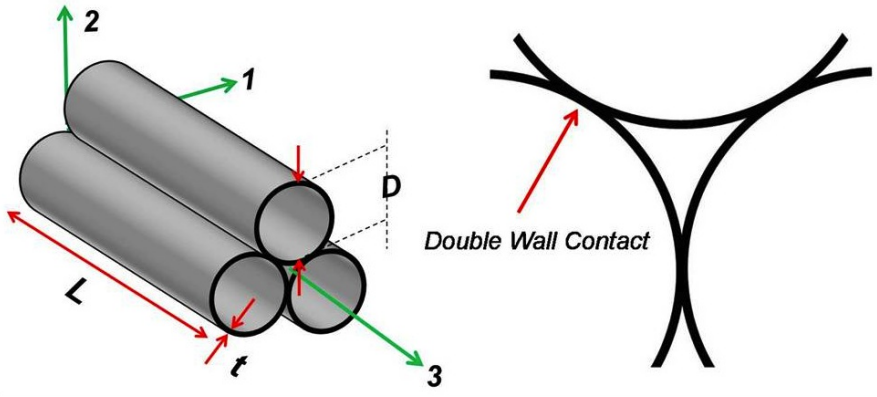

Figure 5.1: Schematic of a 3-cell specimen showing the cell length (L), wall thickness (t) and cell diameter (D) is shown to the left. The out-of-plane loading direction is in the 3-direction. The double wall contact over a line is shown in a diagram to the right.

5.2 Sample preparation & test setup

The honeycomb's physical dimensions were measured using a low-magnification optical microscope study. The out-of-plane length was 24.5 mm, the cell wall thickness was 0.065 ± 0.005 mm and the cell radius was 2.108 ± 0.39 mm. Each cell is in contact with its neighbor through an area contact. The double wall thickness and the cell adhesion length measured 0.133 ± 0.006 mm and 0.227 ± 0.027 mm respectively. The material properties of the polycarbonate material were assumed to be isotropic. A single cell was crushed in a uniaxial testing machine and the load response was backed out by simulating this experiment in ABAQUS/Standard and matching the slope of the load-deflection plot. The average Young's modulus of the specimen was found to be approximately 2,400 MPa. Polyurethane solution is first prepared and poured into a cylindrical mold (diameter 22.8 mm and length 25.4 mm) containing the honeycomb. The polyurethane-honeycomb sample is cured at room temperature for 5 days. A schematic in Figure 5.2 shows the cross-section of the filled 3-cell, 7-cell and 19-cell specimens.

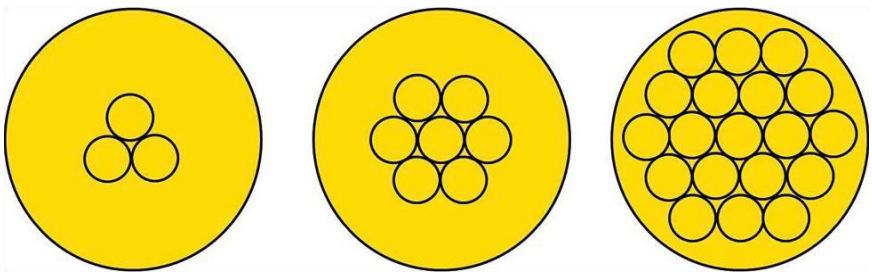

Figure 5.2: Cross section of the 3-cell, 7-cell and 19-cell specimens filled with polyurethane.

5.3 Experiments: Polyurethane as the Filler Material

5.3.1 Static Uniaxial Compression of Polyurethane

The polyurethane block having the same dimensions as the mould is tested under similar loading conditions as mentioned above. Lubricating oil is applied at the loading surfaces to reduce the influence of friction on the test specimen. A set of images taken from the experiment are provided in Figure 5.3. For the macroscopic strain (end crushing over initial length) of 0.25 onwards, prominent barreling is observed. The specimen is compressed up to 90% of its length. Upon unloading, the specimen relaxes nearly to its original length. The load increases at a lower rate up to macroscopic strain of 0.5 and thereafter rises rapidly with increased crushing. The uniaxial loading-unloading plot is shown in Figure 5.4 shows some hysteresis in the specimen. This information from this experiment is crucial for characterizing the hyperelastic properties of polyurethane for use in the finite element crush simulation. Moreover, this test also will also serve to compare the filler material's contribution when filled honeycomb specimens are subject to uniaxial static compression loading.

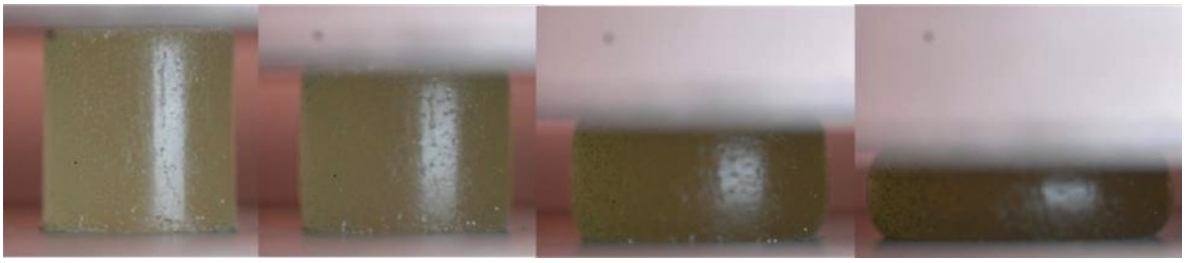

Figure 5.3: Image sequence taken from the quasi-static uniaxial compression test of polyurethane block corresponding to macroscopic strains of 0, 0.22, 0.48 and 0.70.

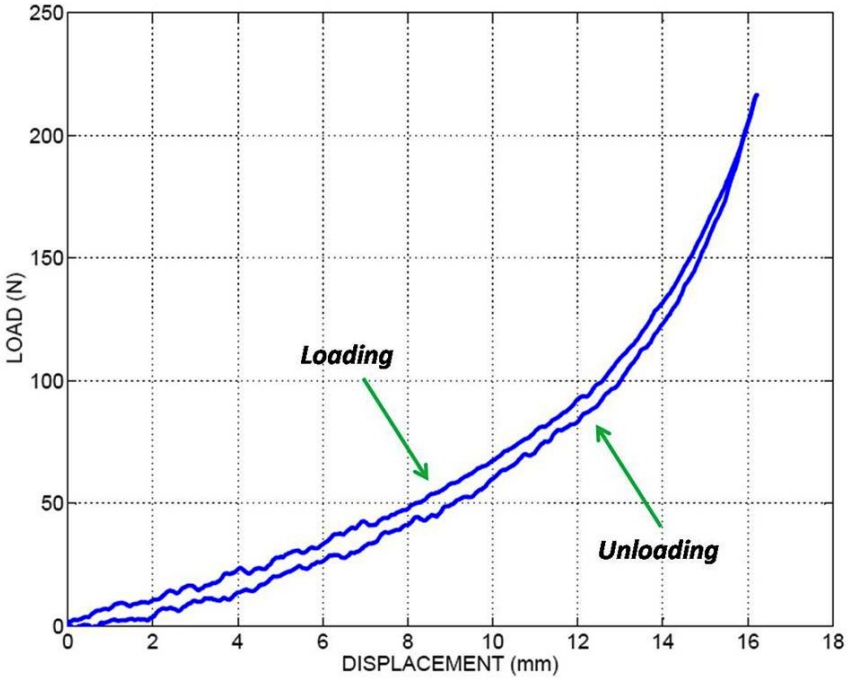

Figure 5.4: Load-deflection plot of polyurethane sample undergoing compression loading followed by unloading.

5.3.2 Static crush response of filled honeycombs

Static axial crushing experiments on filled 3-cell, 7-cell and 19-cell specimens were conducted under similar testing conditions described in the previous section. Here, the main features of response pertaining to the three types of filled specimens under study is discussed. The load-displacement plots for the 3-cell, 7-cell and 19-cell specimens are shown in Figure 5.5, Figure 5.6 and Figure 5.7 respectively. These figures also contain the crush response plots of corresponding unfilled honeycombs and that of the polyurethane block to enable comparison of filled and unfilled honeycomb response and assess the contribution of the polyurethane material during various stages of loading. During the initial stages of loading, typically up to crush distance of less than 1 mm (corresponding to a macroscopic strain of 0.04), the load response is fairly linear. The contribution of the polyurethane material to the total load response up to this point is marginal and the confined honeycomb carries majority of the load.

The filler material is colored and therefore, this phenomenon is not captured clearly in the images. However, upon inspection of the failed specimen, it is concluded that folds were the first to form before another type of failure - longitudinal tearing, which will be described subsequently. The circumferential folds were continuous across the region where longitudinal tearing had occurred thus suggesting that folds were indeed the first to form. Moreover, the macroscopic strain value at first failure was very close to the macroscopic strain corresponding to the first localized failure of the unfilled specimens. The structure continues to carry load and catastrophic failure is not observed at first failure. Hence, the first failure can be described as a stable collapse. Unlike the case of unfilled honeycombs, the stable collapse that is seen in the filled crushing is because localized folds are not completely formed at once due to the presence of the filler material; hence the drop in load is less. In other words, the filler material acts as a cushion in the event of localized collapse. From the load-response plots, the crush distance where the initial failure took place is fairly close to that for the unfilled honeycomb. As loading progresses, localized folds continue to form at a near-constant load value. The load level beyond the initial stable failure is much higher compared to the plateau load of the unfilled honeycomb specimen. This suggests that the load carrying ability of the cells has been enhanced when they are confined with a soft filler material.

With increase in the end-shortening distance, the nearly incompressible filler material begins to exert force in the radial direction of the cylindrical block, thus initiating longitudinal tearing of the honeycomb cells, especially those that are present in the outermost layer. Therefore, the longitudinal tearing is more prominent in the 19-cell samples compared to the 3-cell and 7-cell cases. In contrast to the stable failure corresponding to fold formation, the tearing is characterized by a sudden drop in the load and is therefore an unstable failure. With increase in deformation, more tearing is observed and this failure has the effect of lowering the ability of the filled specimen

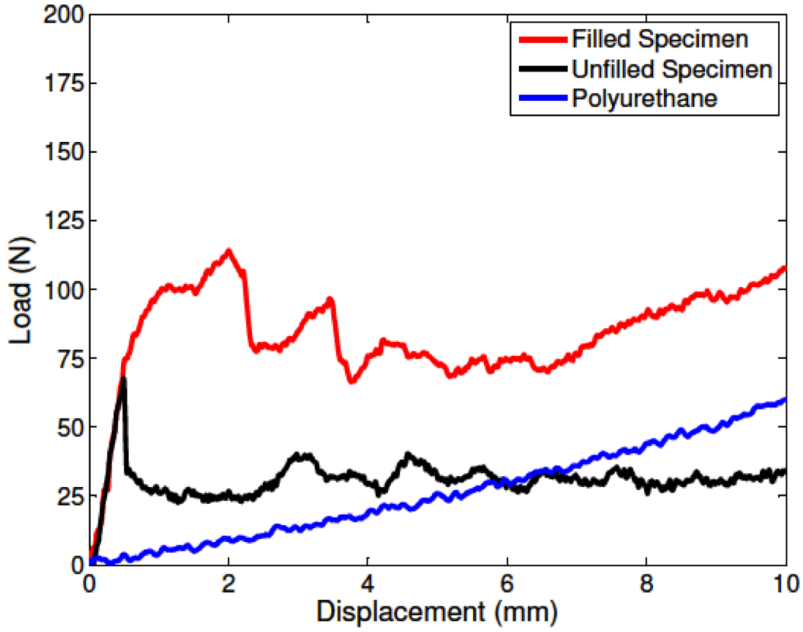

Figure 5.5: Load response of a filled 3-cell specimen shown against that of an unfilled 3-cell specimen. The crush response of the polyurethane block is also shown.

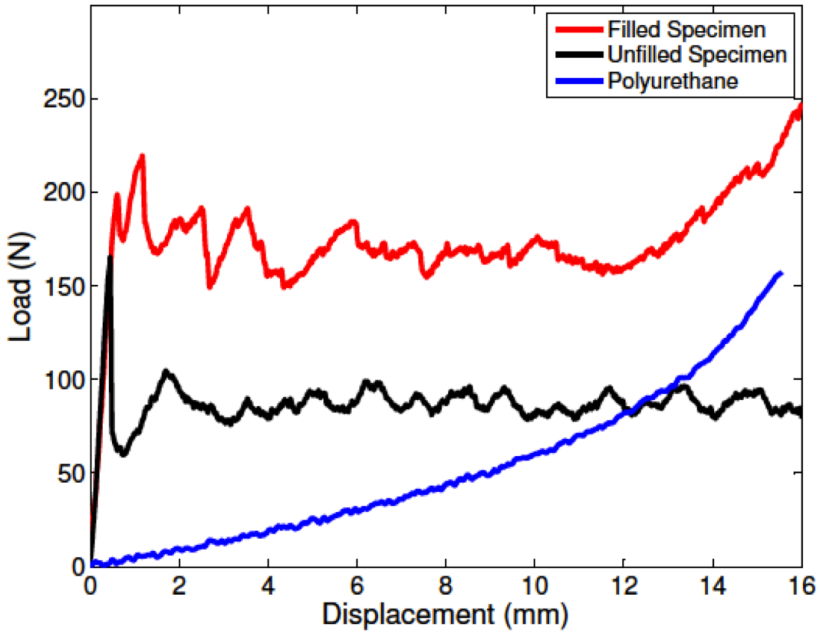

Figure 5.6: Load response of a filled 7-cell specimen shown against that of an unfilled 3-cell specimen. The crush response of the polyurethane block is also shown.

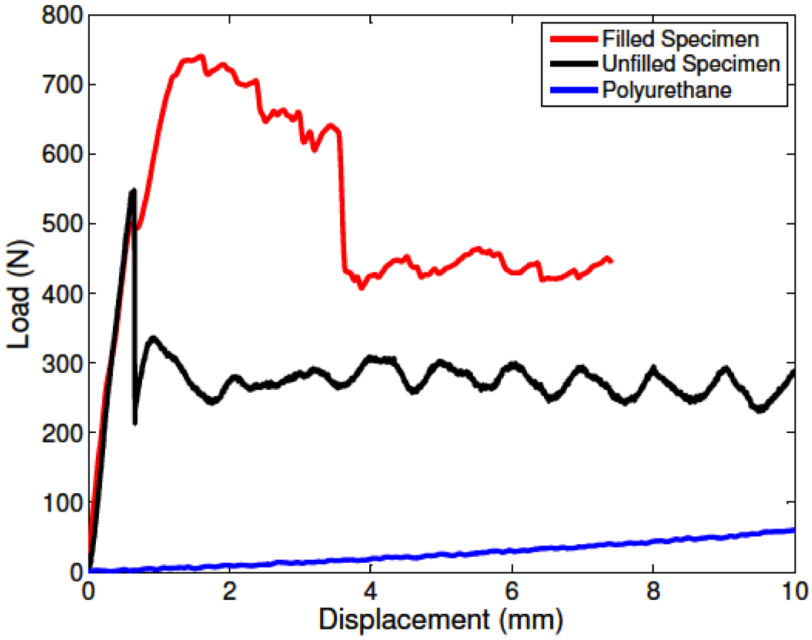

Figure 5.7: Load response of a filled 19-cell specimen shown against that of an unfilled 3-cell specimen. The crush response of the polyurethane block is also shown.

to carry compressive load.

Beyond the initial stable collapse, another type of failure pattern is observed prominently in the 3-cell specimens and mildly in the 7-cell specimens - that of *beam-like* global buckling. This global buckling also leads to longitudinal tearing characterized by fairly sharp drop in the load as can be seen in the load response plot of a 3-cell specimen that is shown in Figure 5.5. However, for specimen with low aspect ratio, 19-cell specimens, global buckling was not observed upon inspection of the damaged honeycomb after the test was complete.

With further increase in crushing, the contribution of polyurethane material to the total load increases and that of the crushing honeycomb decreases. It is also seen that the filled honeycomb that is partially damaged due to global buckling and longitudinal tearing, continues to carry load. The shape of the load-displacement plot is similar to that of the polyurethane filler material, but has a vertical offset which

indicates the load carried by the damaged honeycomb.

The deformed specimens of the filled and unfilled 7-cell and 19-cell specimens are shown in Figure 5.11. The localized folds formed were formed at discontinuous sites along the length of the specimen. This behavior is different from the fold formation in unfilled honeycombs where folds typically appeared at one end and propagated sequentially to the other end. Moreover, due to the presence of the filler material on both surfaces of the cell, the localized folds were not completely formed at the crushed end, unlike in the case of unfilled honeycombs. This constrained deformation at the cell walls resisting the fold formation and instead distributing the folds along the length of the cells (i.e. diffused folding) enables the honeycomb to collapse at a much higher load, in contrast to the unfilled honeycombs where deformation is more localized at the crush end. Therefore, this phenomenon, which is responsible for significant enhancement in the load carrying capacity beyond the initial stable failure, leads to increased energy absorption.

It is instructive to compare the load response of the filled specimen with the sum of the responses of the polyurethane block and the unfilled honeycomb. The total response of the block (filled specimen) is greater than the sum of the load responses of the honeycomb and the polyurethane block. This synergetic load enhancement for 3-cell, 7-cell and 19-cell filled specimens is shown in the shaded portions in Figure 5.8, Figure 5.9 and Figure 5.10 respectively. This behavior suggests that the response of the filled specimen is not linear with respect to the individual responses of the unfilled honeycomb and the filler material block. This phenomenon arises due to the fact that the confined honeycomb crushes in a manner differently compared to the case when it is not filled. In the filled case, the filler material interferes with the fold formation, making it more difficult for the folds to form.

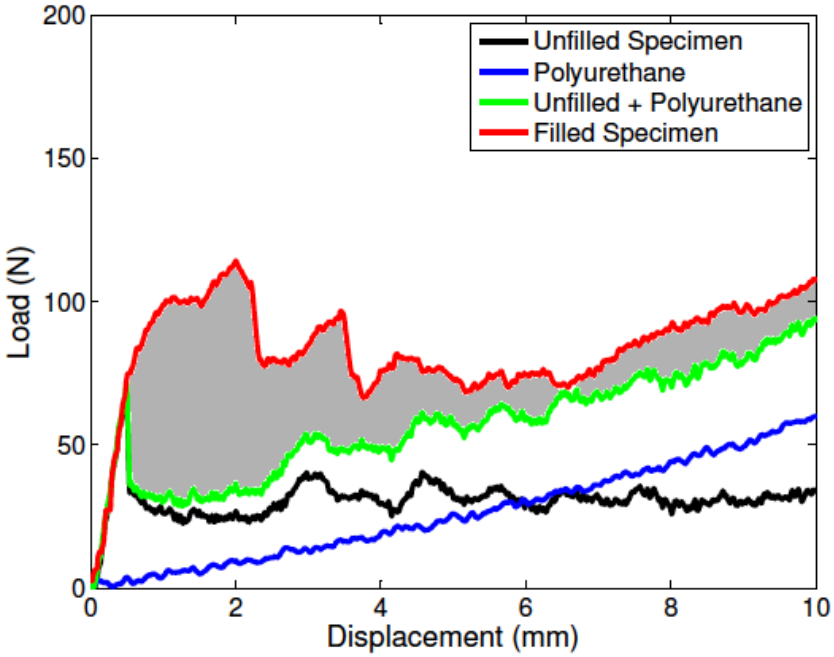

Figure 5.8: The green curve shows the response of the polyurethane block added to the response of the 3-cell unfilled honeycomb. The shaded portion shows synergy in load response for the filled specimen.

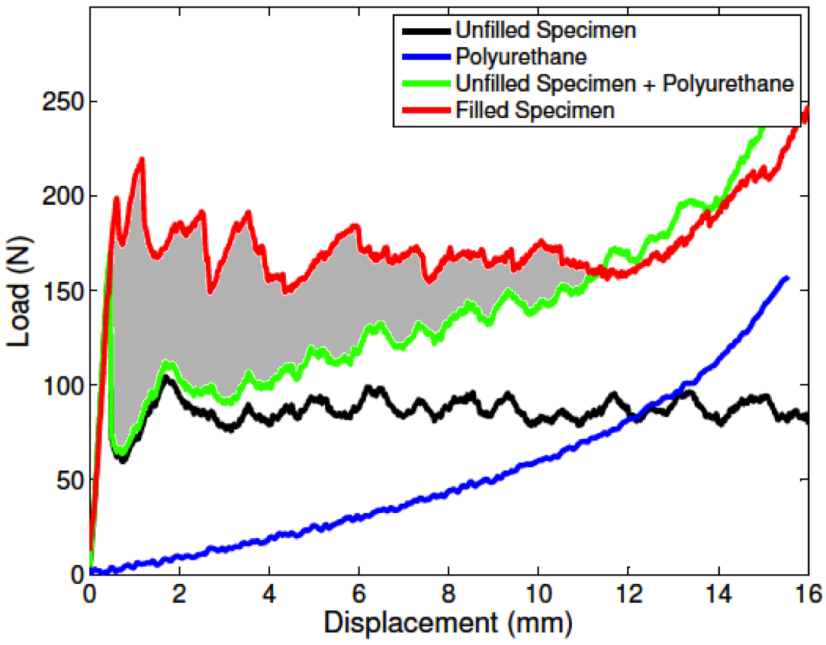

Figure 5.9: The green curve shows the response of the polyurethane block added to the response of the 7-cell unfilled honeycomb. The shaded portion shows synergy in load response for the filled specimen.

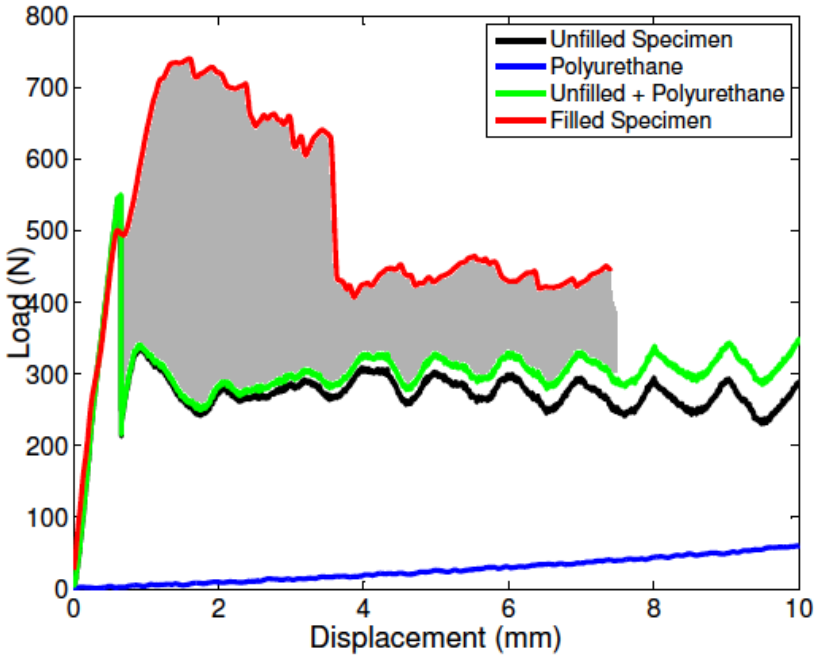

Figure 5.10: The green curve shows the response of the polyurethane block added to the response of the 19-cell unfilled honeycomb. The shaded portion shows synergy in load response for the filled specimen.

5.3.3 Load contribution of the honeycomb-infill cylinders

The 3-cell, 7-cell and 19-cell filled honeycombs were prepared in equal sized molds. It is necessary to separate out the contribution of the honeycomb-infill cylinders (HIC) from the total load response. For the filled honeycomb specimen used in this study, the HIC is defined as that part of the specimen that consists of each cell and filler material which lies inside. Therefore, the remaining part of the specimen is the outer layer composed of the filler material. For example, in a 3-cell filled specimen, the HIC consists of three cells and the filler material that lies inside each of the cells. For a given filled specimen consisting of n cells, if $P_T^{(n)}$ is the total response at a particular crush distance, then this total response is a contribution of the load response of the HIC denoted by $P_{HIC}^{(n)}$ and that of the remaining portion of the filler material which is denoted by $P_R^{(n)}$. Therefore, $P_T^{(n)} = P_{HIC}^{(n)} + P_R^{(n)}$. The response of the outer layer can be obtained from the load-response plot of polyurethane block (P_{fill}), which is of the

Figure 5.11: The images comparing the deformations of filled and unfilled 7-cell and 19-cell honeycombs. The unfilled specimens are shown on the left column and the filled specimens on the right column. Notice the progressive localized failure spread over a continuous region in the unfilled specimens. In contrast, the localized folds in the filled specimens occur in a random fashion. Longitudinal tearing is seen in both the filled honeycombs. In the filled 7-cell specimen, notice some global deformation that is not present in the filled 19-cell specimen due to lower aspect ratio.

same size as those of the filled honeycomb specimens. If $V_f^{(n)}$ is the volume fraction of the outer layer, then $P_R^{(n)} = P_{fill} V_f^{(n)}$. Therefore, the response of the HIC is given by $P_{HIC}^{(n)} = P_T^{(n)} - P_{fill} V_f^{(n)}$. The normalized response is then given by $F_{HIC}^{(n)} = P_{HIC}^{(n)}/n$. The normalized load $F_{HIC}^{(n)}$ enables us to compare the amount of load carried by the HIC per cylinder across specimens having different number of filled cells and is shown for 3-cell, 7-cell and 19-cell specimens in Figure 5.12. With reference to Figure 5.12, one observes that the load carried by the all three kinds of specimens considered is not significantly different from one another. The slightly higher response of the 19-cell specimen can be explained due to the fact that it is more stable and not prone to global buckling when compared to the response of 3-cell and 7-cell specimens. Therefore, this plot suggests that scaling in terms of number of cells has no significant influence on the load carrying capacity of the HIC per cylinder of these specimens. Here, it is instructive to recall a similar result for unfilled honeycombs that was reported for static crush response of unfilled specimens by Mellquist & Waas (2004).

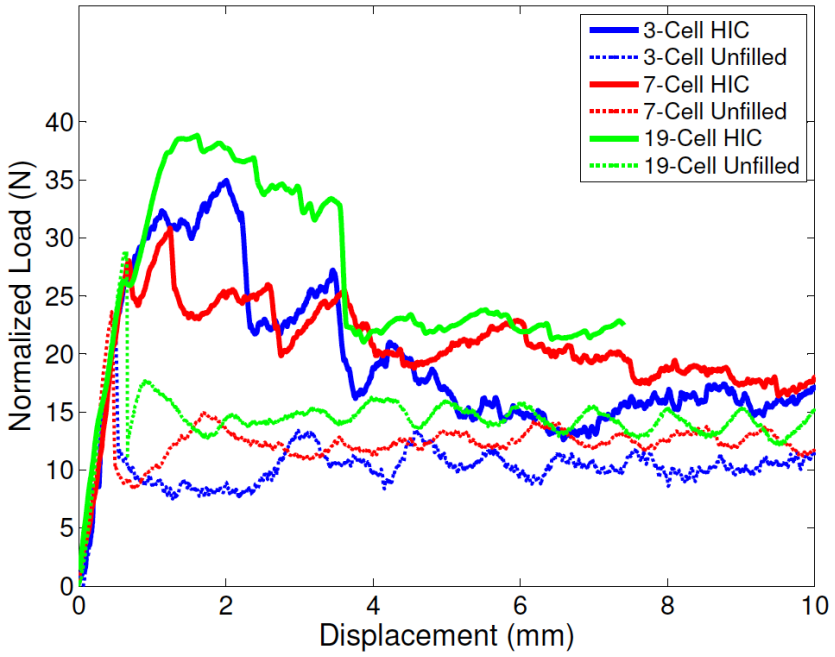

Figure 5.12: Plot showing the normalized load response of honeycomb-infill cylinder for a 3-cell, 7-cell and 19-cell specimens. The normalized load per cell for the corresponding unfilled honeycomb is also shown.

5.3.4 Finite Element Simulation

This section presents finite element simulation of a representative filled 7-cell specimen. Here, 7-cell is chosen as a representative sample and simulations described shortly would hold good for specimens with any number of cells. First, the polyurethane compression experiment was validated using hyperelastic model in ABAQUS/Standard. A cylindrical model with dimensions of the polyurethane test specimen was created with reduced integration eight node brick solid brick elements (C38DR). The nominal stress-strain data of the polyurethane sample obtained from the uniaxial crush experiment was used as an input in hyperelastic material definition. Marlow's hyperelastic model was chosen to simulate the hyperelastic behavior of polyurethane. The Marlow's hyperelastic model is best suited when only limited type of test data are present - in our case, being the uniaxial test data. Before proceeding with the simulation of the filled honeycomb, it is instructive to understand how the boundary conditions at the top and bottom conditions influence the uniaxial compression response of polyurethane. For the first set of simulations, the top and bottom faces of the model were held against movement in the radial direction. The bottom face was fixed in the axial direction and displacement was specified at the top face. The stress-strain plot was backed out and the result was in close agreement with that observed in the experiment. Owing to the incompressibility of the polyurethane material, the onset of barreling was seen for macroscopic strain of 0.25. For the next set of simulation, the top and bottom surfaces were assumed to be frictionless. The stress-strain plot backed out was again, in close agreement with the experimental data and was negligibly lower than that from the first simulation set. Since in the experiment, the constraint at the top and bottom faces of the specimen lie in between these two extreme cases considered in the simulation, the data obtained from the uniaxial compression test is assumed to characterize the polyurethane closely.

Finite element model of a 7-cell honeycomb was created using S4R shell elements

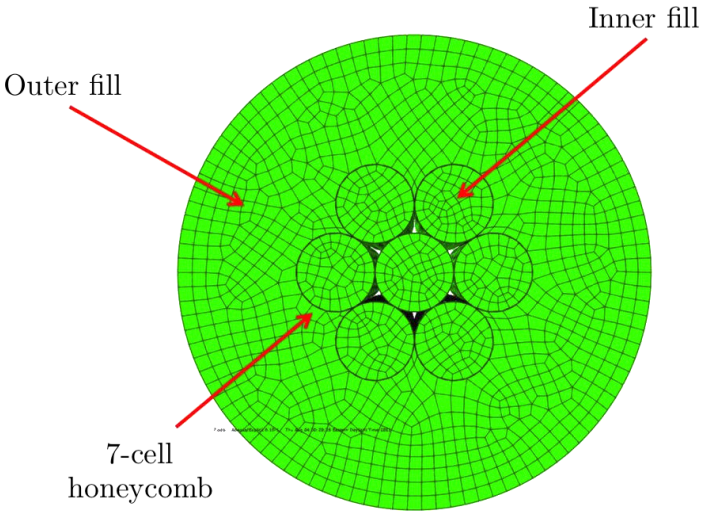

Figure 5.13: The finite element mesh (top view), showing the honeycomb filled with polyurethane (Inner Fill) and surrounding it (Outer Fill). The space formed where three cells meet is not filled to make the explicit crush simulation more computationally affordable by reducing the surface-to-surface constraints.

using the dimensions of the honeycomb microstructure. The mesh contained 12, 928 nodes and 13, 482 elements. In this model, ideal shell-to-shell contact was assumed, i.e. each cell was in contact with its neighbor through point contact. The real honeycomb cell deviates from the perfect geometry due to presence of localized geometrical imperfections, non-uniform wall thickness, out-of-roundness and non-uniform cell-to-cell contact. Out of these, the crush response is most influenced by the presence of geometrical imperfections (Babcock (1983)). Linear eigenbuckling analysis was conducted and the first eigen mode was chosen to seed the honeycomb structure in the filled specimen model. Geometrical imperfections were added to perturb the perfect geometry of the shell elements with imperfection amplitudes. The method adopted to arrive at the imperfection levels that were representative of geometrical imperfections of real honeycombs was as follows: The maximum deviation from perfect circular shape was calculated using measured cell dimensions. The maximum deviation in cell radius value was 0.36 mm, which corresponded to approximately 5.5 times the

wall thickness. Using this estimate, the imperfection amplitude of 0.128 and 0.194 (corresponding to 200% and 300% of the shell wall thickness) were chosen such that the initial slope of the resulting unfilled crushing simulation was not significantly different from the initial slope measured from the unfilled static crush experiment. The inner filling and outer cover containing polyurethane was created using reduced integration eight node solid brick elements (C38DR). The top view of the finite element model is shown in Figure 5.13. In order to simulate the bonding between the filler material and the shell, the surface nodes of the shells were tied to those of the surrounding solid elements using the surface-to-surface tie constraint. Hence, through this constraint, perfect bonding was assumed between the honeycomb and filler material interface. ABAQUS/Explicit was used to simulate the crushing response because it is computationally efficient, given the complexity and the interactions present in the model. The boundary conditions were specified as follows: the top and bottom surfaces of the model were constrained in the radial direction. The bottom surface was constrained in the longitudinal direction and crush velocity of 10 mm/sec was specified at the top surface. The kinetic energy of the structure was much smaller compared to the strain energy of the structure and therefore, the use of such prescribed velocity to mimic the quasi-static response was justified. Rate dependent data for the polycarbonate material was taken from Mulliken & Boyce (2006) with the initial yield stress of 66 MPa. However, due to the low local values of strain-rate, the rate effects have marginal influence on the crush simulation. The crush simulation of unfilled 7-cell honeycomb model was also performed with inputs similar to the one described above for the case of filled honeycomb. Next, we describe in parallel the crush simulation response of filled and unfilled 7-cell models.

The load vs. end-shortening plot of the two models is shown in Figure 5.14. The load response of the 7-cell filled honeycomb model was linear during initial stages of loading and the load peaked to a maximum (peak load) and dropped. This load drop

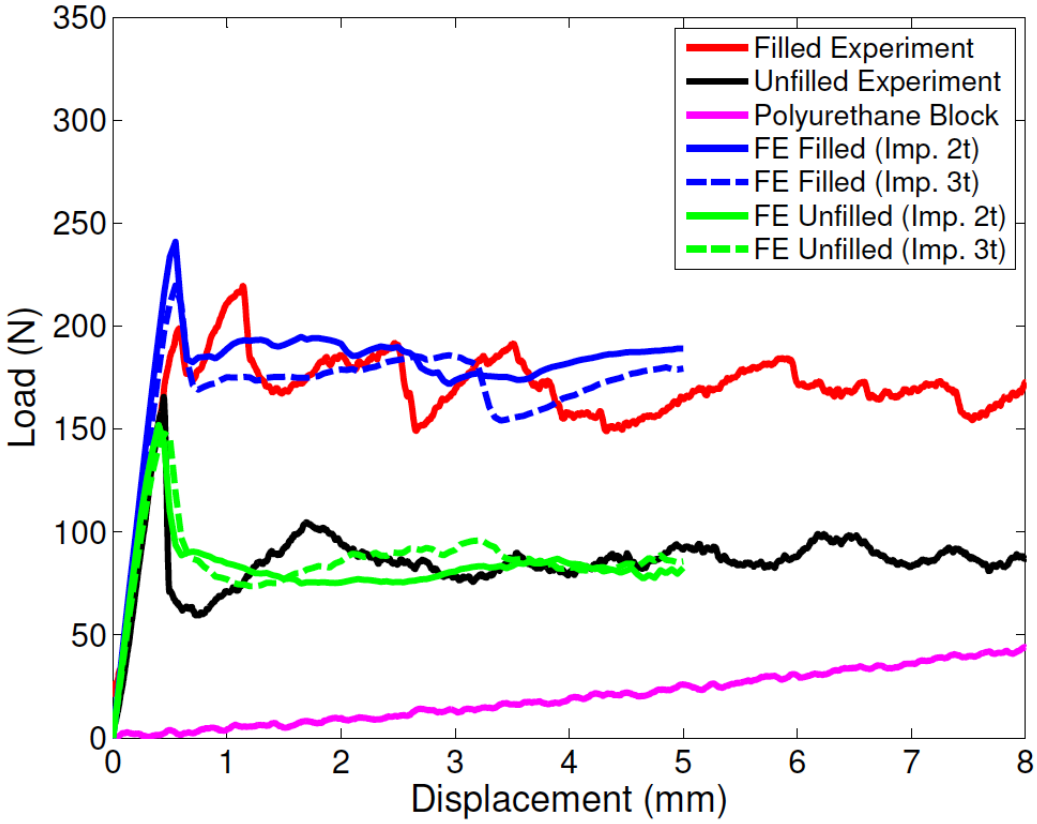

Figure 5.14: Plot showing the comparison of the load response of 7-cell honeycomb experiments and finite element simulation for both filled and unfilled honeycombs.

was accompanied by localized fold formation near one of the ends. The unfilled model also showed a linear regime with slope very close to that of the filled model. However, here, the peak load was lower than that of the filled model and was accompanied by localized fold formation with folds being localized at the ends, whereas the buckling pattern is diffused in the case of the filled honeycombs. Thereafter, the load response for both the models was fairly constant (plateau load) where more folds were formed. New folds were completely formed once the previous folds were nearly complete. In the case of the filled model, folds were formed only partially before the next folds began to completely form. This is attributed to the fact that the shell was undergoing constrained deformation, due to the lateral support of the filler material, with the ability of fold formation being inhibited due to the presence of the filler material. Furthermore, because the filler hardens non-linearly (that is, its stiffness increases with axial deformation) the lateral support provided by the filler to the buckling cell walls increase (this effect is similar as a beam in a non-linear elastic hardening foundation) as the loading increases. Consequently, the plateau level of the filled model was much higher compared to that of the unfilled model. Of course, during the plateau level, the filler lateral stiffness stays constant. Overall, the predicted response of both the models was in fairly good agreement with the experimental data with the exception of the peak load for the crush simulation of the filled model. A series of images of the deformation response of filled and unfilled models are shown in Figure 5.15. Individual cells in the filled model also showed signs of global deformation and this phenomenon was also observed in the experiment. Note that in the above crush simulation, there was no mechanism to accommodate longitudinal tearing of the honeycomb. This aspect is beyond the scope of the present investigation and is relegated to a future study.

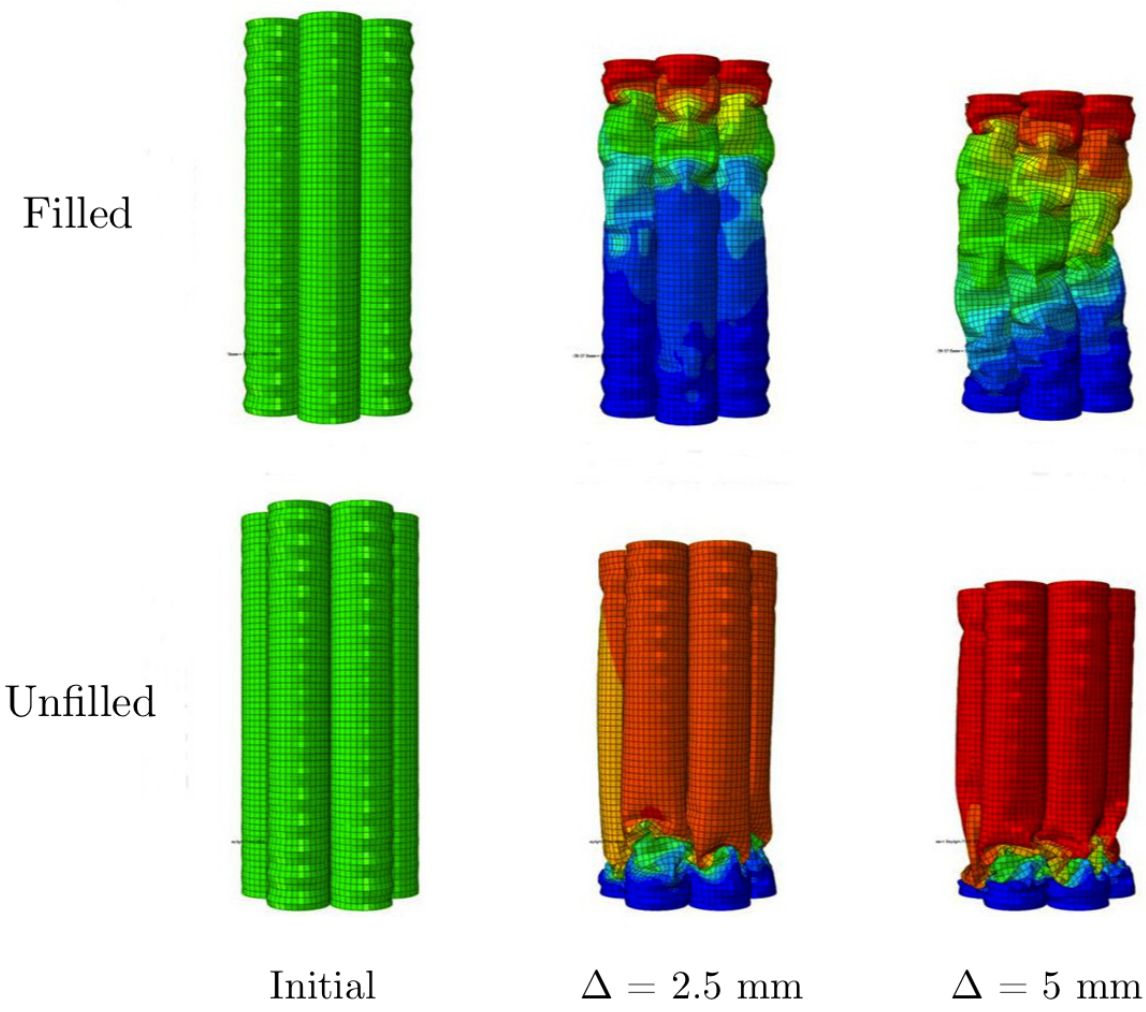

Figure 5.15: Deformation of filled and unfilled 7-cell honeycombs obtained from explicit finite element simulation. The folding in the filled model is diffused compared to the unfilled model where the failure is localized. The filled model shows cells deforming globally and this behavior is not present in the unfilled specimen.

5.4 Effect of filler stiffness on the crush response

In the previous section, it was shown that the presence of the filler material changes the mode of deformation in the honeycomb when compared to the unfilled case. This change in deformation is due to the stabilizing effect of the filler material. This is related to the response of the beam on an elastic foundation. It is seen that an increase in the foundation stiffness has an effect on decreasing the wavelength of the eigenmode of the beam. Now, in our present problem, keeping the honeycomb base system fixed, let us compare the effect of the stiffness of the filler on the response of the filled structure. This analysis has been performed via finite element simulations similar to that described in the previous study. Five stress-strain responses for the elastomers are considered. Curve B is that of polyurethane that has been described in the earlier experimental study, curve D is PDMS (polydimethysiloxane). The curves A, C and D are created such that the polymer stiffness increases from curves A to D as shown in Figure 5.16. The load-displacement response of composite honeycombs filled with these elastomers is shown in Figure 5.17. It is observed that with increase in the stiffness of the filler material, the collapse changes from unstable to stable behavior. Moreover, the load at which first collapse occurs shifts to a higher load with increase in the filler stiffness. The contribution of the honeycomb component to the load response is shown in Figure 5.18. Again, it is noticed that the peak load increases and tends to become more stable when the surrounding elastomer stiffness increases. The mode of collapse associated with these cases is shown in Figure 5.19. For curve A that has low stiffness, the mode of collapse is dominated by the diamond shape with larger-wavelength (diffused). Recall that in the extreme limit with no filler, the collapse shape would be dominated by the diamond pattern. Now, with increase in the foundation stiffness the diffused folds tend to be dominated by the concertina (axisymmetric) pattern with decrease in the fold wavelength.

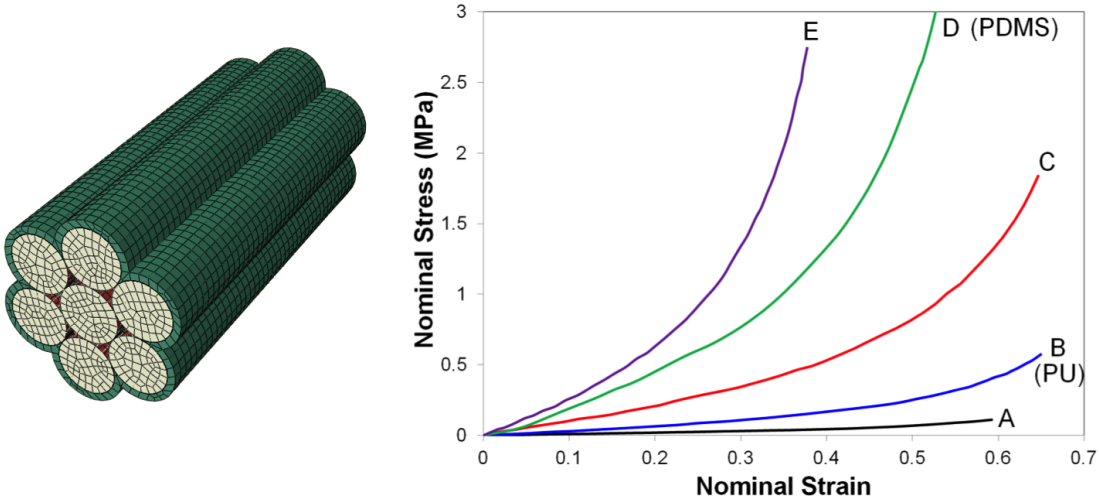

Figure 5.16: Finite element model of the filled honeycomb (left). Nominal stress vs. strain response of elastomers considered in the study. The curve B corresponds to polyurethane and curve D corresponds to PDMS.

5.5 Conclusions

In this chapter, the axial crush response of filled 3-cell, 7-cell and 19-cell specimens was studied through uniaxial quasi-static crush experiments, motivated by prior work reported in Mellquist & Waas (2004). Soft elastomer polyurethane was used as the filler material. Explicit finite element modeling was used to simulate the crush behavior of a representative 7-cell filled honeycomb. The main findings of this work are as follows

1. Beyond the initial failure, the filled honeycombs had greater load carrying capacity compared to the unfilled honeycombs, due to the lateral wall support provided by the filler.

2. Initial failure in filled honeycombs was a stable failure in contrast to unfilled honeycombs, where the catastrophic failure was accompanied by a large and instantaneous drop in load.

3. Initial failure was characterized by fold formation. With increase in the load,

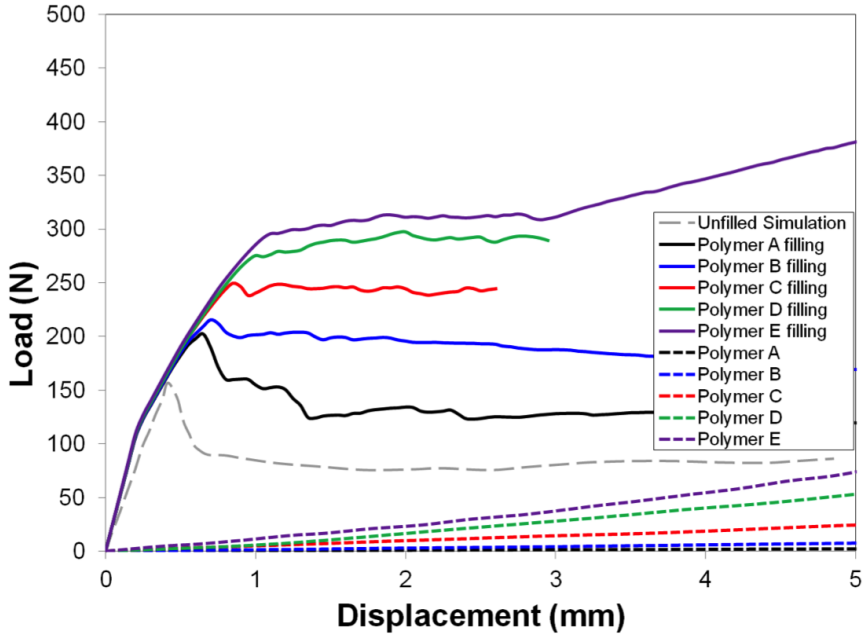

Figure 5.17: Load response of filled honeycomb with varying elastomeric properties and corresponding response of an equal sized elastomer.

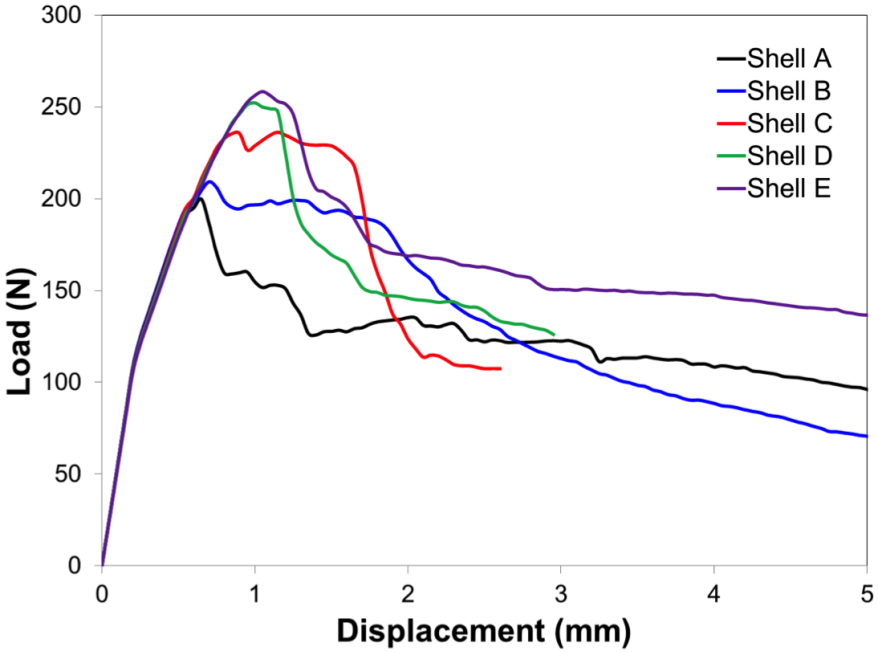

Figure 5.18: Load carried by the honeycomb during the axial crushing of the filled honeycomb for varying filler stiffness

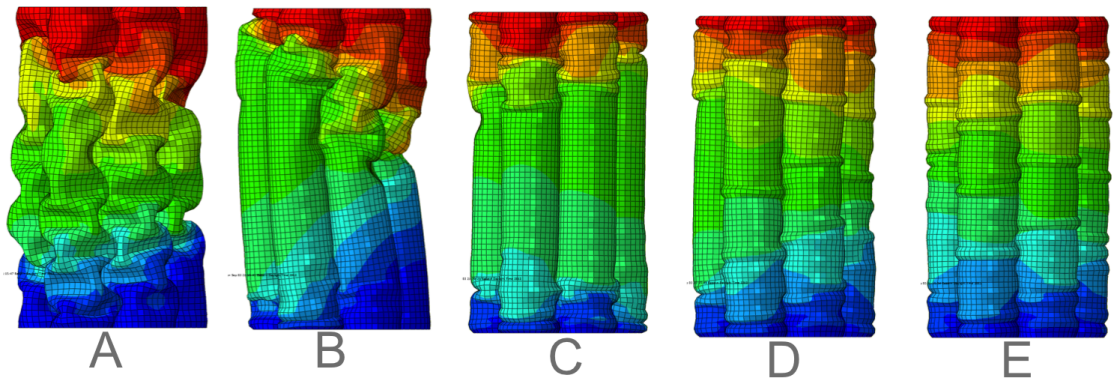

Figure 5.19: The mode of collapse in the honeycomb for the five cases considered.

the folds appeared at disconnected regions along the length of the individual cells, which is referred to as distributed fold formation. In contrast, folds in the unfilled honeycombs usually propagate from one end to the other via concertina-diamond mode, thus localizing the area of dissipation. These experimental observations were reproduced by the finite element crush simulation, lending credence to the developed model and the modeling strategy for future studies

4. The normalized load carrying capacity of the filled honeycomb was more or less similar for 3-cell, 7-cell and 19-cell specimens, reinforcing a similar result for unfilled honeycombs reported in Mellquist & Waas (2004).

5. Apart from fold formation, other failure modes were observed which contributed to reducing the load carrying capacity of the specimen, such as global buckling and longitudinal tearing. These mechanisms, if suppressed, can lead to even better mechanical performance.

6. The honeycombs having high aspect ratio (such as the 3-cell specimen) were prone to global buckling even under confinement with the soft polyurethane material. This effect was not observed for comparatively low aspect ratio honeycomb specimen (such as the 19-cell specimen).

7. From the parametric study conducted on the filler material, the relative stiffness of the filler material controls the mode of deformation and the wavelength of the diffused folds. Especially, stiff filler material would result in a lower wavelength diffused folding in the cell walls of the honeycomb.

5.6 APPENDIX: Axial crush of filled hexagonal aluminum honeycomb

In this appendix, results of another honeycomb-filler combination, namely 7-cell aluminum honeycomb filled with PDMS elastomer is reported. Aluminum honeycombs (alloy 3003) with hexagonal microstructure are used for the static out-of-plane crush response study. The out-of-plane length of the honeycomb is 12.7 mm, the edge length is 4.45 mm and wall thickness is 0.09 mm. Specimens are placed in a cylindrical mould of height 25.4 mm and diameter 22.8 mm and PDMS resin + hardener mix is poured over. Next, the air bubbles are removed using a vacuum chamber. The sample is heated at 100°C for 45 minutes and left to cool. The excess PDMS filler is carefully cut and the top surface is ground using an emery paper. The sample is placed in an INSTRON machine and loaded quasi-statically at a crush rate of 0.033 mm/sec. Data are acquired at the rate of 10 Hz and images are acquired every 5 seconds. Test was also conducted on 7-cell unfilled samples and an equal sized PDMS specimen. The load vs. end-shortening plot of these specimens are shown in Figure 5.20.

With reference to this plot, the unfilled specimen response is nearly linear where axial crushing takes place with no fold formation. The load rises to a peak load of 1,900 N. At the peak, folding is seen at one end of the specimen and the load drops to approximately 550 N. This first collapse is unstable where stiffness becomes negative and a sharp drop in load ($\approx$ 1,350 N) is seen over a relatively small crush distance. Thereafter, the load maintains a relatively constant value where new folds are formed.

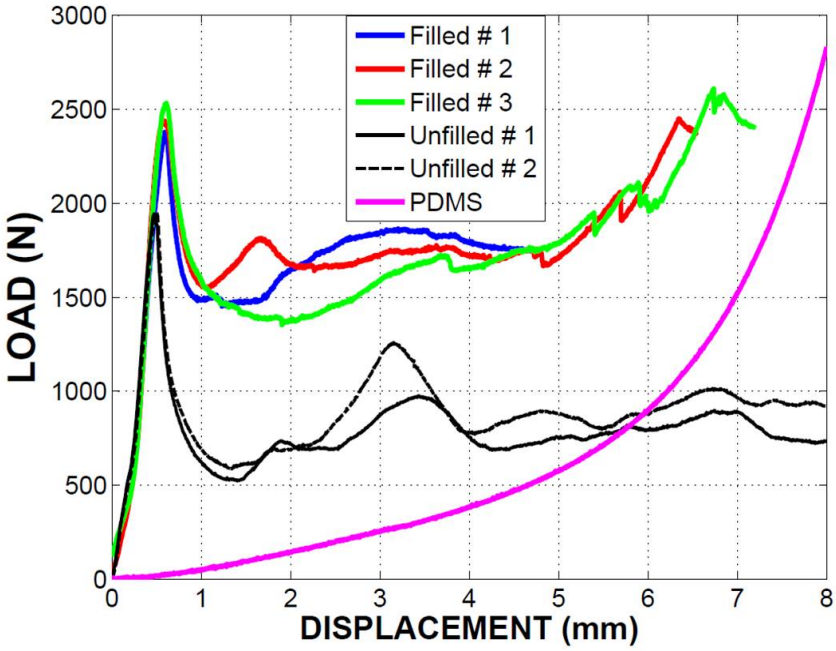

Figure 5.20: Load-deflection plot of 7-cell filled and unfilled hexagonal aluminum honeycomb. The load response plot of PDMS is also shown for comparison.

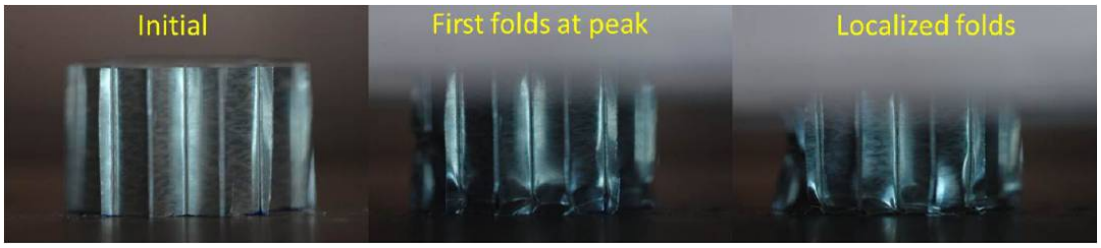

Figure 5.21: Image showing first fold formation at first peak (center) and localized folding (right) at the bottom of the specimen, beyond the peak in the unfilled honeycomb experiment.

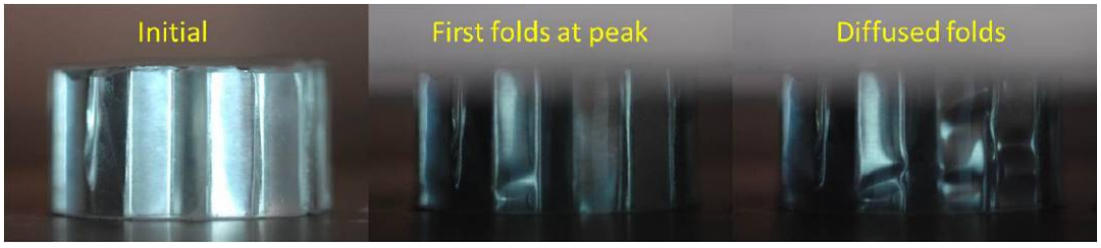

Figure 5.22: Image showing first fold formation at first peak (center) and diffused folding (right) beyond the peak in the filled honeycomb experiment.

This plateau load is close to 800 N. The folds are localized and progressively form from one end to the other. The deformation sequence of the unfilled specimen is shown in Figure 5.22. In the case of the filled specimen, there is an initial linear region where the load peaks to a value of approximately 2,450 N compared to peak value of 1,900 N for the unfilled specimen. Up to this point, the crushing in the sample is mainly axial with no visible folds. By comparing with the PDMS response in Figure 5.20, the contribution of the PDMS to the total load is marginal and the honeycomb carries majority of the load. Moreover, due to marginal contribution of PDMS here, the slope of the linear region for the unfilled and filled samples is similar. Beyond the peak, the load drops to nearly 1,500 N and the first folds appear immediately after the peak. The drop in load in the filled specimen is 950 N compared to load drop of 1,350 N in the unfilled specimen. This reduction in load drop immediately after the peak indicates that the filler material has partially stabilized the first failure event. Thereafter, the load is at fairly constant value of 1,700 N, again plateau load value higher than its unfilled counterpart. The folds formed are diffused and not localized as seen in the unfilled honeycomb. The deformation sequence of the filled specimen is shown in Figure 5.21. This feature is identical to that in our study with polycarbonate-polyurethane out-of-plane crush experiments, which was reported in the previous sections. Apart from diffused folding, longitudinal tearing was another failure that was observed in the honeycomb specimen.

Synergistic response of the filled honeycomb is shown in Figure 5.23. In the plateau region marked in the figure, the load in the filled specimen is nearly constant (plateau load). Thereafter, the filled response rises and takes the shape of the PDMS response at the given end-shortening value. The end-shortening value (Δ_C) where the unfilled response changes from near constant plateau to a rise, roughly corresponds to the point where the PDMS load value is higher than the plateau load of

the unfilled honeycomb specimen[2]. This behavior suggests that as long as the PDMS load level is lower than the plateau load value of unfilled specimen, the corresponding filled specimen exhibits plateau (dissipates the additional external work done by loading). As soon as the PDMS load level is higher than the unfilled plateau, the filled honeycomb starts to store energy. In other words, beyond (Δ_C), the additional external work done in loading is now stored in the structure as elastic strain energy. This feature was also observed in our study with polycarbonate honeycomb filled with polyurethane filler reported in earlier sections of this chapter.

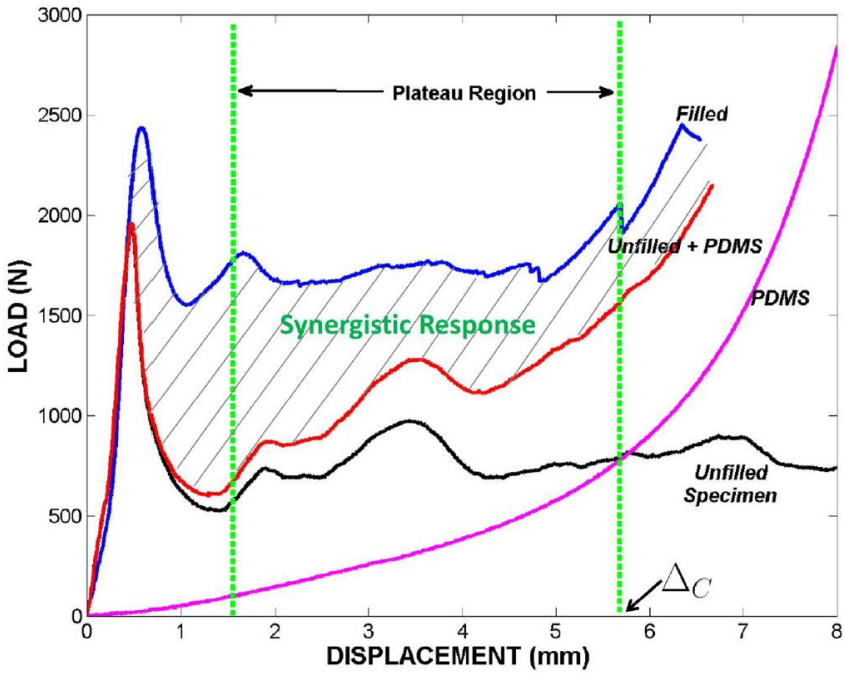

Figure 5.23: Plot showing the synergistic response of the filled honeycomb. The end-shortening value (Δ_C) is at the end of the plateau region, where filled load response rises with further increase in end-shortening.

[2]Recall that in the case of the 3-cell and 7-cell honeycomb filled with polyurethane, similar trend was observed

CHAPTER VI

Dynamic Crush Response of Filled Honeycombs: Out-of-Plane direction

6.1 Introduction

In the previous chapter, the quasi-static axial crushing of polyurethane filled honeycomb was presented. The present chapter focusses on the dynamic counterpart. A wave loading device (WLD) is used to perform the experiments. The results obtained here are compared with the static crushing of filled honeycombs.

6.2 Test Setup

Recall that in Chapter III, the wave loading device was used to perform dynamic compression tests on unfilled honeycombs. It was found that the setup cannot be used to crush honeycombs larger than 7-cell specimens for large crush distances. This is because the specimens' relatively large stiffness in the axial direction retards the motion of the incident bar rapidly. Therefore, a larger diameter split-Hopkinson pressure bar setup is used in the present work. Since the bar diameters of the new setup are of size 38.1 mm (1.5 in), the number of cell clusters can also be increased. The symmetric configuration for a hexagonally packed cluster of 7 cells and 19 cells can be easily be accommodated in this setup. Hence, 19-cell filled specimens are

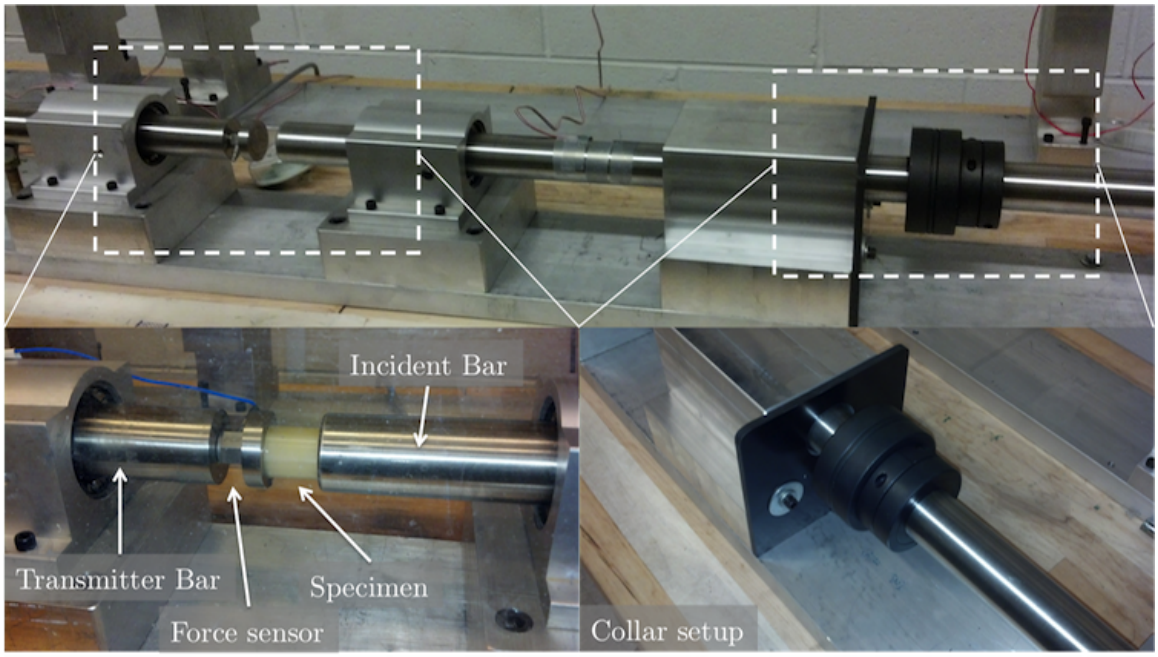

Figure 6.1: Image of the WLD setup modified from an existing split-Hopkinson pressure bar. Important components are also shown.

chosen in this study. An image of the present setup with important details is shown in Figure 6.1. The drawing of this setup with dimensions is shown in Figure 6.2.

A notable difference in the present WLD setup is the introduction of the collar setup. If the collar setup is not used, then there is a possibility that the incident bar will impact the end with the force sensor. Such a metal-to-metal contact at high velocities would most likely damage the force sensor. With the collar setup in place, the incident bar is stopped when the collar hits the rubber pad. A part of the impact force is absorbed by the rubber pad and also by the aluminum post to which the rubber pad is attached. Thus, the collar prevents the incident bar from moving more than a desired amount which is equal to the desired total crush distance of the specimen. This distance was set between 10.2 to 15.2 mm (i.e. $0.4 - 0.6$ in), which means that the setup can crush about 40 to 60% of the specimen length along the axial direction.

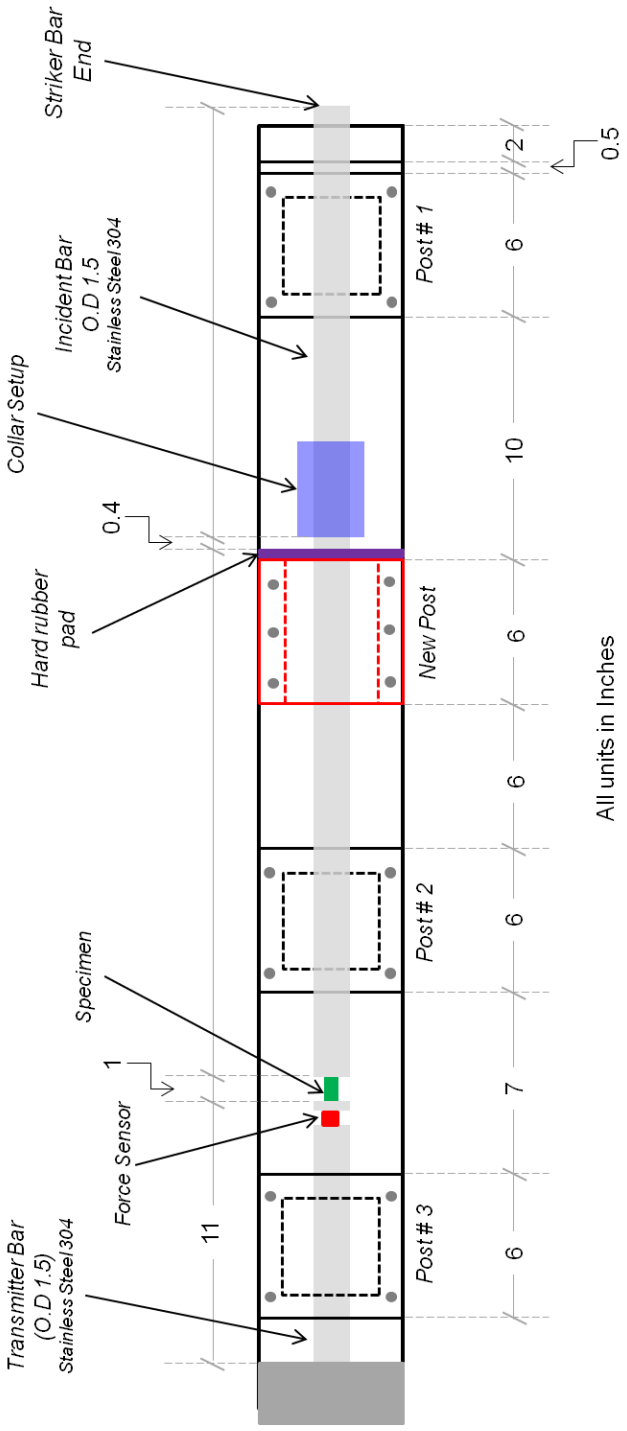

Figure 6.2: Details of the WLD device used in the present work. Units are in inches.

6.3 Experiment

The force sensor used here is PCB Piezotronics model 208C03 of 500 lbf capacity. A metal disc is attached in front of the force sensor to accommodate the specimen. The specimen is then sandwiched between the metal disc and the incident bar before the test. Six different firing pressures in the gas-gun are used in this study, these being 50 psi, 100 psi, 150 psi, 250 psi, 325 psi ands 400 psi. Images from the experiment are recorded using a high speed camera (Photron SAX) at 50,000 frames per second.

The firing pressure dictates how fast the striker bar exits the gas chamber. The striker bar impacts the incident bar at the striker bar end (see Figure 6.2). As soon as it hits the incident bar head-on, a compression stress pulse travels with the speed of sound in the incident bar and travels towards the specimen. The amplitude of this stress pulse varies with the striker bar velocity and the length of the pulse depends on the length of the striker bar. The crush velocity is determined by the displacement rate of the incident bar that is in contact with the specimen. The crush velocity depends on the velocity of the striker bar. Figure 6.3 shows displacement imparted to the specimen vs. time as a function of the firing pressure. Since the displacement data are obtained from the high speed images, the displacement information is obtained only at discrete intervals. To compare this information with the load signal, more displacement data points are needed. Thus, the displacement vs. time data for every firing pressure are represented using a function $d(t)$ via curve fitting. It is found that the function that best represents the ramp-step displacement-time profile is "sum-of-sines", of the form

$$d(t) = \sum_{j=1}^{N} [a_j \sin(b_j t + c_j)] \tag{6.1}$$

where the constants a_j, b_j and c_j are determined using least square curve fitting. For the present data set, six sine terms are sufficient to satisfactorily represent the ramp-rest profile. For each firing pressure value, the displacement-time function is

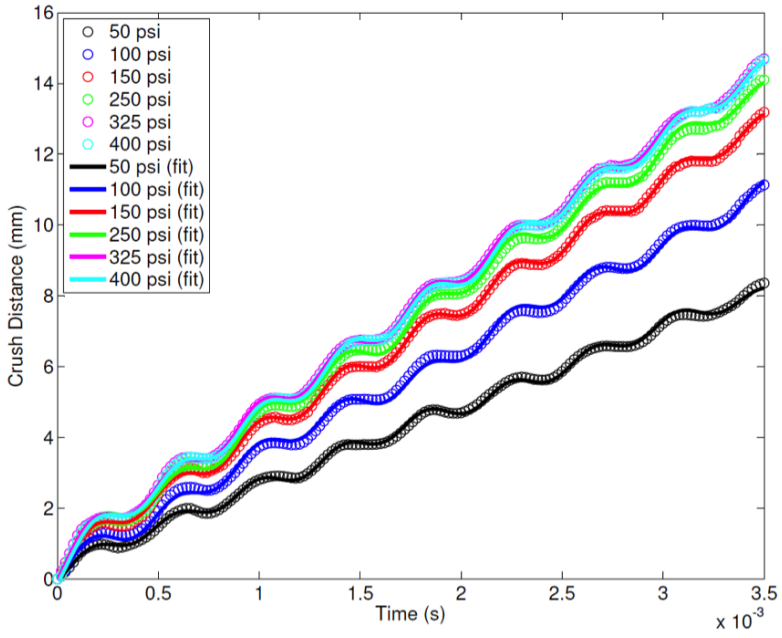

Figure 6.3: Plot of displacement vs. time for the specimen-end of the incident bar as a function of firing pressure.

also plotted in Figure 6.3 along with the discrete data points measured from the images. The time taken for successive ramp cycles t_s is equal to the time taken for the stress wave in the incident bar to travel twice along its length. Assuming 1-D wave theory holds good, $t_s^{1-D} = 0.412$ ms using standard properties of steel. This is in close agreement with the measured value from Figure 6.3, which is $t_s^{expt} = 0.4$ ms. The value of t_s is independent of the firing pressure because it only depends on the length and material properties of the incident bar.

The crush velocity profile of the incident-bar can now be obtained by differentiating the displacement function $d(t)$. Figure 6.4 shows the velocity profile as a function of time. Here, average and peak velocities are also plotted as a function of the firing pressure. Note that the peak velocity corresponds to the velocity during ramping motion, which is a consequence of the compressive stress pulse reflecting as a tensile pulse. On the other hand, the average velocity corresponds to the rigid-body motion of the incident bar. The maximum velocity is more meaningful compared to the average velocity because maximum velocity is attained during the ramping motion

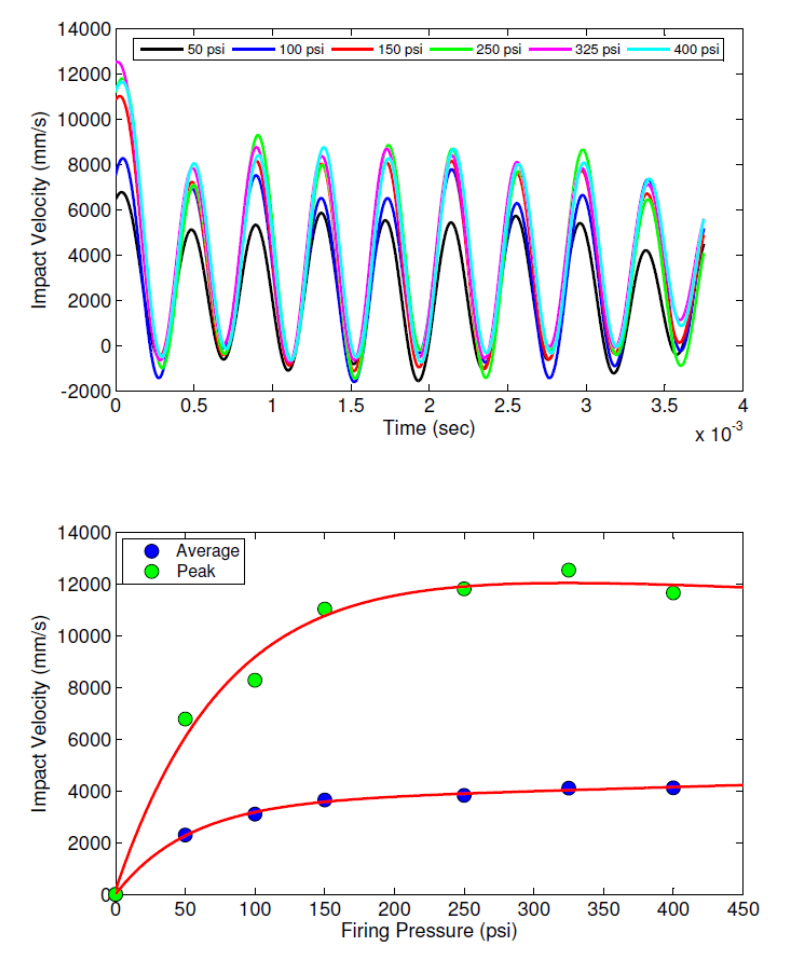

Figure 6.4: Plot of velocity vs. time for the specimen-end of the incident bar as a function of firing pressure (top). Average and maximum peak velocities as a function of firing pressure (bottom).

of the incident bar, which is the velocity imparted the specimen during crushing. It is seen that the crush velocity saturates at a firing pressure of around 150 psi. The compressed gas in the chamber expands to propel the striker bar. However, the design of the gas chamber and the nozzle where gas is forced to propel the striker bar sets the limit on the rate at which the gas can expand. Details of the physics concerning such a process can be found in Rohrbach et al. (2012), who have derived equations describing the exit velocity of a projectile in an air cannon in terms of its geometry and properties of the propellant gas.

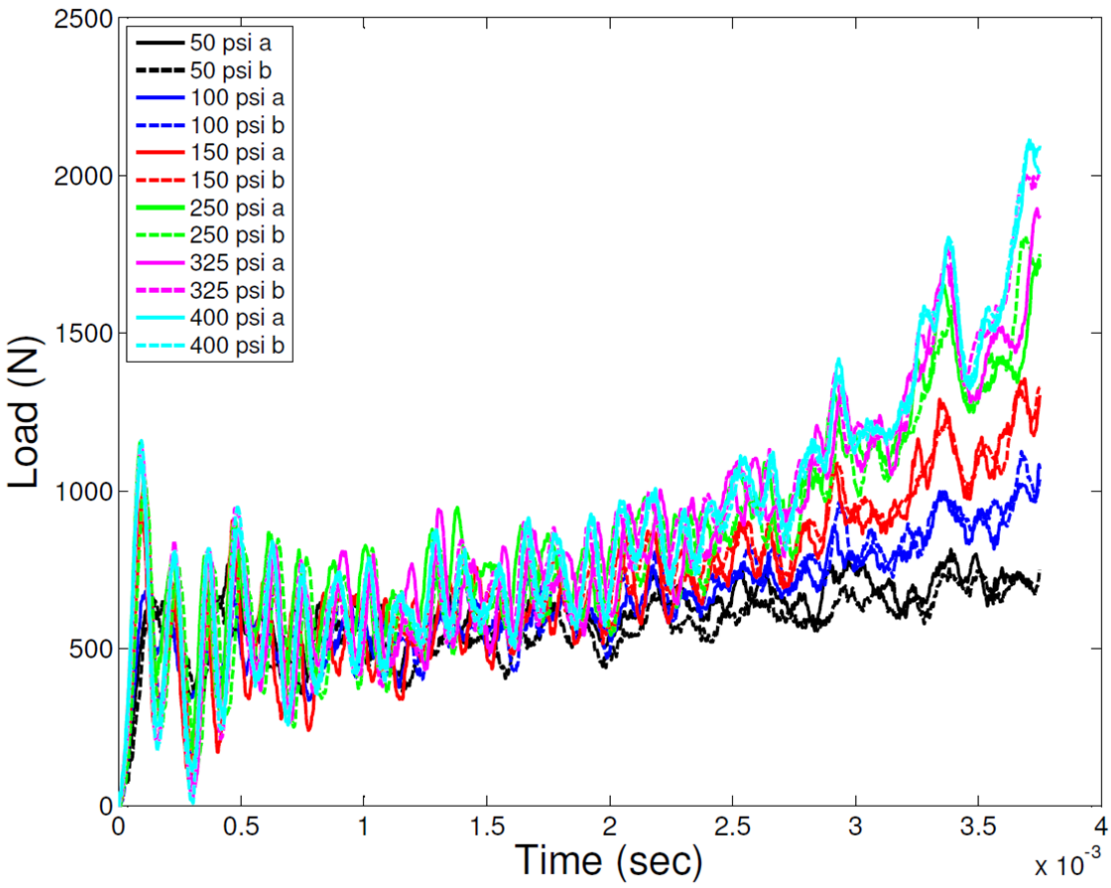

Figure 6.5: Load vs. time data for the crushing of 19-cell filled specimens using the WLD technique.

6.4 Crush Experiment

The variation of load as a function of time for 19-cell filled specimens is shown in Figure 6.5. Initially, there is a linear regime which is dominated by the honeycomb response. There is a transition at 0.1 ms into a plateau nearly up to 2 ms. After this, the response stiffens because the hardening polymer response dominates. Unlike the axial static crushing of filled honeycombs encountered in Chapter V, there are oscillations in the load signal because of the dynamic nature of loading.

High speed images of the experiment corresponding to firing pressures of 100 psi and 400 psi are shown in Figures 6.7 and 6.8 respectively. When the incident bar

impacts the specimen during its first ramp motion, the polymer surrounding the honeycomb at the impacted end is seen to deform radially over a short segment. The amplitude rapidly decays along the length of the specimen. This behavior is seen in snapshot #2 in each of these figures. Since the elastic modulus of the soft polyurethane elastomer is low (in the range of $0.2 - 0.3$ MPa), the wave speed in this material is approximately 1.5×10^4 mm/s, which is about 90 times slower than the wave speed in polycarbonate. Based on this estimate, it takes about 1.6 ms for the axial stress waves in the polyurethane to reach the fixed end. The localized deformation in polyurethane will be in the results from finite element simulations presented later in this chapter. During the rest phase of the incident bar, the specimen exhibits a free vibration response in the axial as well as in the radial direction. Longitudinal tearing is observed in the cell walls as crushing progresses. This is visible in snapshots #4 to #9 in Figures 6.7 and 6.8. Excessive barreling is seen towards the final stages of crushing as can be seen in the final snapshots in the two aforementioned figures. The deformed shaped of the crushed samples retain some residual barreling. Figure 6.6 shows a deformed specimen in contrast to a specimen from a quasi-static test. Here, the dynamic mode of folding is quite similar to the static as can be seen in the images. However, the residual barreling is not seen in the specimen subjected to quasi-static loading. Under static loading, the average crush load is approximately 375 N whereas the peak load is in the range of $390 - 500$ N.

Since the loading does not occur at a uniform rate, the rate dependency can be compared against the estimates of the maximum and average crush velocities. Figure 6.10 shows the variation of the peak load as a function of the maximum velocity, which occurs during the first ramp cycle. It is seen that the peak load increases with increase in the maximum impact velocity. The energy absorbed normalized by the length L of the specimen during crushing as a function of maximum and average crush velocities is also calculated as shown in Figures 6.11 and 6.12 respectively. Note that

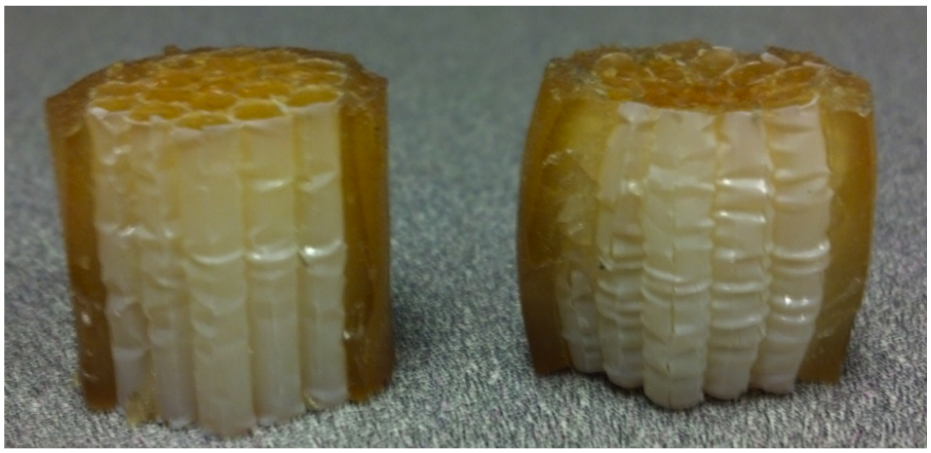

Figure 6.6: Deformed specimens from the static test (left) and dynamic test (right). Notice the residual barreling in the specimen subjected to dynamic loading.

energy absorbed per unit length is equivalent to a mean plateau load value. In the above three plots, the static values are plotted corresponding to maximum/average velocity of 0 mm/s. The variation of normalized energy absorbed is somewhat linear for the range of crush velocities attained in the WLD device. These observations strongly point to rate dependency in these specimens.

The high rate crushing of polyurethane blocks using the WLD method serves no purpose in the present investigation. High rate testing of soft materials is a challenge because low wave speeds in the material delay equilibration of stresses in the soft polyurethane sample. That is, upon impact, two distinct regions develop in the sample (I) a narrow stressed (and simultaneously deformed) zone that propagates from the impacted end with low speed, (II) a stress free zone (and undeformed) in the remaining portion of the sample. Unlike stiff materials such as metals, in which three reflections within the specimen are usually sufficient for stress equilibration, a soft material like polyurethane would require several rounds of reflections within the specimen before stresses equilibrate in the sample. The signal registered when the stress wave reaches the force sensor can be thought of as that measuring the structural response of the polymer sample rather than material response. This problem can

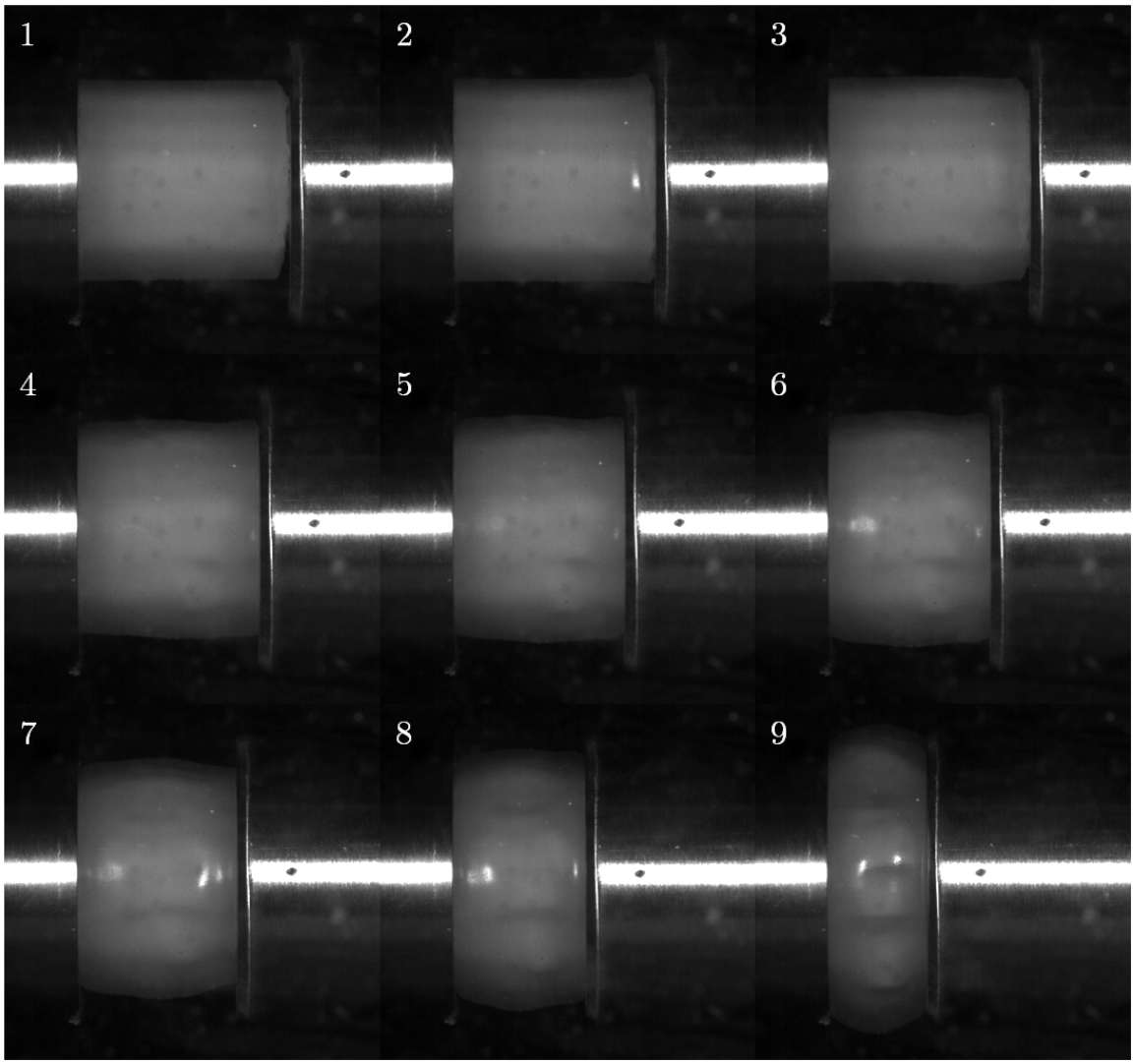

Figure 6.7: High speed images from the experiment (with 100 psi firing pressure) corresponding to time points after impact (1) 0 ms, (2) 0.2 ms, (3) 0.4 ms, (4) 1 ms, (5) 1.4 ms, (6) 1.8 ms, (7) 2 ms, (8) 3 ms, (9) 4.5 ms. Impact occurs from the right side of the specimen.

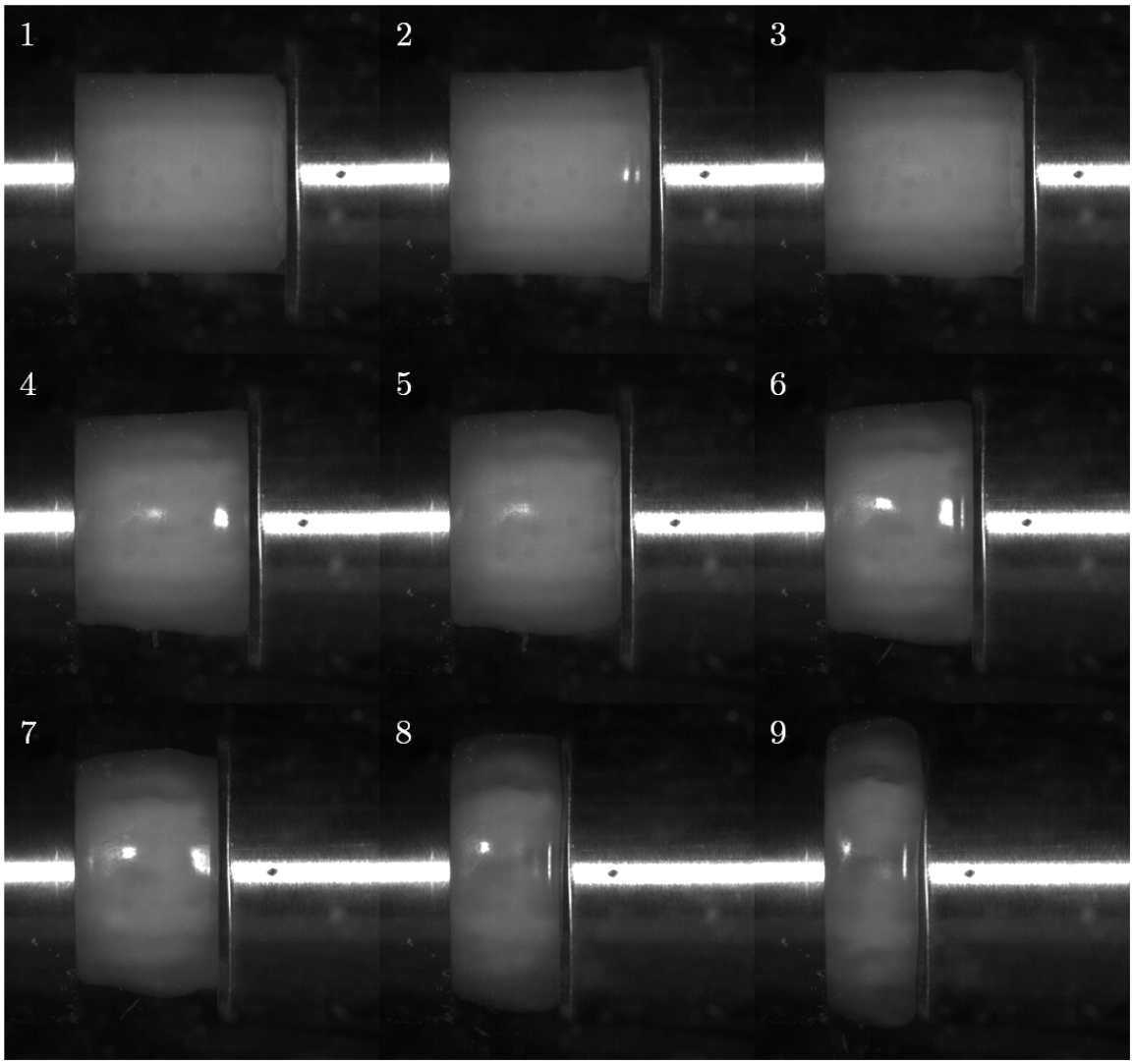

Figure 6.8: High speed images from the experiment (with 400 psi firing pressure) corresponding to time points after impact (1) 0 ms, (2) 0.2 ms, (3) 0.4 ms, (4) 1 ms, (5) 1.2 ms, (6) 1.8 ms, (7) 2 ms, (8) 3 ms, (9) 3.5 ms. Impact occurs from the right side of the specimen.

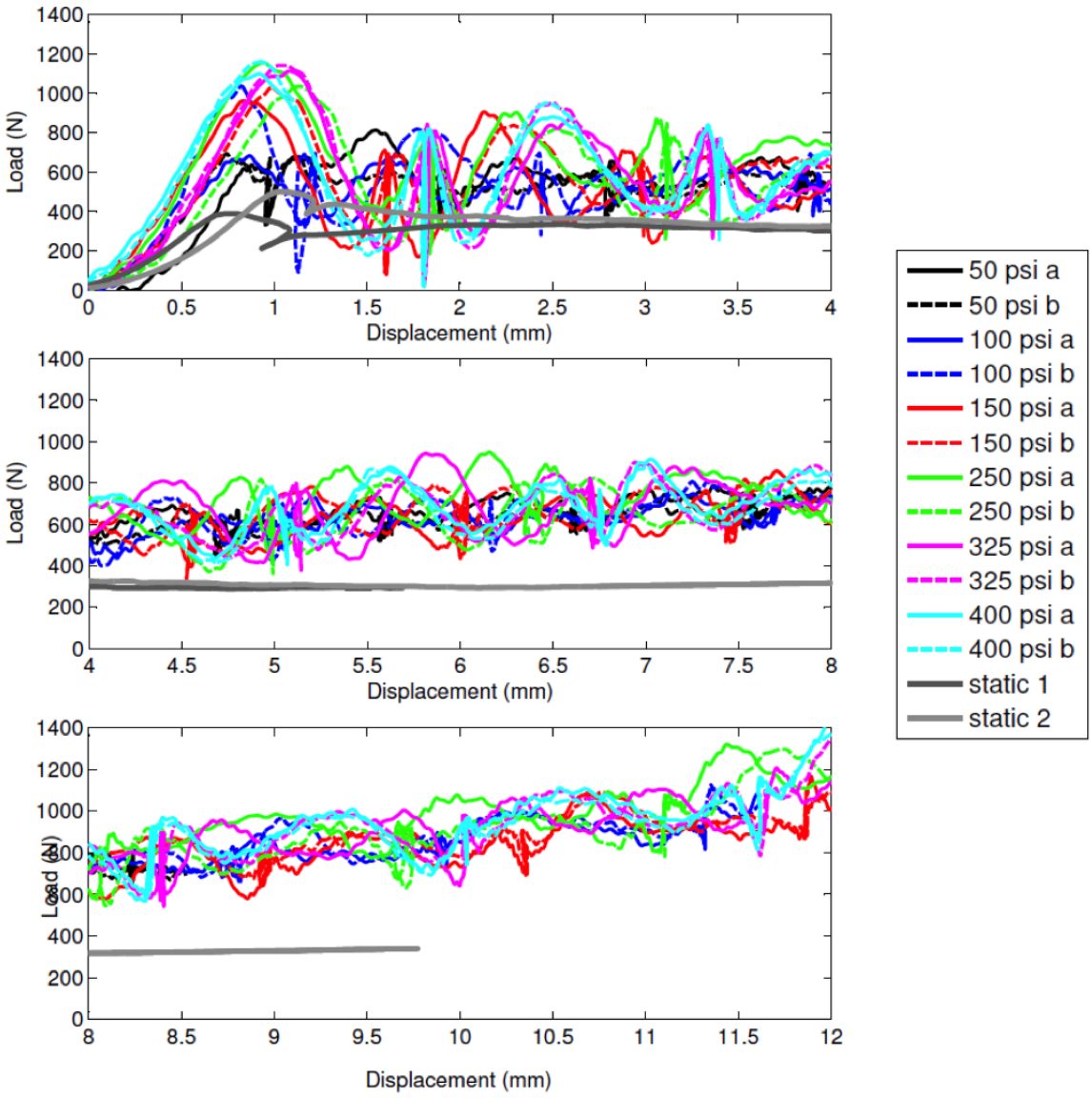

Figure 6.9: Load vs. displacement response for various firing pressures. Static crush response is also shown.

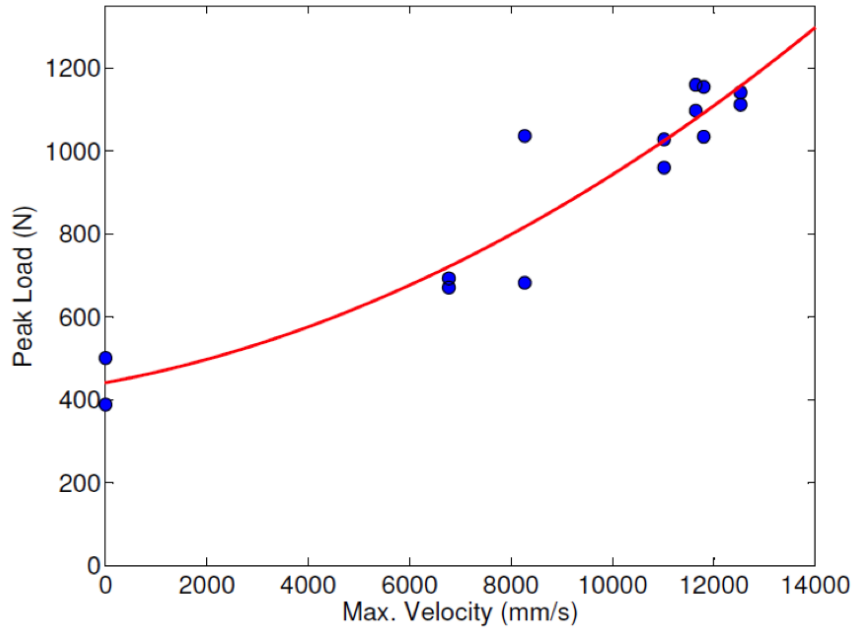

Figure 6.10: Peak load as a function of the maximum crush velocity

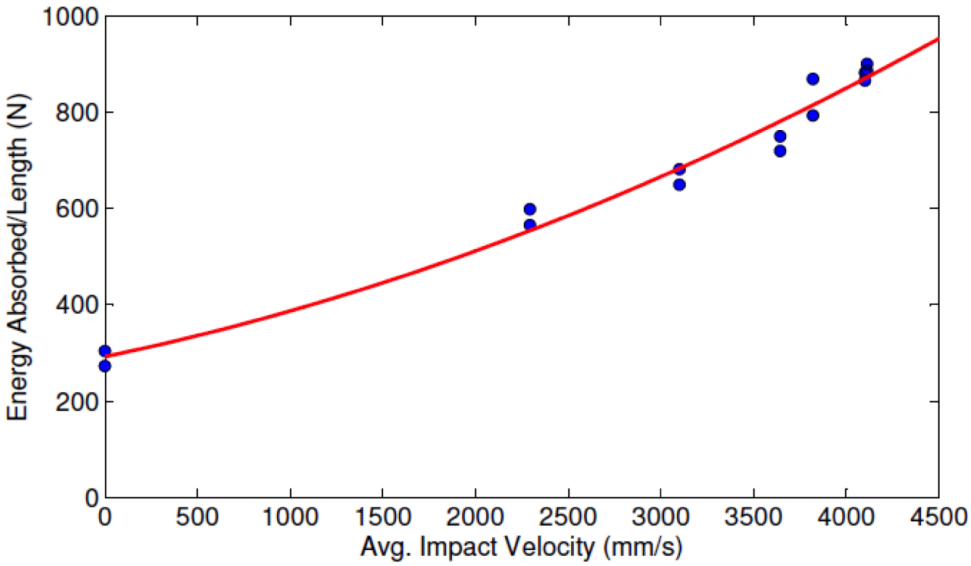

Figure 6.11: Energy per unit crush distance as a function of average crush velocity

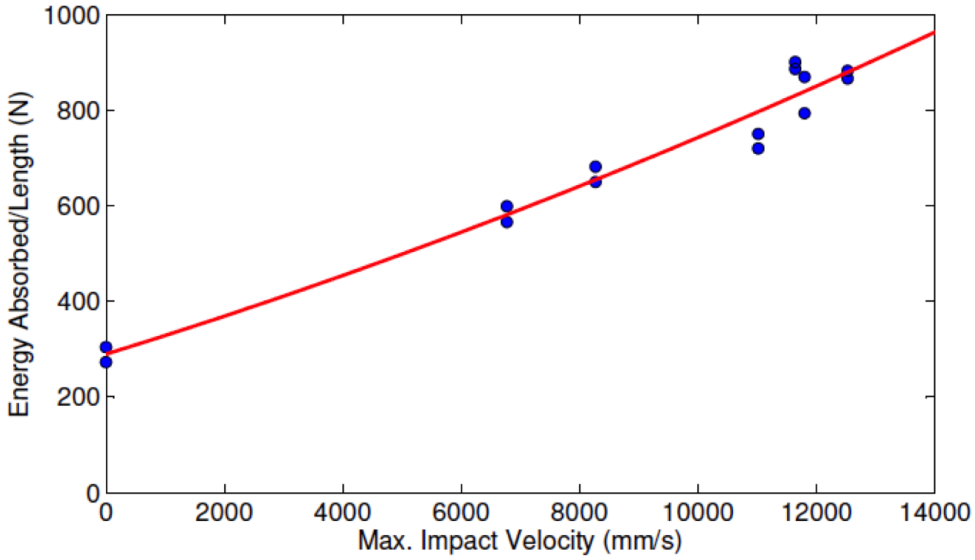

Figure 6.12: Energy per unit crush distance as a function of maximum crush velocity

be partially resolved at lower loading rates by using Dynamic Mechanical Analysis (DMA), which is discussed later.

6.5 Modeling Polyurethane Response

The rate dependent behavior of the polyurethane filler is studied here. This is important because the rate dependency in the experimental results reported in this chapter is influenced by the large deformation and rate dependent response of polyurethane. Since elastomers such as polyurethane exhibit viscoelastic behavior, their 3D constitutive behavior must be characterized. Specifically, the visco-hyperelastic behavior must be understood since viscoelasticity is coupled with finite deformation behavior. A more accurate description of polyurethane would be that of a finite strain viscoplastic solid because of residual strains seen in the dynamic crushing of a few polyurethane specimens using the WLD test. However, for simplicity,

the plasticity effects are neglected in the present investigation. The model chosen to characterize polyurethane in this study is the one proposed recently by Sain et al. (2013). This model's schematic representation is shown in Figure 6.13.

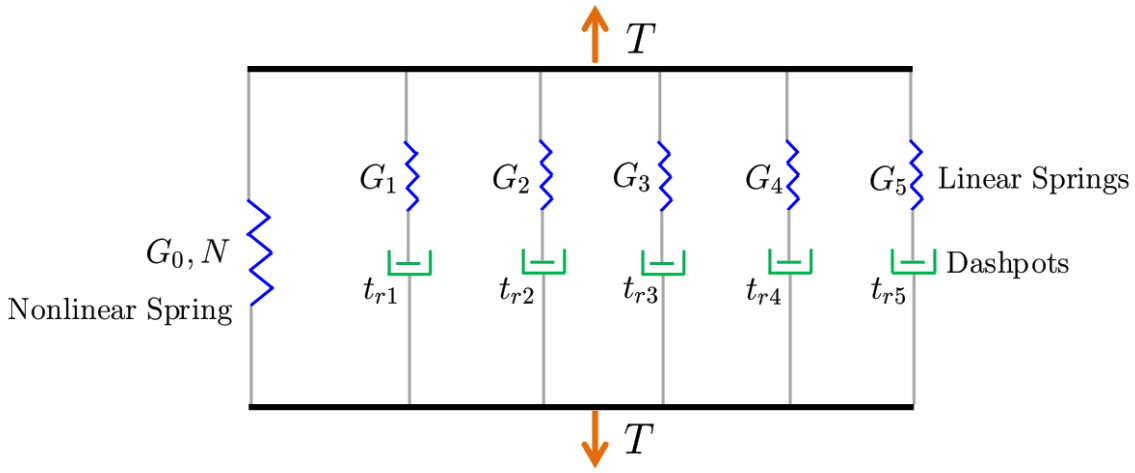

Figure 6.13: Schematic representation of a 3D finite strain viscoelastic model proposed by Sain et al. (2013) that is subjected to Cauchy stress **T**. Shown here is a model with a nonlinear spring and five Maxwell branches.

The left branch consists of a nonlinear spring which could, in theory, be any hyperlelastic model such as Neo-Hookean, Odgen, Yeoh and the like. A concise review of several such models is provided by Boyce & Arruda (2000). In the present study, the 8-chain model (Arruda & Boyce (1993)) is used to model the nonlinear spring with unknown constants $G_0 = nk\theta$ and N, which are respectively the initial shear modulus and the square of the limiting stretch of each chain in the polymer. This model depends only on the first stretch invariant I_1, which dominates the contribution to the strain energy of soft elastomers such as polyurethane. This spring captures the large strain response of the elastomer. The nonlinear spring is in series with several branches consisting of a linear spring (Hookean) and a dashpot, which are essentially the Maxwell elements. These elements capture the viscoelastic part of the response. This model is similar to that by Boyce et al. (1988), which was used to characterize

rate dependent response of glassy polymers. Here, k is the Boltzmann constant, θ is the absolute temperature taken to be room temperature and n is the chain density, which is defined as the number of molecular chains per unit reference volume. The strain energy density function of the 8-chain model is

$$\mathcal{U} = nk\theta N \left\{ \left(\frac{\lambda_{ch}}{\sqrt{N}} \right) + ln \left(\frac{\beta_{ch}}{\sinh(\beta_{ch})} \right) - \left(\frac{\beta_0}{\sqrt{N}} \right) - ln \left(\frac{\beta_0}{\sinh(\beta_0)} \right) \right\} \tag{6.2}$$

where $\beta_{ch} = \mathcal{L}^{-1}(\lambda_{ch}/\sqrt{N})$ and $\beta_0 = \mathcal{L}^{-1}(1/\sqrt{N})$. Here, $\mathcal{L}^{-1}$ is the inverse Langevin function which can be written using Padé approximation (Cohen (1991)) as

$$\mathcal{L}^{-1}(x) = x \left(\frac{3 - x^2}{1 - x^2} \right) \tag{6.3}$$

The inverse Langevin term arises due to the non-Gaussian statistics of the polymer chains, which predicts the nonlinear dependence of force on the polymer chain length.

In Equation 6.2, λ_{ch} is the stretch on each chain in the polymer network and is defined as $\lambda_{ch} = \sqrt{I_1/3}$ where I_1 is the first invariant of $\mathbf{B}$, the right Cauchy Green strain tensor. This can be written in terms of the deformation gradient $\mathbf{F}$ as $\mathbf{B} = \mathbf{F}\mathbf{F}^T$. For uniaxial compression, assuming incompressibility, the deformation gradient is

$$\mathbf{F} = \begin{pmatrix} \lambda & 0 & 0 \\ 0 & \frac{1}{\sqrt{\lambda}} & 0 \\ 0 & 0 & \frac{1}{\sqrt{\lambda}} \end{pmatrix} \tag{6.4}$$

Then, λ_{ch} can be written in terms of stretch as

$$\lambda_{ch} = \sqrt{\frac{1}{3} \left(\lambda^2 + \frac{2}{\lambda} \right)} \tag{6.5}$$

The 8-chain model is an I_1 based model. Then, the expression for the Cauchy stress

is obtained by differentiating the strain energy density function as

$$\mathbf{T} = 2\frac{\partial \mathcal{U}}{\partial I_1} - p^*\mathbf{I} \tag{6.6}$$

where p^* is the indeterminate pressure required to ensure incompressibility and can be obtained by satisfying the boundary conditions. Upon manipulation, the above equation takes the form

$$\mathbf{T} = \frac{nk\theta}{3}\left(\frac{\sqrt{N}}{\lambda_{ch}}\right)\mathcal{L}^{-1}\left(\frac{\lambda_{ch}}{\sqrt{N}}\right)\mathbf{B} - p^*\mathbf{I} \tag{6.7}$$

Specializing the above equation for uniaxial loading condition by making use of deformation gradient in Equation 6.4, we obtain the Cauchy stress T_1 along the loading direction

$$T_1 = \frac{nk\theta}{3}\left(\frac{\sqrt{N}}{\lambda_{ch}}\right)\mathcal{L}^{-1}\left(\frac{\lambda_{ch}}{\sqrt{N}}\right)\left(\lambda^2 - \frac{1}{\lambda}\right) \tag{6.8}$$

To characterize the nonlinear spring constants G_0 and N, the polyurethane sample is subjected to uniaxial static compression. Then, the constants are obtained by least square fit with the nominal stress (T_{01}) expression of the 8-chain, which is

$$T_{01} = \frac{nk\theta}{3}\left(\frac{\sqrt{N}}{\lambda_{ch}}\right)\mathcal{L}^{-1}\left(\frac{\lambda_{ch}}{\sqrt{N}}\right)\left(\lambda - \frac{1}{\lambda^2}\right) \tag{6.9}$$

The nominal stress expression is used because nominal quantities are easily obtained from the experiment to enable a fit. The fit is got using nonlinear regression option in MATLAB. For the present polyurethane specimen, $G_0 = 0.0876$ MPa and $\sqrt{N} = 965$ for the nominal strain values between 0 and 0.48 (i.e. between $0.52 \leq \lambda \leq 1$). The experimental plot and nominal stress vs. strain using the values from the fit is shown in Figure 6.14. At this point, the nonlinear spring is fully characterized.

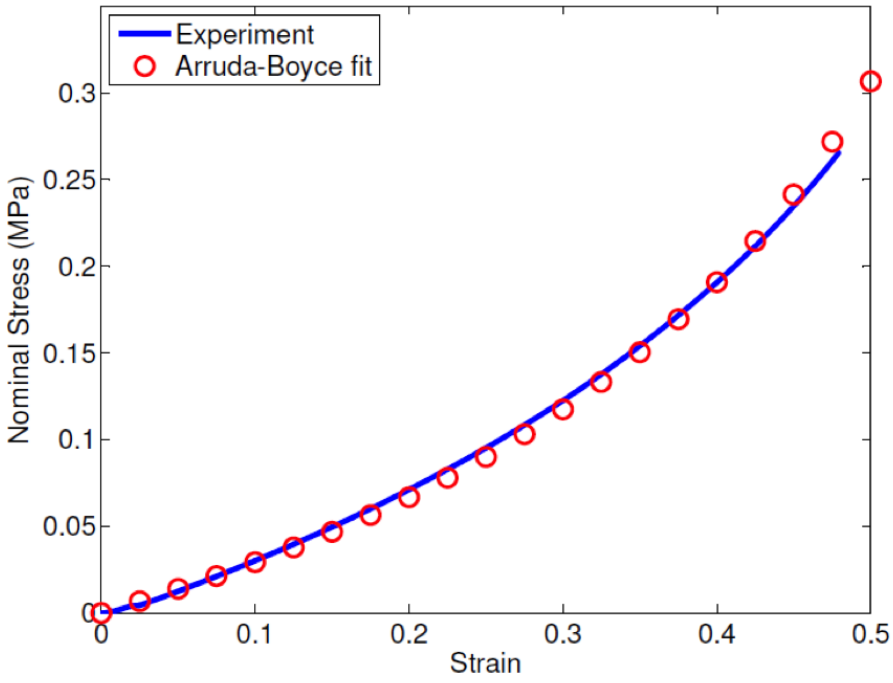

Figure 6.14: Calibration of the Arruda-Boyce 8-chain model with nominal compression stress-strain data for polyurethane.

Next, the Maxwell elements of the model shown in Figure 6.13 are identified. This viscoelastic response can be obtained using Prony series for the complex shear modulus $G^*(\omega)$ and the complex bulk modulus $K^*(\omega)$ were the subscript $*$ denotes a complex number and ω is the frequency of strain oscillation. These can be written in the frequency domain as

$$G^*(\omega) = G_0 + \sum_{i=1}^{N_b} \left(\frac{G_i \mathcal{I} \omega \tau_i}{1 + \mathcal{I} \omega \tau_i} \right) \tag{6.10}$$

$$K^*(\omega) = K_0 + \sum_{i=1}^{N_b} \left(\frac{K_i \mathcal{I} \omega \tau_i}{1 + \mathcal{I} \omega \tau_i} \right) \tag{6.11}$$

where N_b is the number of Maxwell elements and $\mathcal{I}$ denotes $\sqrt{-1}$. Here, G_i and K_i are the shear and bulk moduli of the linear springs for $i = 1....N_b$. Without loss of generality, the Poisson's ratio of each linear spring was taken to be equal to 0.25 so

that $K_i = 5G_i/3$. Also, G_0 is the initial stiffness of the nonlinear spring) which was characterized in the previous step. Notice that $G^* = G_0$ at $\omega = 0$, which corresponds to the static forcing condition. For an incompressible material, the bulk modulus $K \to \infty$. However, to ensure numerical stability when implementing hyperelasticity in ABAQUS/Explicit, the Poisson's ratio (ν) must be slightly less than 0.5 because the program has no mechanism for enforcing incompressibility constraint at each integration point. Recommended (Simulia (2011)) range is $0.49 \leq \nu < 0.49995$. Using Poisson's ratio of $\nu = 0.49$, the bulk modulus K_0 equals 4.35 MPa.

Dynamic Mechanical Analysis (DMA) is used to obtain viscoelastic properties of the polyurethane sample. In DMA, thin strips of polyurethane are pre-stretched and then subjected to sinusoidal strain input. This test gives frequency dependent complex Young's modulus $E^*(\omega)$ and $\tan(\delta)$, which is the viscoelastic loss factor. Here, $E^*(\omega)$ can be related to the complex bulk and shear moduli as

$$E^*(\omega) = \frac{9K^*(\omega)G^*(\omega)}{3K^*(\omega) + G^*(\omega)} \tag{6.12}$$

The experimental data for the loss factor and storage modulus is shown in Figure 6.15. The range of frequencies available on the test setup was between 5 to 100 Hz. It was seen that the test data had massive scatter at frequencies above 50 Hz onward, with the scatter progressively getting worse with further increase in the loading frequency. The scatter is caused due to low wave speed in the polyurethane material. For low frequencies, the stresses have enough time to equilibrate along the length. However, at higher frequencies, the specimen is in a state of dynamic non-equilibrium leading to a wider scatter in the measured data. In the present analysis, the data in the range 1 Hz $\leq \omega <$ 50 Hz only are considered. Using Equation 6.11, the loss

i	1	2	3	4	5
t_{ri} (sec)	54.42	0.1818	0.2163	0.00208	0.00015
G_i	3.85×10^{-12}	0.0084	0.02	0.0372	0.0933

Table 6.1: Material parameters for the five Maxwell elements to model polyurethane

modulus can be written as

$$\tan(\delta) = \frac{\text{Img}(G^*(\omega))}{\text{Re}(G^*(\omega))} \tag{6.13}$$

where G_0 had been found from the uniaxial compression test.

A nonlinear least squares fit is conducted using the experimental measurement of $\tan(\delta)$ and Equation 6.13 for a given number Maxwell elements N_b. It is seen that $N_b = 5$ gave the best agreement with the experimentally measured $\tan(\delta)$ response. Taking the optimized values of the shear moduli of the i^{th} spring G_i and time constant of the i^{th} dashpot t_{ri}, a prediction with the experimentally obtained storage modulus was performed. The values of t_{ri} and G_i are provided in Table 6.1.

Along with the DMA data, Figure 6.15 also shows the fit with $\tan(\delta)$ and the prediction of the storage modulus. The $\tan(\delta)$ fit and prediction storage modulus agree well with the corresponding experimental values well, especially in the range 1 Hz $\leq \omega <$ 20 Hz. For $\omega >$ 50 Hz, the material behavior is assumed to obey the fit. Note that this is a significant assumption which arises due to the inability to accurately model the behavior of the material owing to its low wave speed.

6.6 Finite Element Simulations

The objective of the finite element study is to simulate the high rate crushing of the 19-cell filled honeycomb. Similar to the filled honeycomb model presented in Chapter V, a 19-cell filled model is constructed in ABAQUS/CAE with honeycomb modeled using shell elements and the polymer modeled using a combination of 6-noded and 8-noded solid elements (Figure 6.16). In the dynamic crush simulations,

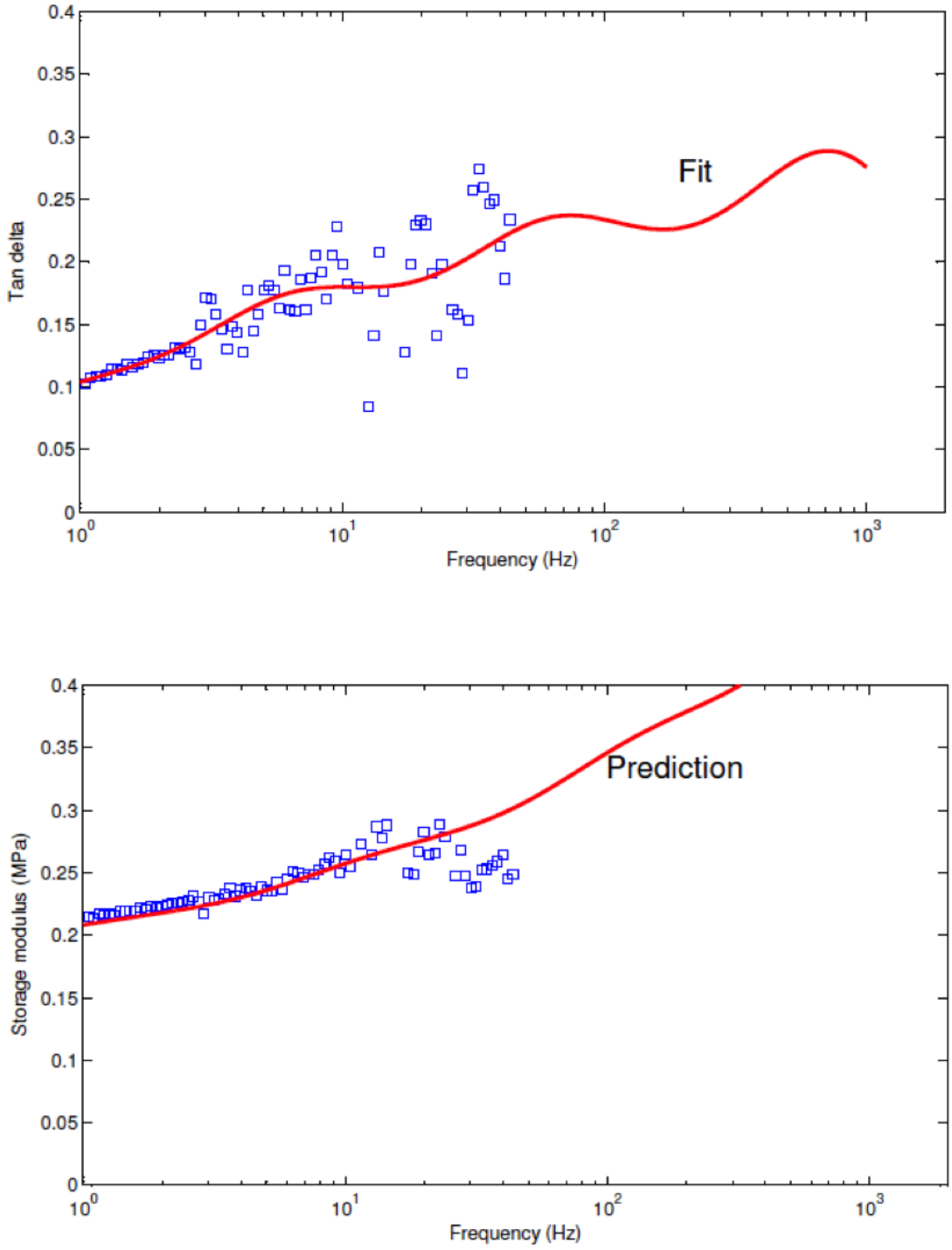

Figure 6.15: The DMA data from the experiment is shown in blue: Loss factor tan(δ) is shown at the top and the storage modulus is shown at the bottom. The curve fit for tan(δ) and storage modulus prediction are shown in red.

displacement information from experiments with 50 psi and 250 psi firing pressures are chosen. The constitutive model for polyurethane is implemented using an ABAQUS user subroutine VUMAT. To trigger instabilities in these simulations, the honeycomb mesh is seeded with the first two eigenmodes with imperfection amplitude of 50% of the wall thickness. For the polycarbonate wall material, the rate dependent properties in Mulliken & Boyce (2006) are used.

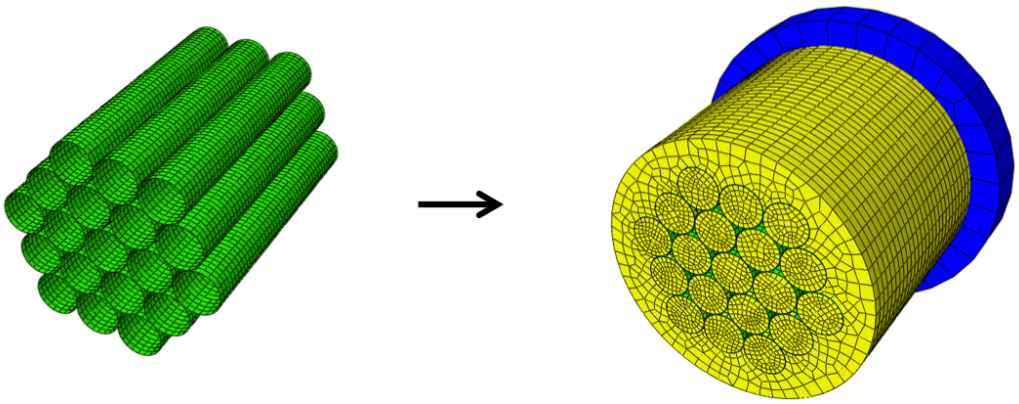

Figure 6.16: Finite element model of the 19-cell honeycomb which is embedded in the solid (right)

The input to each of two models is the displacement vs. time data that was measurement from the experiment (i.e. motion of the incident bar). Once the model is loaded, the progression of axial stress wave in the honeycomb and in the polymer is shown in Figure 6.17 at various time instances. Here, it is seen that due to low wave speeds in the polymer, the deformation in the polymer is concentrated in a narrow zone. Hence, the loads that are initially measured at the back end of the specimen are primarily due to the constrained honeycomb. However, the rate effect of the polymer comes into play when the honeycomb walls begin to collapse. That is, in the polymer, even though the axial wave propagated from the impacted end has not yet travelled over most of the specimen's length, the polymer surrounding the wall material gets loaded when the honeycomb starts to fold. Hence, it is expected that constraint placed on the honeycomb walls during folding is influenced by the rate dependent

behavior in the surrounding polymer. The comparison between the finite element simulations and experiment is shown in Figure 6.18. The comparison between quasi-static experiment and its corresponding simulation is also shown in that plot. Load elevation is seen in the simulation corresponding to 250 psi when compared to the case of 50 psi. This suggests that the load response simulated using finite elements exhibits rate dependent behavior. Overall, the simulated load response is close to that from the experiment. The simulated fold pattern is shown in Figure 6.19, which again is similar that obtained from the experiment shown in Figure 6.19.

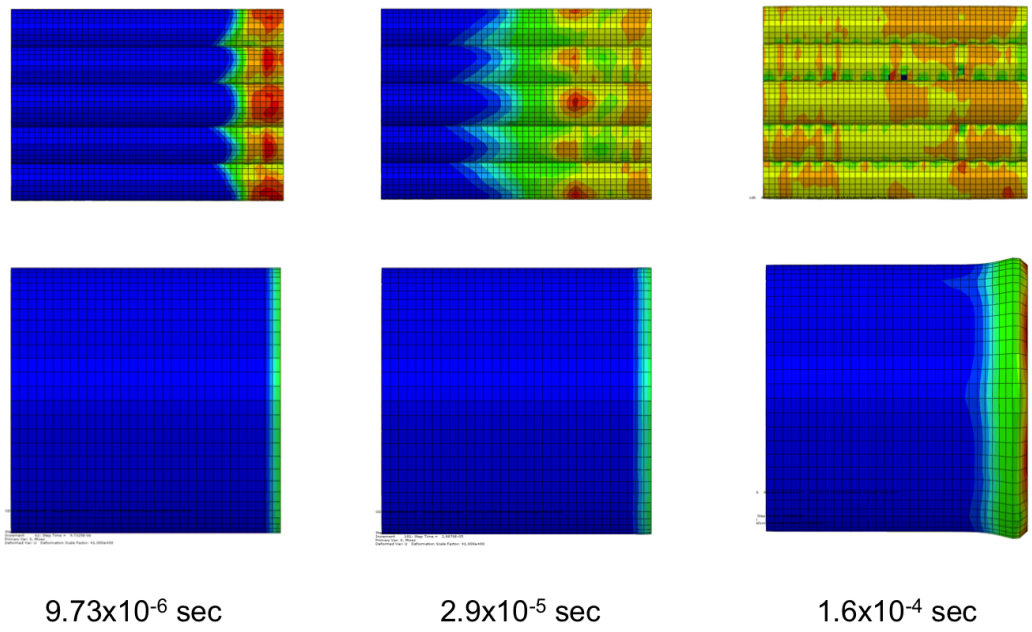

Figure 6.17: Extent of wave propagation in the honeycomb and in the polymer in the axial direction.

6.7 Conclusions

In this chapter, the high rate axial crushing of 19-cell filled honeycombs was presented. The filler material used in the study was polyurethane. High rate experiments using the wave loading device (WLD) revealed the presence of rate dependent crush behavior in these specimens. The behavior of polyurethane filler was characterized

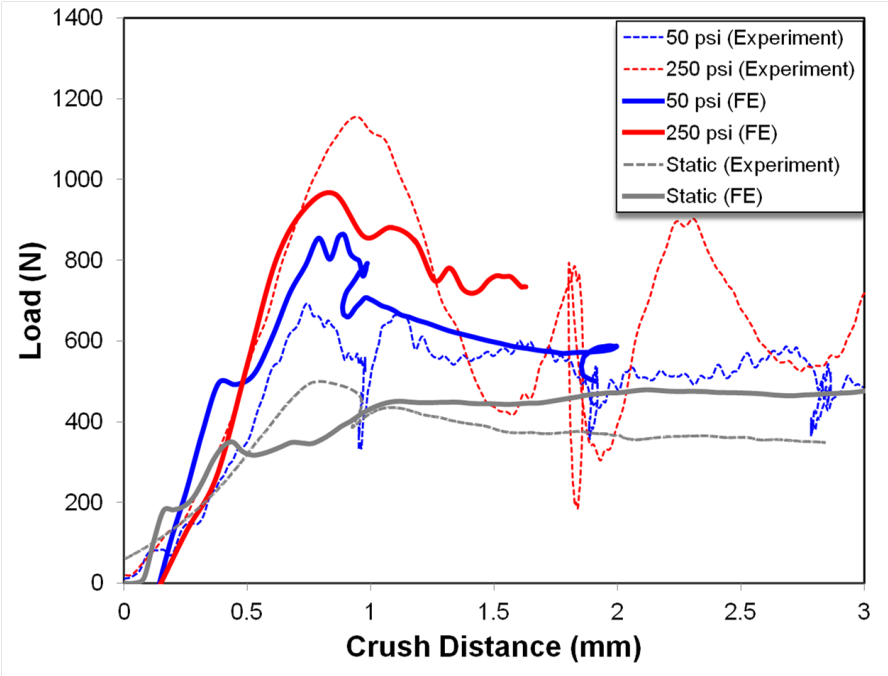

Figure 6.18: Comparison between simulation and experiment under dynamic (WLD) and static loading.

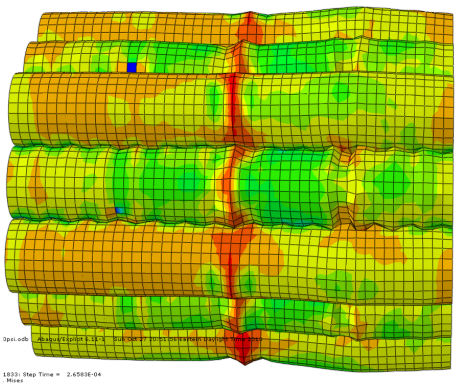

Figure 6.19: Diffused collapse mode in the honeycomb walls obtained from WLD simulation

using the dynamic mechanical analysis (DMA) test and modeled using a large strain viscoelastic material model. The simulations performed using ABAQUS/Explicit were in fair agreement with experimental load response in terms of overall load response. Also, the diffused mode of deformation was captured in the dynamic crush simulations.

CHAPTER VII

Conclusions and Future Work

In this dissertation, the compressive response of circular cell polycarbonate honeycomb was studied. The inplane crush response was revisited and an approximate method to determine the plateau load which provided remarkably accurate prediction of the plateau load was presented. Next, the high rate response in the out-of-plane (axial) direction was studied. Two experimental methods were conceived to perform crush experiments - Wave Loading Device (WLD) and the Direct Impact Method (DIM). It was seen that the crush load increases with the crush velocity. The mode of deformation was concertina-diamond folding, which is also similar to the mode of crushing under quasi-static condition. A minor difference in the dynamic crushing is that folding can sometimes initiate at both ends.

The response of filled honeycomb was investigated. First, the inplane crushing of a 11×11 size honeycomb filled with PDMS elastomer was studied. It was seen that due to constraint of the filler in each of the cells, the first load to failure was much higher than what is seen in the unfilled experiment. Hence, a synergy in the load response is observed and is attributed to the biaxial state of stress in the filler material as revealed by both the Digitial Image Correlation (DIC) analysis and also finite element analysis. The energy dissipation mechanism is controlled by Mode I longitudinal fracturing of cell walls which triggers localization, which then propagates somewhat erratically to

the rest of the structure. Consequently, a new energy dissipation mechanism was reported where dissipation occurs along with some storage in the filler material.

The out-of-plane crushing of filled circular cell honeycombs also leads to synergy in the crush load. Polyurethane filler was used in this study. This synergy is due to the change of mode from localized to diffused mode because the filler material stabilizes folding. To the cell walls, the filler acts as a hardening foundation. Moreover, unlike a sharp drop seen in shells, there is only a marginal drop in the presence of the filler material, which is desirable for energy absorption applications. The high rate crushing of this filled honeycomb system was studied in another wave loading device. Rate dependency observed here was due to the viscoelasticity in the polyurethane filler, which was characterized by Dynamic Mechanical Analysis (DMA) tests. Again, the folding pattern is diffused like in the quasi-static case, but the critical feature of the dynamic response are elevated loads compared to the quasi-static response.

The following are some directions for future work with some strategies:

- It is of interest to examine how honeycombs behave when loaded at rates that are comparable to the wave speed in honeycomb wall. Motivated by the experimental results of Gladden et al. (2005) on the dynamic buckling of impacted rods, Ji & Waas (2008) proposed the notion of critical time to buckle t^* which is analogous to the critical load P_{cr} in static Euler buckling. Essentially, Ji & Waas (2008) showed that at t^*, the beam can buckle even though the stress wave has not traversed the entire length L. That is, t^* can be less than L/c where c is the wave speed in the material. To understand such a phenomenon in honeycombs, the axial response of a thin cylindrical shell can be first studied to extract t^* as a function of the impacting mass M and the velocity of impact V, where V is of the same order of magnitude as the wave speed in the cylinder.

Since the non-axisymmetric shell buckling equations are formidable, a starting point could be the use of axisymmetric shell equation[1] coupled with the wave equation along the shell's axial direction.

- It was shown in this dissertation that mode of folding controls the crush load. Most of the cells have uniform thickness. A natural question is the following: Is it possible to design cell walls such that it would absorb the highest amount of energy for some prescribed weight? Addressing this question would require coupling optimization concepts and finite element analysis. The designs can then be verified by experiment. A major bottleneck here are the constraints posed by manufacturing. It is expected that with further advancement in 3D printing technology, it would be possible to print prototypes with a wider range of materials to validate optimal cell designs.

- The introduction of the elastomeric filler material in the honeycomb stabilizes the first collapse event. It would be interesting to extend Koiter's asymptotic analysis (Koiter (1945)) with a foundation term to analytically study the transition from unstable to stable collapse (by examining the initial post-buckling path) with change in filler properties. In other words, for a given shell of certain dimensions and modulus of elasticity, what is the relative filler stiffness required to ensure stable collapse? An associated question to ask is: What is the imperfection sensitivity of a cylindrical shell in the presence of elastomeric foundation? It may be feasible to extend Koiter's analysis of imperfect shells (Koiter (1963)) to answer the question by introducing a foundation term. It is likely that the foundation terms for the aforementioned analyses may be approximated as linear. This is motivated by ease in solving the imperfect shell equation with such an approximation and because the finite element paramet-

[1]Mathematically, the axisymmetric shell equation is similar to that of a beam on an elastic foundation

ric study in Chapter V suggested that the highly nonlinear hardening response comes into play only after the fold formation has started.

BIBLIOGRAPHY

BIBLIOGRAPHY

Arbocz, J. (1987). Post-buckling behavior of structures: Numerical techniques for more complicated structures. *Lecture Notes in Physics*, 84 - 142.

Arruda, E. M., & Boyce, M. C. (1993). A three-dimensional constitutive model for the large stretch behavior of rubber elastic materials. *Journal of the Mechanics and Physics of Solids*, *41*, 389-412.

Ashby, M. F. (1983). The mechanical properties of cellular solids. *Metallurgical Transactions A*, *14*(9), 1775-1769.

Babcock, C. D. (1983). Shell stability. *ASME Journal of Applied Mechanics*, *50*, 935-940.

Baker, W. E., Togami, T. C., & Weydert, J. C. (1998). Static and dynamic properties of high density metal honeycombs. *International Journal of Impact Engineering*, *21*(3), 149-163.

Bažant, Z. P., & Cedolin, L. (1991). *Stability of structures: Elastic, inelastic, fracture and damage theories*. New York, Oxford: Oxford University Press.

Bažant, Z. P., & Oh, B. (1983). Crack band theory for fracture of concrete. *Materials and Structures*, *16*, 155-177.

Boyce, M. C., & Arruda, E. M. (2000). Constitutive models of rubber elasticity: A review. *Rubber Chemistry and Technology*, *73*(3), 504-523.

Boyce, M. C., Parks, D. M., & Argon, A. S. (1988). Large inelastic deformation of glassy polymers, part i: Rate dependent constitutive model. *Mechanics of Materials*, *7*, 15-33.

Brush, D. O., & Almroth, B. O. (1975). *Buckling of bars, plates and shells*. McGraw-Hill, New York.

Carlsson, L. A., & Kardomateas, G. A. (2011). *Structural and failure mechanics of sandwich composites*. Springer.

Chen, D. H. (2011). Equivalent flexural and torsional rigidity of hexagonal honeycomb. *Composite Structures*, *93*(7), 1910-1917.

Chung, J. (2000). *Inplane compressive response and failure of circular cell honeycomb.* Unpublished doctoral dissertation, University of Michigan - Ann Arbor.

Chung, J., & Waas, A. M. (1999). Compressive response and failure of circular cell polycarbonate honeycombs under inplane uniaxial stresses. *Journal of Engineering Materials and Technology*, *121*(4), 494-502.

Chung, J., & Waas, A. M. (2002). Elastic imperfection sensitivity of hexagonally packed circular–cell honeycombs. *Proceedings of the Royal Society of London. Series A: Mathematical, Physical and Engineering Sciences*, *458*(2028), 2851-2868.

Chung, J., & Waas, A. M. (2002a). Compressive response of circular cell polycarbonate honeycombs under inplane biaxial static and dynamic loading - part i: experiments. *International Journal of Impact Engineering*, *27*(7), 729-754.

Chung, J., & Waas, A. M. (2002b). Compressive response of circular cell polycarbonate honeycombs under inplane biaxial static and dynamic loading - part ii: simulations. *International Journal of Impact Engineering*, *27*(10), 1015-1047.

Chung, J., & Waas, A. M. (2009). The micropolar elasticity constants of circular cell honeycombs. *Proceedings of the Royal Society A: Mathematical, Physical and Engineering Science*, *465*(2101), 25-39.

Cohen, A. (1991). Pade approximation to the inverse langevin function. *Rheologica Acta*, *30*, 270-273.

Daly, S. (2010). Digital image correlation in experimental mechanics for aerospace materials and structures. *Encyclopedia of Aerospace Engineering*.

de Borst, R. (2003). Numerical aspects of cohesive-zone models. *Engineering Fracture Mechanics*, *70*(14), 1743-1757.

D'Mello, R. J., Guntupalli, S., Hansen, L. R., & Waas, A. M. (2012). Dynamic axial crush response of circular honeycombs. *Proceedings of the Royal Society A: Mathematical, Physical and Engineering Sciences*, *468*, 2981-3005.

D'Mello, R. J., & Waas, A. M. (2012). Synergistic energy absorption in the axial crush response of filled circular cell honeycombs. *Composite Structures*, *94*(5), 1669 - 1676.

D'Mello, R. J., & Waas, A. M. (2013). Inplane crush response and energy absorption of circular cell honeycomb filled with elastomer. *Composite Structures*, *106*, 491-501.

Foo, C. C., Chai, G. B., & Seah, L. K. (2007). Mechanical properties of nomex material and nomex honeycomb structure. *Composite Structures*, *80*(4), 588 - 594.

Fratzl, P., & Weinkamer, R. (2007). Nature's hierarchical materials. *Progress in Materials Science*, *52*, 1263-1334.

Gibson, L. J., & Ashby, M. F. (1999). *Cellular solids: structure and properties* (2nd ed.). Cambridge University Press.

Gibson, L. J., Ashby, M. F., Schajer, G. S., & Robertson, C. I. (1982). The mechanics of two-dimensional cellular materials. *Proceedings of the Royal Society of London. A. Mathematical and Physical Sciences*, *382*(1782), 25-42.

Gladden, J. R., Nandzy, N. Z., Belmonte, A., & Villermaux, E. (2005). Dynamic buckling and fragmentation in brittle rods. *Physical Review Letters*, *94*.

Goldsmith, W., & Sackman, J. L. (1992). An experimental study of energy absorption in impact of sandwich plates. *International Journal of Impact Engineering*, *12*, 241-262.

Heimbs, S., Middendorf, P., & Maier, M. (2006). Honeycomb sandwich material modeling for dynamic simulations of aircraft interior components. *9th International LS-DYNA Users Conference*, *20*, 1-13.

Heinrich, C., & Waas, A. M. (2012). *Investigation of progressive damage and fracture in laminated composites using the smeared crack approach.* Honolulu: 53rd AIAA/ASME/ASCE/AHS/ASC Structures, Structural Dynamics and Materials conference, April 23-26.

Hencky, H. (1924). Zur theorie plastischer deformationen und der hierduch im material hervorgerufenen nebenspannungen. *Proceedings of the First International Congress on Applied Mechanics, Delft*.

Hong, S.-T., Pan, J., Tyan, T., & Prasad, P. (2008). Dynamic crush behaviors of aluminum honeycomb specimens under compression dominated inclined loads. *International Journal of Plasticity*, *24*, 89-117.

Hou, B., Ano, A., Adennadher, S., Pattofatto, S., Li, Y. L., & Zhao, H. (2011). Impact behavior of honeycombs under combined shear-compression, part i: Experiments. *International Journal of Solids and Structures*, *48*, 687-697.

Ji, W., & Waas, A. M. (2008). Dynamic bifurcation buckling of an impacted column. *International Journal of Engineering Science*, *46*(10), 958-967.

Klintworth, J. W., & Stronge, W. J. (1988). Elasto-plastic yield limits and deformation laws for transversely crushed honeycombs. *International Journal of Mechanical Sciences*, *30*(3–4), 273 - 292.

Koiter, W. T. (1945). *On the stability of elastic equilibrium.* (in dutch with english summary), Delft University.

Koiter, W. T. (1963). *The effect of axisymmetric imperfections on the buckling of cylindrical shells under axial compression* (Tech. Rep. No. 6-90-63-86). Palo Alto, California: Lockheed Missiles and Space Co.

Lagace, P. A., & Vizzini, A. J. (1988). The sandwich column as a compressive characterization specimen for thin laminates. *ASTM STP 972; 46:14*.

Lin, T.-C., Chen, T.-J., & Huang, J.-S. (2012). In-plane elastic constants and strengths of circular cell honeycombs. *Composites Science and Technology*, *72*(12), 1380 - 1386.

Lin, T.-C., & Huang, J.-S. (2013). In-plane mechanical properties of elliptical cell honeycombs. *Composite Structures*, *104*, 14 - 20.

Lubliner, J. (2008). *Plasticity theory*. Dover Publications.

Masters, I. G., & Evans, K. E. (1996). Models for the elastic deformation of honeycombs. *Composite Structures*, *35*(4), 403-422.

McFarland Jr, R. K. (1964). *The development of metal honeycomb energy absobing elements* (Technical Report No. 32-639). Jet Propulsion Laboratory, California Institute of Technology.

Mellquist, E., & Waas, A. M. (2002). *Size effects in the compressive crushing of honeycombs.* Denver, Colorado: 43rd AIAA/ASME/ASCE/AHS/ASC Structures, Structural Dynamics and Materials conference, April 19-22.

Mellquist, E., & Waas, A. M. (2004). *Size effects in the crushing of honeycomb structures.* Palm Springs, California: 45th AIAA/ASME/ASCE/AHS/ASC Structures, Structural Dynamics and Materials conference, April 19-22.

Mohr, D., & Doyoyo, M. (2006). Large plastic deformation of metallic honeycomb: orthotropic rate-independent constitutive model. *International Journal of Solids and Structures*, *41*, 4435-4456.

Morris, N. (1990). Use of lanczos algorithm in elastic stability. *ASCE Journal of Structural Engineering*, *116*(7), 2049-2054.

Mulliken, A. D., & Boyce, M. C. (2006). Polycarbonate and a polycarbonate-poss nanocomposite at high rates of deformation. *ASME Journal of Engineering Materials and Technology*, *128*, 543-550.

Nadai, A. (1931). *Plasticity: A mechanics of the plastic state of matter*. McGraw-Hill, New York and London.

Ostoja-Starzewski, M. (2008). *Microstructural randomness and scaling in mechanics of materials*. CRC Press.

Papka, S. D. (1998). *In-plane uniaxial and biaxial crushing of a polycarbonate honeycomb*. Unpublished doctoral dissertation, The University of Texas at Austin.

Papka, S. D., & Kyriakides, S. (1994). In-plane compressive response and crushing of honeycomb. *Journal of the Mechanics and Physics of Solids*, *42*(10), 1499-1532.

Papka, S. D., & Kyriakides, S. (1998). In-plane crushing of a polycarbonate honeycomb. *International Journal of Solids and Structures*, *35*(3-4), 239 - 267.

Peters, W. H., & Ranson, W. F. (1982). Digital imaging techniques in experimental mechanics. *Optical Engineering*, *21*, 427-431.

Petras, A., & Sutcliffe, M. P. F. (1999). Failure mode maps for honeycomb sandwich panels. *Composite Structures*, *44*(4), 237-252.

Rogers, W. F. (1972). *Apollo lunar module landing gear* (Tech. Rep.). http://ntrs.nasa.gov: NASA Technical Report.

Rohrbach, Z. J., Buresh, T. R., & Madsen, M. J. (2012). Modeling the exit velocity of a compressed air cannon. *American Journal of Physics*, *80*(1), 24-26.

Rots, J. G., Nauta, P., Kusters, G. M. A., & Blaauwendraad, J. (1985). Smeared crack approach and fracture localization in concrete. *Heron*, *30*(1).

Sain, T., Meaud, J., Yeom, B., Waas, A. M., & Arruda, E. M. (2013). Rate dependent finite strain constitutive modeling of polyurethane and polymer-clay nanocomposites. *Journal of the Mechanics and Physics of Solids*. (In review)

Schwingshackl, C. W., Aglietti, G. S., & Cunningham, P. R. (2006). Determination of honeycomb material properties: Existing theories and alternative dynamic approach. *ASCE Journal of Aerospace Engineering*, *19*(3), 177-183.

Seide, P., Weingarten, V. I., & Morgan, E. J. (1960, December). *The development of design criteria for elastic stability of thin shell structures.* (Tech. Rep. No. Final Report: STL/TR-60-0000-19425). Los Angeles, CA: Space Technology Laboratories, Inc.

Simulia. (2011). *ABAQUS user manual*. Edition 6.11.

Singer, J., Arbocz, J., & Weller, T. (2002). *Buckling experiments: Experimental methods in buckling of thin-walled structures, vol. 2 - shells, built-up structures, composites and additional topics*. Wiley.

Sutton, M. A., Wolters, W. J., Peters, W. H., Ranson, W. F., & McNeill, S. R. (1983). Determination of displacements using an improved digital image correlation method. *Image and Vision Computing*, *1*, 133-139.

Vinson, J. R. (2001). Sandwich structures. *Applied Mechanics Reviews*, *54*(3), 201-214.

von Kármán, T., & Tsien, H.-S. (1941). The buckling of thin cylindrical shells under axial compression. *Journal of the Aeronautical Sciences*, *8*, 303 - 312.

Vural, M., & Ravichandran, G. (2003). Dynamic response and energy dissipation characteristics of balsa wood: experiment and analysis. *International Journal of Solids and Structures*, *40*, 2147-2170.

Weingarten, V. I., Seide, P., & Peterson, J. P. (1965). *Buckling of thin-walled circular cylinders* (Tech. Rep.). NASA SP 8007.

Wierzbicki, T., & Abramowicz, W. (1983). On the crushing mechanics of thin-walled structures. *ASME Journal of Applied Mechanics*, *50*, 727-734.

Wilbert, A., Jiang, W.-Y., Kyriakides, S., & Floccari, J. F. (2011). Buckling and progressive crushing of laterally loaded honeycomb. *International Journal of Solids and Structures*, *48*, 803-816.

Wu, E., & Jiang, W.-S. (1997). Axial crush of metallic honeycombs. *International Journal of Impact Engineering*, *19*(5-6), 439-456.

Xie, D., & Biggers, S. B. (2006). Strain energy release rate calculation for a moving delamination front of arbitrary shape based on the virtual crack close technique. part i: Formulation and validation. *Engineering Fracture Mechanics*, *73*(6), 771-785.

Xie, D., & Waas, A. M. (2006). Discrete cohesive zone model for mixed-mode fracture using finite element analysis. *Engineering Fracture Mechanics*, *73*(13), 1783-1796.

Xue, Z., & Hutchinson, J. W. (2006). Crush dynamics of square honeycomb sandwich cores. *International Journal for Numerical Methods in Engineering*, *65*, 2221-2245.

Zhang, K., Duan, H., Karihaloo, B. L., & Wang, J. (2010). Hierarchical, multilayered cell walls reinforced by recycled silk cocoons enhance the structural integrity of honeybee combs. *Proceedings of the National Academy of Sciences*, *107*(21), 9502-9506.

Zhou, G., Hill, M., Loughlan, J., & Hookham, N. (2006). Damage characteristics of composite honeycomb sandwich panels in bending under quasi-static loading. *Journal of Sandwich Structures and Materials*, *8*(1), 55-90.